

ABSTRACT

Title of Dissertation: Analogue Cosmology Experiments
with Sodium Bose-Einstein Condensates

Swarnav Banik
Doctor of Philosophy, 2021

Dissertation Directed by: Dr. Gretchen Campbell
Department of Physics

Due to their high degree of controllability and precise measurement capabilities, ultracold ensembles of neutral atoms are a leading platform for performing quantum simulations. In this thesis, I will describe the design and construction of an analog quantum simulator based on ^{23}Na Bose-Einstein Condensates (BEC). Our system can produce and trap BECs in arbitrary-shaped quasi two-dimensional optical dipole traps, which can be dynamically altered during an experimental sequence. Such controlled variation of the BEC's spatial mode enables exploration of open questions in superfluidity, atomtronics, and analogue cosmology. I will describe the implementation of our system to study the inflationary dynamics of the early universe and report our recent results on the simulation of cosmological Hubble friction. We expand and contract a toroidally shaped BEC and analyze the time evolution of its collective phonon modes. These excitations are analogous to fluctuating scalar fields in an expanding universe. The changing metric of the expanding or contracting background BEC results in dilation of the phonon field through a term dependent on the expansion speed, similar to Hubble friction in inflationary models

of the universe. We conclusively demonstrate the analogy by experimentally measuring Hubble attenuation and amplification. Our measured strength of Hubble friction disagrees with recent theoretical work [J. M. Gomez Llorente and J. Plata, *Phys. Rev. A* **100** 043613 (2019) and S. Eckel and T. Jacobson, *SciPost Phys.* **10** 64 (2021)], suggesting inadequacies in the current model.

ANALOGUE COSMOLOGY EXPERIMENTS
WITH SODIUM BOSE EINSTEIN CONDENSATES

by

Swarnav Banik

Dissertation submitted to the Faculty of the Graduate School of the
University of Maryland, College Park in partial fulfillment
of the requirements for the degree of
Doctor of Philosophy
2021

Advisory Committee:

Professor Steven Rolston, Chair

Dr. Gretchen Campbell, Co-chair/Advisor

Dr. Ian Spielman

Professor Rajarshi Roy

Professor Mohammad Hafezi, Dean's Representative

© Copyright by
Swarnav Banik
2021

Acknowledgments

My experience in the 'Laser Cooling and Trapping' group at the Joint Quantum Institute (JQI) has been enriching. The training and exposure received during the past few years has not only had a transformational impact on my problem-solving approach but also helped me appreciate the importance of collaborations in doing so. During my Ph.D. I had the privilege to work with and learn from incredibly talented researchers. The collaborative environment fostered by Bill Philips, Gretchen, Ian, Trey Porto, Steve Rolston, Alicia Koller, and former graduate students Daniel Barker, Benjamin Rechovsky, Neal Pimenti, Zach Smith, Varun Vaidya, Dan Campbell, Ana Valdes Curiel, Francisco Salces Carcoba (Paco), Dalia Ornelas-Huerta, and Avinash Kumar made it a delight to work in this group. As a new graduate student, I had a minimal experimental background and was in absolute awe of the massive homemade multi-component quantum simulators at JQI. A major part of my doctoral work involved the construction of one such setup. This would not have been possible without the help and support that I received from my colleagues. Here is my humble attempt to acknowledge and thank them for making this experience as fulfilling as it was.

First of all, I would like to thank my advisors, Gretchen Campbell and Ian Spielman, for being such great mentors. Throughout my Ph.D., their patience and encouragement were instrumental in helping me develop my intellectual faculties and grow as an independent

researcher. Gretchen's ability to see through complex problems and bring our attention to what matters most has helped us establish priorities for the project. Ian's ability to adapt relevant experimental techniques from different fields of research is impressive. It was a privilege to learn from such great researchers. The construction of this lab would not have been possible without the efforts of my fellow labmates Monica Gutierrez Galan, Hector Sosa Martinez, and Madison Anderson. Hector's presentation skills and Monica's workflow design and systematic approach to problem-solving are some of the many invaluable skills I'll take with me from grad school. When I was a young graduate student, our former labmate Avinash Kumar patiently taught the basics of an AMO experiment, such as optical alignment. I am very thankful for his eagerness to help.

I would also like to thank our electronics guru Alessandro Restelli for his help on many electronic projects which now power our apparatus. Over the years, my interactions with members of the Strontium lab, Neal Pisenti, Peter Elgee, and Ananya Sitaram, have resulted in many productive collaborations. Insightful discussions with fellow JQI grad student Sarthak Subhankar has helped me identify gaps in my understanding. Discussions with our new post-doc Shouvik Mukherjee and my roommate Tamoghna Barik have allowed me gain a perspective different from AMO physicists.

My friends Kumi Wickramanayaka, Umesh Kumar, Subhojit Dutta, Yidan Wang, Nicholas Mennona, Sabyasachi Barik, and Nitish Mehta have been a constant source of support. I am thankful to Kumi for cheering me up when things didn't work in the lab. My undergraduate classmate Umesh has always kept in touch, and I am genuinely grateful for having him as a friend. Lastly, my family has been a great source of support throughout these years. My parents have always gone out of their way to help me realize my dreams.

I'm grateful for having such a caring family.

Table of Contents

Acknowledgements	ii
Table of Contents	v
List of Tables	vii
List of Figures	viii
List of Abbreviations	xv
Chapter 1: Introduction	1
1.1 Outline of the Thesis	4
Chapter 2: Theory of Bose Gas	5
2.1 Ideal Non-interacting Bose Gas	5
2.2 Mean Field Dynamics of Weakly Interacting BECs	6
2.2.1 Thomas Fermi Approximation	9
2.2.2 Collective Excitations: Phonons	10
2.2.3 Damping of Low-energy Excitations	12
Chapter 3: Analogue Gravity	14
3.1 Previous Experiments	16
3.2 BEC Phonon Wave Equation and the Space-time Metric	17
3.3 Wave Equation in a Toroidal BEC	20
Chapter 4: Experimental Apparatus	23
4.1 Vacuum Chamber	24
4.2 Laser Frequency Stabilization	26
4.3 Optical Dipole Traps	31
4.3.1 Red-detuned Optical Dipole Trap	31
4.3.2 Blue-detuned Optical Dipole Trap	33
4.4 Imaging	38
4.4.1 Partial Transfer Absorption Imaging	39
4.4.2 Probe Reconstruction	42
Chapter 5: Production of BEC	46
5.1 2D MOT Source	47

5.2	Laser Cooling	50
5.3	Forced Evaporation	54
5.4	Transfer to Purely Optical Traps	59
Chapter 6: The Hubble Friction Experiment		62
6.1	Publication: Hubble Attenuation and Amplification in Expanding and Contracting Cold-Atom Universes	64
6.1.1	Abstract	64
6.1.2	Introduction	64
6.1.3	Experiment and Results	69
6.2	Model for the Toroidal Potential and Scaling Laws	75
6.3	Simulation: Impact of Phonon Phase on Hubble Friction Strength	77
6.3.1	Simulation Model	79
6.3.2	Simulation Results	80
6.4	Mode Purity of the Phonons	82
6.5	Fitting Method	85
Chapter 7: Towards Erbium BEC: Scanning Transfer Cavity Lock		89
7.1	Laser Cooling of Erbium	91
7.2	Frequency Stabilization of 583 nm Laser	94
7.3	Fabry Perot Etalons	97
7.4	Construction of the Setup	102
7.4.1	Cavity Construction	102
7.4.2	Electronics	109
7.5	Results and Outlook	111
Chapter 8: Conclusions and Outlook		115
Appendix A: Characterizing Imaging Aberrations		117
Bibliography		124

List of Tables

4.1	Detunings and intensities of the different laser cooling beams. For the first five entries, detunings are from the cooling transition. For the last three entries, detunings are from the repump transition. For reference, the saturation intensity for the cooling transition is $I_{\text{sat}} = 6.26 \text{ mW/cm}^2$. . .	31
6.1	Best fit global parameters.	72
6.2	Fit results of the eight different techniques when applied to the expansion data sets.	86
6.3	Fit results of the eight different techniques when applied to the contraction data sets.	86
7.1	Erbium laser cooling transitions [1].	94
7.2	Thermal expansion of cavity parts.	104

List of Figures

3.1	A moving fluid creating an acoustic horizon when supersonic flow avoids upstream movement of sound waves. The colored circles represent time-evolution of acoustic wavefronts in the fluid space-time. $\mathbf{e}_x - \mathbf{e}_y$ plane represents spatial coordinates. Time is expressed in different colors according to the color bar to the left. The vertical red lines denotes the sonic horizon. (a) and (b) depict how the wavefront time-evolution changes with varying fluid velocity v and sound speed c_s , respectively.	15
4.1	Schematic of the vacuum chamber. The source chamber, science chambers, and the sodium oven are indicated. The blue circle points to the location of the differential pumping tube, with the inset showing a schematic of the tube. The yellow line indicates the push laser beam used for transferring atoms from the source to the science chamber.	24
4.2	Cross-section of the differential pumping tube.	26
4.3	Energy levels for the ^{23}Na D_2 transition [2]. The yellow and green lines indicate the cooling and repump transitions separated in frequency by 1.7 GHz.	27
4.4	Schematic of the optical setup inside the Toptica DL-pro laser [3]. The inset shows a magnified view of the ECDL, indicating the piezo actuated grating, which can be externally controlled via the voltage V_{piezo}	28
4.5	Optical schematic of the SAS setup. The yellow lines indicate light from a Toptica DL-pro laser which is first upshifted by 150 MHz and then split into pump and probes. The signal from a balanced photodetector, as shown in the rectangular box, is sent to a lock-in amplifier.	29
4.6	(a) Lock-in scheme to obtain the derivative of the SAS absorption signal V_{PD} . The blue and purple lines represent V_{PD} and the derivative signal V_{lockin} respectively. The dashed box indicates the components of a lock-in amplifier. The local oscillator is a Voltage Controlled Oscillator (VCO) that drives the AOM. The servo generates the signal V_{piezo} to control the laser frequency. (b) V_{PD} and V_{lockin} indicated in blue and purple, respectively.	29

4.7	Propagation of ODT beams in the science chamber. The main figure shows the red-detuned ODT propagating along positive \mathbf{e}_x and being focused down at the center of the chamber. The blue-detuned sheet ODT propagates along positive \mathbf{e}_y . The inset shows beam propagation on the $\mathbf{e}_y - \mathbf{e}_z$ plane. The blue-detuned DMD ODT propagates along negative \mathbf{e}_z . Gravity acts along negative \mathbf{e}_z	32
4.8	Schematic for the sheet trap optical setup. Blue-detuned laser light from a single-mode fiber is collimated and propagated through lenses L_1, L_2, L_3 and a π phase plate along the \mathbf{e}_y direction. (a) and (b) shows the beam profile in the $\mathbf{e}_z - \mathbf{e}_y$ and $\mathbf{e}_x - \mathbf{e}_y$ planes, respectively. Figures (c) and (d) show the simulated $\mathbf{e}_z - \mathbf{e}_x$ beam intensity profiles at indicated Y positions, with \mathbf{e}_z along the vertical axis and \mathbf{e}_x along the horizontal. The color bar encodes the relative beam intensity for figures (c) and (d). The atoms, as depicted by the yellow dots, lie close to the front focal plane of lens L_3 . Gravity acts along negative \mathbf{e}_z	34
4.9	Simulations exploring slight vertical misalignment between laser spot and π phase plate. The top panel is a schematic depicting the relative vertical distance between the laser spot and the π phase plate. The elongated beam has a $1/e^2$ beam waist of 5 mm on a phase plate of clear aperture radius 25 mm. The middle panel shows the $\mathbf{e}_z - \mathbf{e}_x$ intensity profile of the beam at the front focal plane of L_3 . The color bar encodes the relative beam intensity for the middle panel. The bottom panel is a vertical cut-out showing the intensity profile along the \mathbf{e}_z axis from the middle panel. (a), (b), and (c) correspond to 0, 3, and 5 mm misalignments, respectively.	35
4.10	(a) Schematic of the DMD optical setup. P_o and P_i refer to the DMD and atom planes, respectively. The purple lines are rays representing imaging of the DMD pattern onto the plane P_i . The blue lines indicate the spatial profile of the collimated laser beam as it travels through the optics. (b) DMD being used as a binary amplitude grating. The top panel shows binary patterns imprinted onto the DMD plane P_o . The dark and bright regions represent micromirrors in the OFF and ON positions, respectively. The bottom panel shows the resultant atomic density distribution on the atom plane P_i . (c) DMD being used as an analog amplitude grating using halftoning. The right panel shows the overlap between the images of adjacent DMD pixels when projected through the imaging system. The right panel shows halftoning implemented in our system.	37
4.11	Partial Transfer Absorption Imaging. (a) The atomic levels involved in imaging the atomic sample. The inset shows a magnified view of the transitions induced by microwaves. The splitting in the hyperfine levels of the ground state is caused by a constant magnetic field applied throughout the experiment. (b) Rabi oscillations for the transition $ F = 1, m_F = -1\rangle$ to $ F = 2, m_F = -2\rangle$. (c) Smith chart for the impedance matched microwave antenna.	40
4.12	(a) Schematic of absorption imaging optical setup. The dark field created by the atoms cast a shadow on the probe.	43

4.13	Optical densities obtained via absorption imaging without (a) and with (b) PCA. The gray bar indicates optical densities for both (a) and (b).	43
4.14	Principal Component Analysis. (a) The variance along each of the principal components. (b) σ_{A-P} as a function of the number of principal components used for reconstructing the reference image \mathcal{P}	44
5.1	Flux vs. sodium atomic velocity at different temperatures. The blue, orange and green curves correspond to 150°C, 200°C, and 230°C, respectively. As a point of reference, 3D MOT velocities are usually less than 100 m/s.	47
5.2	(a) Schematic of the old NIST experiment [4]. The main chamber is separated from the sodium source by a long Zeeman slower tube wound by magnetic field coils creating a space-varying magnetic field. (b) and (c) are two orthographic views of the 2D MOT chamber. The cooling arms cool atoms in the $\mathbf{e}_x - \mathbf{e}_y$ plane, as shown in (b). The push beam pushes atoms into the main chamber along the \mathbf{e}_z direction, as shown in (c). Sodium atoms effuse out of the oven in the positive \mathbf{e}_y direction. The slower beam is propagated along negative \mathbf{e}_y . The black bars at the top right and bottom center are scale bars for (a) and (b)/(c), respectively. . . .	48
5.3	Cross-sectional views of the science chamber with the 3D MOT cooling beams depicted in yellow and quadrupole coils in purple.	50
5.4	3D MOT $1/e^2$ diameter D vs. time of flight t_{flight} . The red curve is a fit to the blue data points according to Eq. (5.1). The temperature of the thermal atomic cloud is estimated to be $T = 294(25) \mu\text{K}$ by measuring the rate of expansion, as described in the text.	52
5.5	Critical laser cooling parameters vs. time t . Magnetic field gradient B' , cooling laser beam detuning δ_{cool} and power P_{cool} during 3D MOT and PGC stages. The vertical dashed red lines separate the laser cooling steps into three sections. The first 10 s long section is the 3D MOT loading. PGC is performed for the remaining 2.25 ms and 1.5 ms sections.	53
5.6	Schematic of the transfer of atoms from a quadrupole magnetic trap to a hybrid magnetic and optical trap. (a), (b), and (c) depict three snapshots during the transfer process as the magnetic field gradient is reduced from 228 G/cm (a) to 120 G/cm (b) and finally dropped to 7.3 G/cm (c). Gravity acts along the negative \mathbf{e}_z direction. The gravity compensation field gradient is 8 G/cm. The top row is a schematic of the single IR beam dipole trap. The origin marks the center of the magnetic trap. Atoms are adiabatically transferred into the hybrid trap as the field gradient is lowered. The bottom panel shows the change in potential energy landscape U along \mathbf{e}_z at $(x, y) = (0, 0)$, as the field gradient is reduced.	54
5.7	Critical forced evaporation parameters vs. time t . Magnetic field gradient B' (a), RF frequency ω_{RF} (b), and IR ODT power P_{ir} (c) during RF evaporation, adiabatic transfer and hybrid trap evaporation stages. The vertical dashed red lines indicate the separation of the three stages.	57

- 5.8 Transfer of BEC into purely optical traps. Critical parameters, magnetic field gradient B' (a), IR ODT power P_{ir} (b), sheet trap ODT power P_{gs} (c), and DMD ODT power P_{dmd} (d) vs. time t . The vertical dashed lines indicate the instant when the in-situ ODs (e)-(l) were imaged. (e)-(h) are ODs on a vertical plane, with the horizontal axis pointing along the IR beam (\mathbf{e}_x) and gravity acting along the vertical axis (\mathbf{e}_z). (i)-(l) are ODs on a horizontal plane, with the horizontal axis pointing along the sheet trap beam (\mathbf{e}_y) and the vertical axis pointing along the IR beam (\mathbf{e}_x). The black bars in (e) and (i) correspond to $50 \mu\text{m}$, the length scales being same for all horizontal and vertical images separately. The color bar at the bottom depicts the OD scale for (e)-(l). 61
- 6.1 Ring-trapping potential and resulting atomic density. The green surface schematically depicts the trapping potential; the orange lines mark the typical chemical potential μ . The blue-dashed curve shows a power law fit to the potential (up to μ) around $\rho = 0$ giving exponent 2.02(3) for this example. The measured 2D density $n_{2\text{D}}(\rho, \theta)$ is shown in the \mathbf{e}_x - \mathbf{e}_y plane (with peak density $165 \mu\text{m}^{-2}$) and the white dashed arc marks the mean radius R . Because of the short $500 \mu\text{s}$ TOF, the observed width of the ring is slightly in excess of that anticipated from the in-situ T-F approximation. 66
- 6.2 Phonon evolution in a contracting toroidally-shaped BEC, averaged over three measurements. (a) Density perturbations for a ring with $R_i = 38.4(6) \mu\text{m}$ at 10 ms and 35 ms, and $R_f = 11.9(2) \mu\text{m}$ at 45 ms and 53 ms. The density scale of images before contraction is multiplied by 2. The horizontal bar corresponds to $80 \mu\text{m}$. (b) Experimental measurements and (c) fit to Eq. (6.1) of angular density perturbation $\delta n_{1\text{D}}$ as a function of azimuthal angle θ and time t , where the ring contraction occurs at t_i . (d) Phonon amplitude δn as a function of time. The circles plot the phonon amplitude obtained from fitting each time-slice of (b) to a sinusoid. The red curve is the instantaneous amplitude from the fit in (c). The diamonds are the measured mean radius of the BEC and the blue line is the programmed radius of the trap. The grayscale bar encodes the value of $|\dot{R}/R|$, with a maximum of $328(11) \text{ s}^{-1}$ at $t_{\text{peak}} = 41 \text{ ms}$. The arrow indicates $t_i = 38.2 \text{ ms}$ 68
- 6.3 Phonon amplitude δn as a function of time t for (a) expanding and (b) contracting tori. The symbols, curves, and grayscale bars are all as notated in Fig. 6.2(d). The expansion data (a) used $R_i = 11.9(2) \mu\text{m}$ and $R_f = 38.4(6) \mu\text{m}$, and vice versa for contraction (b). t_i is varied from 6.5 ms to 23 ms for expansion and from 27 ms to 70 ms for contraction. Here, the red curves show simultaneous fits to our complete data set, as discussed in the text. 69

6.4	Phonon amplitude vs. phase. (a) Data (black circles), fit (red curve), and oscillation envelope (blue curve) used to extract the amplitude A_f at t_{peak} . The grayscale bar is as notated in Fig. 6.2(d). (b) Ratio of amplitudes A_f/A_i vs. φ_{peak} , the oscillation's phase at t_{peak} . The black circles plot the data. The gray dashed, blue solid, and gray dashed-dot curves show the prediction of Eq. (6.1) for $\gamma_H = 0, 0.36,$ and $1,$ respectively, with $\alpha = 0.52$. The red line indicates the prediction for an adiabatic contraction.	73
6.5	Simulations to study the impact of phonon phase φ_{peak} on Hubble friction strength. (a) Phonon amplitude (solid black curve), and oscillation envelope (dashed red curve) used to extract the amplitude A_i and A_f at t_{peak} . The blue curve denoted the radius R as a function of time t . The grayscale bar is as notated in Fig. 6.2 (d). t_{peak} is the time when $ \dot{R}/R $ attains maximum value. (b) Ratio of amplitudes A_f/A_i vs. φ_{peak} , the oscillation's phase at t_{peak} . The solid red and dashed black curves correspond to a value of γ_H of 0.5 and $0,$ respectively.	81
6.6	Relative contributions of different azimuthal modes in the imprinted phonon. (a) Raw data n_{1D} for phonons in a torus of radius $R = 31.8 \mu\text{m}$. (b) The black dots, red open circles and blue crosses show the time evolution of $\Im[\mathcal{A}_m]$ for modes with $m = 1, 2,$ and $3,$ respectively. The colored solid lines represent decaying sinusoidal fits according to Eq. (6.18). Each colored fit curve corresponds to the data points of the same color. (c) The amplitude B_m (see Eq. (6.18)) for the three modes evaluated from the fits in (b).	83
6.7	Phonon amplitude δn as a function of time t for stationary tori of radii $11.9, 14.3, 16.7, 24.0, 31.2, 38.4$ and $43.2 \mu\text{m}$ from top to bottom. Here, the red curves show simultaneous fits to the complete data set, as discussed in Sec. 6.1.3.	88
7.1	The Erbium ground state.	91
7.2	Laser cooling transitions in atomic Erbium [1]. The purple and green arrows indicate the cooling transitions used for the 2D MOT and 3D MOT, respectively.	93
7.3	Vapor pressure of Sodium and Erbium as function of temperature [5].	95
7.4	Interference in a simple Fabry Perot cavity. The beam on entering the cavity undergoes multiple reflections. These when constructively interfere lead to a maximum in transmission intensity.	97
7.5	Cavity transmission peaks with varying mirror reflectivity R , according to Eq. (7.4). The red, green and purple curves correspond to a reflectivity R of $0.6, 0.8$ and $0.995,$ respectively.	98
7.6	Schematic of a Fabry Perot with curved mirrors. The mirrors with radii of curvature R_1 and R_2 are separated by a distance d	99

7.7	Stability diagram for a two mirror cavity based on Eq. (7.5). The red points (1), (2), and (3) indicate positions of plane parallel ($R_1 = R_2 = \infty$), symmetric confocal ($R_1 = R_2 = L/2$), and concentric ($R_1 = R_2 = L$) mirror configurations. The blue point (4) indicates the position of the STC.	101
7.8	Schematic of the scanning Fabry Perot cavity. The curved mirror is attached to the piezo which is epoxied to the invar spacer via a macor ring. The plane mirror is attached on the other end of the spacer.	103
7.9	Linewidth measurement of the constructed STC. The blue points correspond to measured transmitted intensity I_t as the cavity piezo is scanned. The horizontal axis is the cavity resonance frequency ν_{cav} relative to the master laser frequency ν_{master} which serves as a reference. The black line is a Lorentzian fit to the data giving a linewidth of 1.14 MHz.	105
7.10	Optical setup of the scanning transfer cavity. Light from the two lasers are couple into a fiber and sent to the STC. Lenses with focal length $f_1 = 150mm$ and $f_2 = 100mm$ are used to mode match to the cavity.	106
7.11	Mode matching optics for the cavity. The Gaussian beam from the fiber is collimated using an asphere. Lenses f_1 and f_2 are placed appropriately to achieve mode matching. d_i 's are the distances between the various components. d_0, d_1, d_2 and d_3 are 127, 150, 120 and 317.5 mm respectively.	107
7.12	Pulse Detection action by the analog board. A voltage pulse (a) detected in the photo diode is sent through a number of electronic components which ultimately drive the NAND gate signal (f) LOW. This digital pulse is fed to the micro controller.	110
7.13	Non-uniform motion of the piezo leads to multiple kinks on the cavity transmission peak. The yellow curve is the transmission peak and purple is the digital signal sent to the microprocessor, signaling a transmission peak's occurrence. Each vertical division is 500 mV for yellow and 2V for purple. Each division on the horizontal axis is 250 μ s.	111
7.14	Master and slave frequency drifts $\delta\nu$ as the master oscillates and drifts. The master SatAbs lock was dis-engaged and the master laser frequency was modulated by 5MHz in a period of 0.5 s. The top panel is data acquired over long periods and shows the overall drift in the mean frequency. The bottom panel is a zoomed-in version of the top panel. Measurements were made using the 'Angstorm WSU2' wavemeter via a fiber switch. . .	112
7.15	Histogram of the slave frequencies as it is locked (red) and unlocked (blue). Measurements were made using the 'Angstorm WSU2' wavemeter via a fiber switch.	113
7.16	Cavity transmission peaks (yellow curve) and corresponding pulses generated by analog board (purple) as the cavity (a) or laser (b) is scanned in frequency. Each vertical division is 500 mV for yellow and 2V for purple. Each division on the horizontal axis is 250 s. The above data was taken by scanning the cavity and laser at 3.4 GHz/s.	114

A.1	Comparison of length and spatial frequency scales for imaging BECs. (a) and (b) correspond to imaging systems with spatial resolutions l_{min} and R . The grid represents camera pixels. Thermal De-Broglie wavelength λ_{dB} and healing length ξ are indicated. The dashed circles in (b) correspond to (a)'s solid circles of the same color. (c) Length scales in (a) and (b) in the Fourier domain.	118
A.2	(a) Atomic density of weakly interacting disk-shaped BEC $n_{exp}(\mathbf{r}_l)$. (b) Density variation of (a) $\delta n_{exp}(\mathbf{r}_l)$ about the average 50 shots. The densities in both (a) and (b) are in the same arbitrary units.	119
A.3	(a) Experimentally evaluated density fluctuation power spectrum as a function of the spatial frequency \mathbf{k}_l . (b) Result of fitting (a) to Eq. A.4. The dashed circles enclose resolvable spatial frequencies for an imaging system with NA = 0.28. The color bar holds for both (a) and (b).	121
A.4	(a) Wavefront aberration determined by fitting Fig. A.4 (a) to Eq. A.4. (b) Wavefront aberration reconstructed by projecting (a) onto a Zernike polynomial basis.	122
A.5	Experiment to deterministically change the system defocus. (a) The imaging system with image distance z_i as indicated. (b) Variation of Zernike defocus coefficient Z_0^2 as a function of Δz_i	123

List of Abbreviations

AOM	Acousto-Optical Modulator
BEC	Bose-Einstein Condensate
CAD	Computer Aided Design
CTE	Coefficient of Thermal Expansion
DC	Direct Current
DMD	Digital Micromirror Device
FP	Fabry Perot
FSR	Free Spectral Range
GP	Gross-Pitaevskii
IR	Infra-Red
MOSFET	metal-Oxide-Semiconductor Field-Effect Transistor
MOT	Magneto-Optical Trap
NIST	National Institute of Standards and Technology
ODT	Optical Dipole Trap
PGC	Polarization Gradient Cooling
PI	Proportional Integral
PSF	Point Spread Function
PTAI	Partial Transfer Absorption Imaging
RF	Radio Frequency
SPOT	Spontaneous Force Optical Trap
STC	Scanning Transfer Cavity
TEM	Transverse Electro-Magnetic
T-F	Thomas Fermi
UHV	Ultra High Vacuum
ZS	Zeeman Slower

Chapter 1: Introduction

Since their first realization in 1995 [6, 7], Bose-Einstein Condensates (BEC) have emerged as an ideal platform for performing quantum simulations. Early efforts in simulating the Bose-Hubbard model in 3D optical lattices [8, 9] and tuning atomic interactions via Feshbach resonances [10–13] have illustrated the ability of such systems to simulate defect-free and fully configurable synthetic materials. Moreover, the coherent manipulation of BEC matter waves has opened up the fields of atomtronics [14–19], atomic wave interferometry [20], and laboratory simulations of cosmological phenomena [21–25], to name a few.

Bose-Einstein condensation occurs due to the macroscopic occupation of the single-particle ground state. The phenomenon was first predicted in 1925 by Albert Einstein [26] using methods of quantum statistics developed by S.N. Bose [27]. At a temperature T , atoms of mass m can be regarded as wavepackets with a spatial extent corresponding to the thermal de Broglie wavelength $\lambda_{\text{dB}} = \sqrt{2\pi\hbar^2/mk_B T}$. As these atoms are cooled, λ_{dB} increases, and at extremely low temperatures, it exceeds the inter-atomic spacing. These individual wavepackets at ultracold temperatures coherently superimpose to form a single collective matter wave. If the atoms are bosonic, all of them occupy the lowest quantum state to form a BEC, thereby serving as a macroscopic lens into quantum phenomena.

Attaining quantum degeneracy requires cooling atoms to sub 100 nK temperatures, making the production of BEC technically challenging. With the availability of tunable wavelength lasers, significant progress in laser cooling [28–30] in the 1980’s and forced evaporation techniques [31, 32] in the early 1990’s resulted in the laboratory realization of BECs, 70 years after the first prediction.

Depending on the system, quantum effects become apparent at different temperatures. For example, metal electrons exhibit strong quantum phenomena below the Fermi temperature ($10^4 - 10^5$ K), liquid helium around 1K, and atomic nuclei around 10^{11} K [33]. These temperatures are significantly higher than those required for Bose condensing neutral atoms. However, despite their technically challenging production, quantum-degenerate gases are superior for performing quantum simulations due to the unprecedented control and measurement capabilities they offer. Almost all atoms in a BEC occupy the same quantum state, allowing the interactions between the component atoms to be described by an effective mean-field interaction potential [33,34]. This approach reduces the many-body problem into a single-body problem which is much easier to model. Furthermore, the inter-atomic interactions can be tuned by orders of magnitude using Feshbach resonances [35]. In addition to the interaction potential, BEC systems offer tunability in terms of the condensate fraction, temperature, and shape of the atomic cloud. Because of the dilute nature of these atomic samples, they can be probed via optical means, thereby facilitating an ease of measurement.

The process of Bose condensation is a purely statistical one and has nothing to do with inter-atomic interactions. When gases are cooled, they liquify and eventually solidify, at which stage the interactions become dominant. Avoiding this solidification is

a major challenge in producing quantum degenerate gases. Usually, atoms have a very high molecular binding energy which energetically favors solidification [36]. However, since it occurs at a rate proportional to the gas density, molecular binding is avoided by reducing the atomic density.

In this thesis, I will describe the construction of our ^{23}Na BEC apparatus, aimed at performing quantum simulations. Historically, our group has used BECs to study superfluidity [17,37–40], atomtronics circuits [18,19] and perform cosmological simulations [41]. In 2007, the old Sodium Rings lab at the National Institute of Standards and Technology (NIST) observed superflow in the form of persistent currents in a toroidally shaped BEC [37]. Since then, many of our experiments have focused on exploring the persistent current’s decay mechanism [17,39,40] and using them for atomtronic circuits [18,19]. Towards the old apparatus’s end of life, the group performed some experiments to simulate cosmological analogues in BECs [41]. In 2015, we started building a new apparatus to make a dual-species BEC with Sodium and Erbium. The old apparatus had many limitations, which were addressed in this new system. Additionally, we decided to add highly magnetic Erbium with a magnetic moment $7\mu_B$, to exploit its long-range interactions for studying strongly correlated many-body systems. In 2018, we Bose condensed ^{23}Na , and after that developed capabilities to confine the BEC in arbitrary-shaped two-dimensional Optical Dipole Traps (ODT). Significant advances have been made on the Erbium front as well. In this thesis, I will describe our apparatus, our approach to simulate analogue cosmology using BECs, and a specific example where we simulate the cosmological phenomena of Hubble friction. Since many references describe laser cooling, forced evaporation, and production of BECs [42,43], I will only briefly touch upon these topics. In the next two

chapters I will describe collective modes in a BEC, introduce the idea of analogue gravity and explain how a BEC's collective modes can be used to develop experimental systems for analogue gravity.

1.1 Outline of the Thesis

In 2015, after decommissioning the NIST Sodium Rings apparatus, we embarked on the journey of constructing the new Sodium-Erbium BEC laboratory. The rest of the thesis describes the construction and working of this new apparatus and explains an analogue cosmology experiment performed on it. It is structured as follows. In Chapter 2 I start with describing the theory of Bose-Einstein condensation and follow it with a discussion on the origin and nature of collective excitations in BECs. Chapter 3 introduces the idea of Analogue Gravity and explains how collective excitations in BECs could be used for simulating cosmology. Chapter 4 describes the experimental apparatus, and Chapter 5 explains the procedure employed for producing BEC and further transferring them into arbitrary 2D Optical Dipole Traps (ODT). Chapter 6 reports the simulation of Hubble attenuation and amplification in a toroidal BEC. Though these experiments were performed with ^{23}Na BEC, we have made significant progress towards trapping Erbium in a Magneto-Optical trap (MOT). Chapter 7 describes a Scanning Transfer Cavity scheme used for locking Erbium lasers in our laboratory. Finally, I end with with an outlook in Chapter 8.

Chapter 2: Theory of Bose Gas

2.1 Ideal Non-interacting Bose Gas

Bose-Einstein condensation is a quantum-statistical phenomenon that occurs due to the macroscopic occupation of the ground state. This section will discuss the behavior of an ideal non-interacting ensemble of bosons and highlight the role of quantum statistics in Bose condensation as the ensemble's phase space densities approach unity. It follows the discussion in Ref. [44].

Consider an system of N bosons with chemical potential μ and temperature T . The occupancy of a state $n(\epsilon)$ with energy ϵ is described by the Bose-Einstein statistics, given by

$$n(\epsilon) = \frac{1}{\exp((\epsilon - \mu)/k_B T) - 1}, \quad (2.1)$$

where k_B is the Boltzmann constant. The density of states for a 3D homogeneous system $a(\epsilon)$ is given by

$$a(\epsilon) d\epsilon = (2\pi V/h^3)(2m)^{3/2}\epsilon^{1/2}d\epsilon, \quad (2.2)$$

where V is volume, m is the mass of the atoms, and h is Planck's constant. Using Eq. (2.1)

and (2.2), it can be shown that the number of atoms in all the excited states N_e is given by

$$N_e = \frac{V}{\lambda_{\text{dB}}^3} g_{3/2}(z), \quad (2.3)$$

where g_ν is the Bose-Einstein function¹, and $z = e^{\mu/k_B T}$ lies between 0 and 1. Since $g_{3/2}(z)$ increases monotonically with z , the total number of atoms in the excited state satisfies the inequality

$$N_e \leq \frac{V}{\lambda_{\text{dB}}^3} g_{3/2}(1). \quad (2.4)$$

Since Eq. (2.4) sets an upper limit on the maximum number of atoms in the excited state, the remaining atoms are in the ground state. If the phase space density $(N/V)\lambda_{\text{dB}}^3$ exceeds $g_{3/2}(1)$, the only way to satisfy Eq. (2.4) is if all the excess atoms are in the ground state. This results in a macroscopically large number of atoms occupying the ground state, marking the onset of Bose-Einstein condensation. As evident from Eq. (2.4), the necessary condition for Bose condensation is $(N/V)\lambda_{\text{dB}}^3 > g_{3/2}(1) \approx 2.612$. In terms of the density $n = N/V$, and phase space density PSD = $n\lambda_{\text{dB}}^3$, the condition for Bose condensation is expressed as

$$\text{PSD} > 2.612. \quad (2.5)$$

2.2 Mean Field Dynamics of Weakly Interacting BECs

Though the non-interacting picture of ideal Bose gases describes the phenomena of Bose condensation, weak atom-atom interactions in a BEC lead to several interesting

¹ $g_\nu(z) = \frac{1}{\Gamma(\nu)} \int_0^\infty \frac{x^{\nu-1}}{z^{-1}e^x - 1} dx = z + \frac{z^2}{2^\nu + \frac{2^3}{3^\nu} + \dots}$

phenomena. This section derives the time evolution of the BEC wavefunction. Starting from the many-body hamiltonian in the second quantization, a mean-field approach is applied to model the atom-atom interactions. The discussion here follows that in Ref. [33, 34, 45], where detailed derivations can be found.

The second quantization many-body Hamiltonian describing N interacting bosons in an external potential $V(\mathbf{r})$ is given by

$$\begin{aligned} \hat{H} = \int d\mathbf{r} \hat{\Psi}^\dagger(\mathbf{r}) \left[-\frac{\hbar^2}{2m} \nabla^2 + V(\mathbf{r}) \right] \hat{\Psi}(\mathbf{r}) \\ + \frac{1}{2} \int d\mathbf{r} d\mathbf{r}' \hat{\Psi}^\dagger(\mathbf{r}) \hat{\Psi}^\dagger(\mathbf{r}') V_{\text{int}}(\mathbf{r} - \mathbf{r}') \hat{\Psi}(\mathbf{r}) \hat{\Psi}(\mathbf{r}'), \end{aligned} \quad (2.6)$$

where m is the mass of the atom, and V_{int} is the two body interaction potential, and $\hat{\Psi}^\dagger(\mathbf{r})$ and $\hat{\Psi}(\mathbf{r})$ are the the boson field operators corresponding to the creation and annihilation of particles at position \mathbf{r} , respectively. The field operator $\hat{\Psi}(\mathbf{r}, t)$, can be expressed as

$$\hat{\Psi}(\mathbf{r}, t) = \psi(\mathbf{r}, t) + \hat{\Psi}'(\mathbf{r}, t), \quad (2.7)$$

where $\psi(\mathbf{r}, t)$ is a complex function defined as the expectation of $\hat{\Psi}(\mathbf{r}, t)$ such that

$$\psi(\mathbf{r}, t) = \langle \hat{\Psi}(\mathbf{r}, t) \rangle, \quad (2.8)$$

and $\hat{\Psi}'(\mathbf{r}, t)$ represents a small perturbation. The complex function $\psi(\mathbf{r}, t)$ is a classical field representing the BEC wavefunction with $|\psi(\mathbf{r}, t)|^2$ equal to the condensate density. This serves as the order parameter for Bose condensation. Since we wish to derive the time-evolution of condensate wave function $\psi(\mathbf{r}, t)$, we write the Heisenberg equation

of motion for the operator $\hat{\Psi}(\mathbf{r}, t)$

$$\begin{aligned} i\hbar \frac{\partial}{\partial t} \hat{\Psi}(\mathbf{r}, t) &= [\hat{\Psi}, \hat{H}] \\ &= \left[-\frac{\hbar^2}{2m} \nabla^2 + V(\mathbf{r}) + \int d\mathbf{r}' \hat{\Psi}^\dagger(\mathbf{r}', t) V_{\text{int}}(\mathbf{r}' - \mathbf{r}) \hat{\Psi}(\mathbf{r}', t) \right] \hat{\Psi}(\mathbf{r}, t). \end{aligned} \quad (2.9)$$

Due to its diluteness and low temperature, the atom-atom interactions in an alkali BEC can be described by elastic two-body s-wave scattering processes [33, 45]. This allows for the introduction of an effective mean field approach to model these interactions such that the short wavelength degrees of freedom are integrated out. For dilute Bose gases, the effective mean field interaction potential $V_{\text{int}} = g\delta(\mathbf{r} - \mathbf{r}')$ is a contact interaction between two atoms at \mathbf{r} and \mathbf{r}' , where $g = 4\pi\hbar^2 a_s/m$, and a_s is the s-wave scattering length. Applying this mean field interaction potential in Eq. (2.9) and neglecting the perturbing operator $\hat{\Psi}'(\mathbf{r}, t)$ in Eq. (2.7), we get the time-dependent Gross-Pitaevskii (GP) equation

$$\left[-\frac{\hbar^2}{2m} \nabla^2 + V(\mathbf{r}) + g|\psi(\mathbf{r}, t)|^2 \right] \psi(\mathbf{r}, t) = i\hbar \frac{\partial \psi(\mathbf{r}, t)}{\partial t}, \quad (2.10)$$

which describes the time evolution of the BEC wave function $\psi(\mathbf{r}, t)$. It should be noted that since the operator $\hat{\Psi}(\mathbf{r}, t)$ has been approximated to the complex valued scalar field $\psi(\mathbf{r}, t)$, Eq. (2.10) is simply the zeroth order approximation of Eq. (2.9). The first order approximation developed by Bogoliubov, involves retaining terms in the interaction which are at most quadratic in $\hat{\Psi}'(\mathbf{r}, t)$, and treating the resulting interaction as a perturbation on the BEC wavefunction $\psi(\mathbf{r}, t)$. This first order analysis reveals the existence of collective excitations, which have a phonon-like linear dispersion relationship for long wavelengths. Sec. 2.2.3 covers details of the first order analysis useful for understanding concepts in this

thesis. Higher order corrections, which involve retaining terms proportional to $\hat{\Psi}'^3(\mathbf{r}, t)$ and $\hat{\Psi}'^4(\mathbf{r}, t)$, result in damping of the collective excitations. These are finite temperature effects. Sec. 2.2.3 touches upon some of the commonly observed damping mechanisms in BEC experiments.

The stationary solutions of $\psi(\mathbf{r}, t)$ are obtained by considering the form $\psi(\mathbf{r}, t) = \vartheta(\mathbf{r}) \exp(i\mu t/\hbar)$, where ϑ depends only on the spatial coordinate \mathbf{r} . This gives the time-independent GP equation

$$\left[-\frac{\hbar^2}{2m} \nabla^2 + V(\mathbf{r}) + g|\vartheta(\mathbf{r})|^2 \right] \vartheta(\mathbf{r}) = \mu \vartheta(\mathbf{r}) \quad (2.11)$$

The first term in Eq. (2.10) and Eq. (2.11) correspond to the kinetic energy, the second corresponds to the external potential energy V , and the third term is the inter-atomic interaction energy.

2.2.1 Thomas Fermi Approximation

Eq. (2.11) is not exactly solvable and requires the implementation of numerical methods. However, for a BEC with large number of atoms and repulsive inter-atomic interactions ($a_s > 0$), the kinetic energy term $-\frac{\hbar^2}{2m} \nabla^2 \vartheta(\mathbf{r})$ can be neglected with respect to the interaction and potential energy terms. This, known as the Thomas Fermi (T-F) approximation modifies Eq. (2.11) to

$$V(\mathbf{r})\vartheta(\mathbf{r}) + g|\vartheta(\mathbf{r})|^2\vartheta(\mathbf{r}) = \mu \vartheta(\mathbf{r}), \quad (2.12)$$

which is exactly solvable. The solutions for ψ are given under the T-F approximation are given by

$$|\vartheta(\mathbf{r})|^2 = \begin{cases} \frac{\mu - V(\mathbf{r})}{g}, & \text{if } V(\mathbf{r}) < \mu \\ 0, & \text{if } V(\mathbf{r}) > \mu, \end{cases} \quad (2.13)$$

where $|\vartheta(\mathbf{r})|^2 = n(\mathbf{r})$ is the volume density.

2.2.2 Collective Excitations: Phonons

As mentioned in Sec. 2.2, a first-order correction to the hamiltonian in Eq. (2.9) reveals the existence of collective excitations or phonons. In this section, starting from the time-dependent GP equation, I will show how slight variations of $\psi(\mathbf{r}, t)$ leads to collective excitations, which appear as oscillations in the background condensate density and phase.

The wavefunction $\psi(\mathbf{r}, t)$ can be expressed in terms of the atomic density $n(\mathbf{r}, t)$ and phase $\phi(\mathbf{r}, t)$ as $\psi(\mathbf{r}, t) = \sqrt{n(\mathbf{r}, t)}e^{i\phi(\mathbf{r}, t)}$. Substituting this in Eq. (2.10) and comparing the real and imaginary parts gives the continuity equation

$$\frac{\partial n}{\partial t} + \nabla \cdot (n\mathbf{v}) = 0, \quad (2.14)$$

and an equation analogous to Euler equation of fluid dynamics,

$$m \frac{\partial v}{\partial t} + \nabla \cdot \left(\frac{1}{2} m \mathbf{v}^2 + \tilde{\mu} \right) = 0, \quad (2.15)$$

where the velocity of the condensate \mathbf{v} of the condensate is defined as $\mathbf{v} = (\hbar/m)\nabla\phi$, and

$$\tilde{\mu} = V + gn - \frac{\hbar^2}{2m\sqrt{n}}\nabla^2\sqrt{n}. \quad (2.16)$$

The term $\propto \frac{\hbar^2}{2m\sqrt{n}}\nabla^2\sqrt{n}$ in Eq. (2.16) depends on spatial variations in the BEC density and is known as the ‘quantum pressure’ [33]. It arises due to the kinetic energy term of the GP equation. Neglecting this is equivalent to the T-F approximation, as described in the previous section. Collective excitations can be expressed as small variations of the density n , as

$$n(\mathbf{r}, t) = n_0(\mathbf{r}, t) + \delta n(\mathbf{r}, t), \quad (2.17)$$

where δn are small fluctuations about the background condensate density n_0 . Linearizing Eq. (2.14) and (2.15) with (2.17) and treating δn and \mathbf{v} as small, gives the following set of coupled differential equations.

$$\frac{\partial \delta n}{\partial t} + \nabla \cdot (n_0 \mathbf{v}) = 0 \quad (2.18)$$

$$m \frac{\partial v}{\partial t} + \nabla \delta \tilde{\mu} = 0. \quad (2.19)$$

where $\delta \tilde{\mu}$ is obtained by linearizing $\tilde{\mu}$. Differentiating Eq. (2.18) and substituting the value of $\partial \mathbf{v} / \partial t$ from Eq. (2.19), we get

$$m \frac{\partial^2 \delta n}{\partial t^2} = \nabla \cdot (n_0 \nabla \delta \tilde{\mu}) \quad (2.20)$$

Under the T-F approximation, the quantum pressure term in Eq. (2.16) can be neglected.

Furthermore assuming $|\nabla n_0| \ll |\nabla \delta n|$, Eq. (2.21) can be expressed as

$$\frac{\partial^2 \delta n}{\partial t^2} = \nabla \cdot (c^2 \nabla \delta n) \quad (2.21)$$

where $c^2 = gn_0/m$. Eq. (2.21) is a wave equation representing sound waves or phonons propagating in the BEC with a local velocity $c(\mathbf{r})$ which depends on the local density $n_0(\mathbf{r})$.

2.2.3 Damping of Low-energy Excitations

Starting from the mean-field time-dependent GP equation (Eq. (2.10)), Sec. 2.2.2 derives the propagation of collective excitations as solutions to an undamped wave equation (Eq. (2.21)). Due to absence of a damping term ($\propto \partial \delta n / \partial t$) in Eq. (2.21), one expects the phonons to be long lived. However, collective excitation in a finite temperature BEC always damp with time [39, 46, 47]. To understand the mechanisms of phonon decay, we need to look beyond the mean-field GP approach and consider interactions between the different collective and thermal excitations. Eq. (2.9) describes the time-evolution of the condensate. A full solution to Eq. (2.9) would involve coupling between the different excitations, which becomes apparent as one retains terms proportional to $\hat{\Psi}^{\prime 3}(\mathbf{r}, t)$ and $\hat{\Psi}^{\prime 4}(\mathbf{r}, t)$ in the hamiltonian H [33, 46]. The system could no longer be described as a closed system and finite temperature effects need to be considered.

Two mechanisms for phonon decay in BECs are Landau [46] and Beliaev [48] damping. While Beliaev damping is four-wave mixing process where an elementary excitation decays into two or three lower energy excitation, Landau damping results from

the interaction of phonons with thermal excitations. Since the available final state phase-space is very restricted for low-energy initial excitations, Beliaev damping is usually not the dominant mechanism. Landau damping occurs due to scattering of a low energy phonon with thermal excitations, which leads to phonon creation or annihilation. This form of damping depends on the temperature and arises due to the presence of thermal atoms in the system.

In the next chapter, I will describe how collective excitations in a BEC can be used to simulate analogous systems for studying cosmological phenomena. The concepts developed in this chapter will be useful in establishing the analogy between fields in cosmology and phonons in a moving BEC.

Chapter 3: Analogue Gravity

The broad goal of analogue gravity experiments is to mimic cosmological processes involving general relativity and field theory in controllable systems [49, 50]. The genesis of this field can be traced back to Unruh’s seminal paper [51] from 1981, where he established an analogy between fields at a black hole event horizon and sound waves in a moving fluid. His focus was to study mechanisms and assumptions involved in Hawking’s prediction of black hole evaporation [52, 53]. Since the experimental investigation of Hawking radiation is virtually impossible, developing analogous systems to study quantum thermal radiation could improve our understanding of the evaporation process at trans-Planckian length scales, where many of Hawking’s assumptions might not hold.

Unruh argued that analogous to light at a black hole event horizon, sound waves with speed c_s traveling in a fluid flowing at supersonic velocities $v > c_s$ will not be able to travel upstream. Fig. 3.1 schematically illustrates this idea by displaying the time-evolution of acoustic wavefronts on a 2D space as the fluid velocity v and sound speed c_s are varied. The colored circles represent acoustic wavefronts on the $\mathbf{e}_x - \mathbf{e}_y$ spatial plane. The different colors correspond to different times, as indicated by the color bar to the left. Fig. 3.1 (a) shows the time evolution for four different values of the fluid velocity v with the same speed of sound c_s across all four situations. The horizontal axis

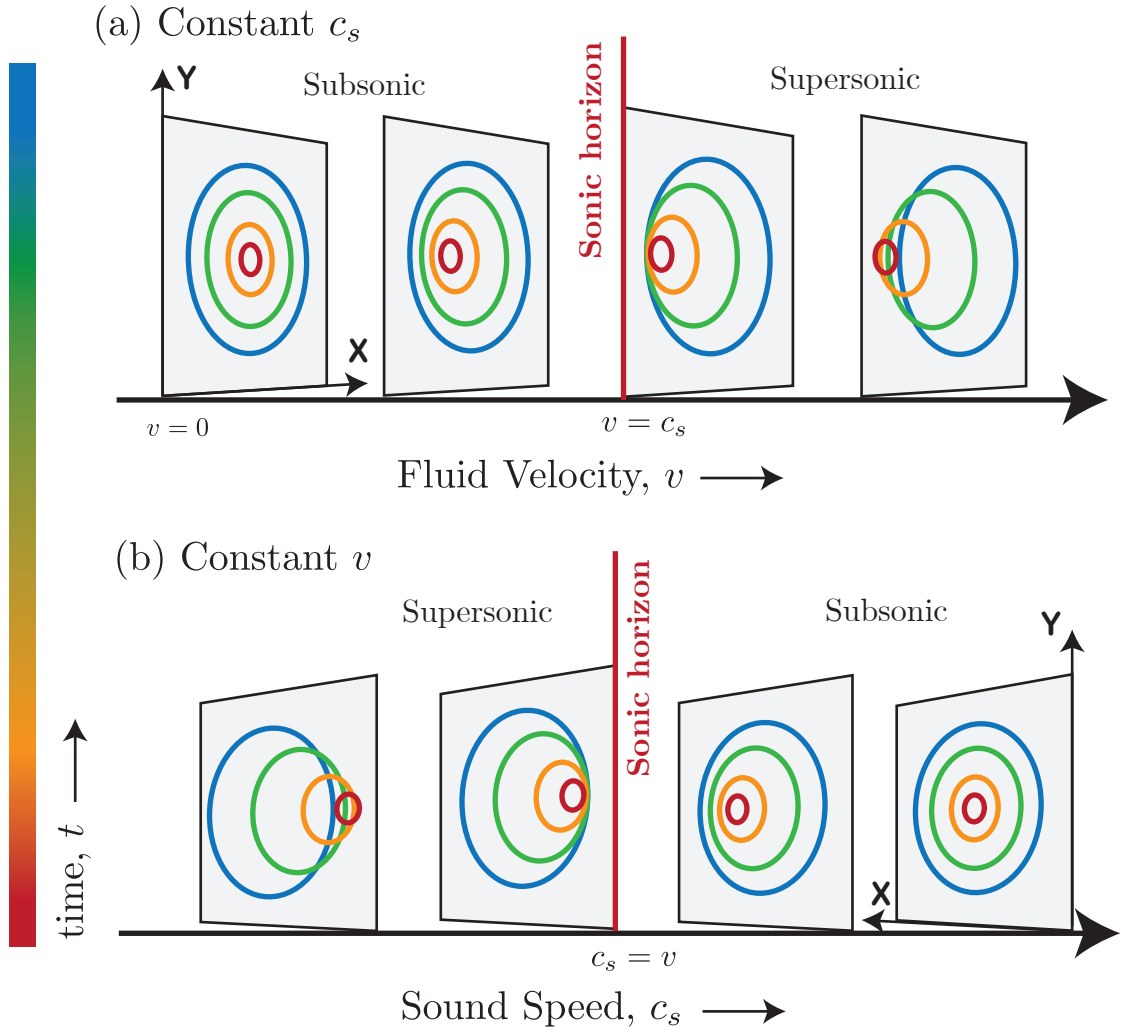


Figure 3.1: A moving fluid creating an acoustic horizon when supersonic flow avoids upstream movement of sound waves. The colored circles represent time-evolution of acoustic wavefronts in the fluid space-time. $\mathbf{e}_x - \mathbf{e}_y$ plane represents spatial coordinates. Time is expressed in different colors according to the color bar to the left. The vertical red lines denotes the sonic horizon. (a) and (b) depict how the wavefront time-evolution changes with varying fluid velocity v and sound speed c_s , respectively.

represents the control parameter v . The leftmost $\mathbf{e}_x - \mathbf{e}_y$ panel in Fig. 3.1 (a) corresponds to $v = 0$, where acoustic waves expand uniformly in all directions. However, as the fluid attains a non-zero velocity, this is no longer true. Beyond the sonic horizon (vertical red line), where the fluid velocity equals the speed of sound, the acoustic waves can no

longer travel upstream, creating causally disconnected regions in the fluid space-time. Fig. 3.1 (b) shows a similar situation where the fluid velocity v is the same across all the panels, but the speed of sound c_s is varied. Here the panels are in reverse order because now the region left of the red line represents supersonic behavior. In this chapter I will introduce the idea of simulating cosmological phenomena in BECs and formally establish the analogy in terms of a wave equation in curved space-time.

3.1 Previous Experiments

Due to their high degree of quantum coherence and ease of control and manipulation, BECs were always considered a promising candidate for developing Unruh's sonic analogues of Hawking radiation. Early proposals for BEC analogues involved creating sonic horizons in long and thin quasi 1D condensates by explosively expanding them or tuning interactions via Feshbach resonances [54,55]. In addition, several proposals involved the implementation of the de Laval nozzle in linear traps to obtain regions of supersonic and subsonic flows in the same condensate, thereby creating a sonic horizon [21,56–58]. A detailed description of the proposed de Laval nozzle implementation can be found Ref. [56]. Despite these theoretical proposals, major experimental progress wasn't made until 2010, when Jeff Steinhauer's group realized a sonic black hole for the first time in a BEC [59]. By accelerating an elongated harmonically-trapped BEC across a step-like potential (also called "waterfall potential"), they achieved fluid velocities an order of magnitude greater than the speed of sound. This resulted in the creation of black and white hole horizons in the same condensate, which they exploited in later experiments to observe self-amplifying

Hawking radiation [23] and spontaneous Hawking radiation [24, 60].

Apart from simulating Hawking radiation, several BEC experiments have exploited the sonic analogue for simulating other cosmological phenomena. Notable among them is the observation of Sakharov oscillations, where synchronously generated sound waves were created by quenching the atomic interactions via Feshbach resonances [22]. Another interesting experiment was the observation of sonic analogue of dynamical Casimir effect, which was performed by modulating the density of a BEC [61]. The goal of our experiments is to simulate cosmological phenomena associated with the inflationary dynamics of the early universe. In particular, we wish to study the evolution of scalar fields in expanding and contracting universes. We use a toroidally shaped BEC, which serves as our analogous universe. We expand and contract our BEC universe by dynamically varying the radius of the toroid during an experiment. Such a toroidal BEC has azimuthally traveling collective phonon modes, which serve as our fluctuating scalar fields. These phonon modes can be created either by intentionally imprinting them or they could also be spontaneously generated. Our experiments study the evolution of these phonon modes as the BEC universe is expanded or contracted.

3.2 BEC Phonon Wave Equation and the Space-time Metric

Unruh's analogy relies on the condition that acoustic scalar fields satisfy the wave equation in curved space-time. Formally the geometric and causal structure of space-time is expressed in the form of metric tensors. For Unruh's analogy to hold, the metric tensor associated with acoustic waves in fluids should algebraically depend on sound speed and

the medium's velocity. Ref. [49] derives the metric related to the phonon field in a BEC. This section follows that derivation and show that the phonon's metric represents a curved space-time.

The time evolution of a BEC wavefunction $\psi(\mathbf{r}, t)$ is given by the time-dependent GP equation, given by Eq. (2.10). We re-write the equation here.

$$-\frac{\hbar^2}{2m}\nabla^2\psi(\mathbf{r}, t) + V(\mathbf{r})\psi(\mathbf{r}, t) + g|\psi(\mathbf{r}, t)|^2\psi(\mathbf{r}, t) = i\hbar\frac{\partial\psi(\mathbf{r}, t)}{\partial t}, \quad (3.1)$$

m is the atomic mass, $V(\mathbf{r})$ is the external potential and g is the GP interaction constant. The wavefunction can be expressed in terms of the atomic density $n(\mathbf{r}, t)$ and phase $\phi(\mathbf{r}, t)$ as $\psi(\mathbf{r}, t) = \sqrt{n(\mathbf{r}, t)}e^{i\phi(\mathbf{r}, t)}$. Substituting this in Eq. (3.1) and comparing the real and imaginary parts gives the continuity equation

$$-\frac{\partial n}{\partial t} = \frac{\hbar}{m}\nabla \cdot (n\nabla\phi), \quad (3.2)$$

This equation is same as Eq. (2.14) with \mathbf{v} replaced by $(\hbar/m)\nabla\phi$. We also obtain an equation analogous to Euler equation of fluid dynamics,

$$-\hbar\frac{\partial\phi}{\partial t} = -\frac{\hbar^2}{2m\sqrt{n}}\nabla^2\sqrt{n} + \frac{\hbar^2}{2m}(\nabla\phi)^2 + V + gn. \quad (3.3)$$

Since we are dealing with only low-energy and long-wavelength collective excitation, the relevant length scales are larger than the healing length $\xi = \hbar/\sqrt{mgn}$. As a result the first term in Eq. (3.3) can be neglected, resulting in the hydrodynamic approximation. We

express the condensate density and phase as

$$n(\mathbf{r}, t) = n_0(\mathbf{r}, t) + \delta n(\mathbf{r}, t), \quad \text{and} \quad \phi(\mathbf{r}, t) = \phi_0(\mathbf{r}, t) + \delta\phi(\mathbf{r}, t), \quad (3.4)$$

where δn and $\delta\phi$ are small fluctuations about the background condensate density n_0 and phase ϕ_0 . Linearizing Eq. (3.2) and (3.3) with (3.4) gives the following set of coupled differential equations.

$$\frac{\partial \delta n}{\partial t} = -\frac{\hbar}{m} \nabla \cdot [n_0 \nabla \delta\phi + \delta n \nabla \phi_0] \quad (3.5)$$

$$-\hbar \frac{\partial \delta\phi}{\partial t} = \frac{\hbar^2}{m} \nabla \phi_0 \cdot \nabla \delta\phi + g \delta n - \frac{\hbar^2}{2m} \hat{D}_2 \delta n, \quad (3.6)$$

where \hat{D}_2 represents a second order differential operator. By substituting the value of δn from Eq. (3.6) into Eq. (3.5), we obtain a partial differential equation (PDE) for $\delta\phi$. This PDE can be expressed in terms of the (3+1) dimensional space time coordinates $x^\mu \equiv (t; x^i)$ as

$$\partial_\mu (f^{\mu,\nu} \partial_\nu \delta\phi) = 0, \quad (3.7)$$

where the tensors $f^{\mu,\nu}$ are given by

$$\begin{aligned} f^{0,0} &= - \left[g - \frac{\hbar^2}{2m} \hat{D}_2 \right]^{-1} \\ f^{0,j} &= - \left[g - \frac{\hbar^2}{2m} \hat{D}_2 \right]^{-1} \frac{\hbar}{m} \nabla^j \phi_0 \\ f^{i,0} &= - \frac{\hbar}{m} \nabla^i \phi_0 \left[g - \frac{\hbar^2}{2m} \hat{D}_2 \right]^{-1} \\ f^{i,j} &= \frac{n_0 \delta^{i,j}}{m} - \frac{\hbar}{m} \nabla^i \phi_0 \left[g - \frac{\hbar^2}{2m} \hat{D}_2 \right]^{-1} \frac{\hbar}{m} \nabla^j \phi_0 \end{aligned} \quad (3.8)$$

The acoustic compton wavelength $\lambda_c = \hbar/mc_s$ sets a lower limit on the length scale of the problem, where $c_s = \sqrt{gn/m}$ is the speed of sound. Since λ_c corresponds to the BEC healing length ξ , the contribution of the second order differential operator \hat{D}_2 can be neglected as is done in the Thomas-Fermi (T-F) approximation. The tensors $f^{\mu,\nu}$ can now be represented by just numbers. By introducing a tensor $g^{\mu,\nu}$ which satisfies $\sqrt{-g} g^{\mu,\nu} = f^{\mu,\nu}$, Eq. (3.7) can be expressed as

$$\frac{1}{\sqrt{-g}} \partial_\mu (\sqrt{-g} g^{\mu,\nu} \partial_\nu \delta\phi) = 0, \quad (3.9)$$

where g is the metric $g^{\mu,\nu}$'s determinant. This effective metric $g^{\mu,\nu}$ describes a curved Lorentzian geometry. The effective wave equation (3.9) for the scalar field ϕ is analogous to that observed by a massless scalar field over curved space-time. It is important to note that even though the underlying fluid motion is Newtonian and non-relativistic with a space-time metric $\eta_{\mu,\nu} \equiv (\text{diag}[-c_{\text{light}}^2, 1, 1, 1])_{\mu,\nu}$, the phonon scalar field ϕ evolves on a curved space-time given by the metric $g_{\mu,\nu}$. This establishes an analogy between phonons in a flowing BEC and scalar fields in the curved space-time of the universe.

3.3 Wave Equation in a Toroidal BEC

The previous section dealt with deriving the wave equation for phonons in a BEC of arbitrary geometry. For our analog cosmology experiments, we use a toroidally shaped BEC. This section focuses on that and derives the corresponding wave equation. It is based on Ref. [62] which derives the wave equation starting from the action of the GP equation and then applying Hamilton's principle of least action. Ref. [62] represents the

action of the GP equation S for a condensate with density and phase variations given by Eq. (3.4) in the T-F approximation. The resultant action can be expressed as

$$S = \frac{\hbar^2}{2g} \int dt d^3x \sqrt{h} \left[\left[\frac{\partial}{\partial t} + \nabla\phi \cdot \nabla \delta\phi \right]^2 - c^2 h^{ij} \frac{\partial \delta\phi}{\partial x_i} \frac{\partial \delta\phi}{\partial x_j} \right], \quad (3.10)$$

where h^{ij} is the euclidian metric, such that $h_{ij}x^i x^j$ is the spatial line element and $h = \det(h_{ij})$. When applied to co-moving cylindrical coordinates (ρ, θ, z) , such that $\rho = r - R(t)$, where $R(t)$ is the time-varying mean radius, Eq. (3.10) becomes

$$S = \frac{\hbar^2}{2g} \int dt d\theta dz d\rho (R(t) + \rho) \left[\left[\left(\frac{\partial}{\partial t} + \nabla^\rho \phi \frac{\partial}{\partial \rho} + \nabla^z \phi \frac{\partial}{\partial z} \right) \delta\phi \right]^2 - c^2 h^{ij} \frac{\partial \delta\phi}{\partial x_i} \frac{\partial \delta\phi}{\partial x_j} \right]. \quad (3.11)$$

Since we are concerned only with the low-energy azimuthal excitations, Eq. (3.11) is integrated along the radial (ρ) and azimuthal (θ) directions. This gives

$$S = \frac{\hbar^2}{4\pi g} \int dt d\theta \mathcal{V} \left[\left(\frac{\partial \delta\phi}{\partial t} \right)^2 - \frac{c_\theta^2}{R^2} \left(\frac{\partial \delta\phi}{\partial \theta} \right)^2 \right], \quad (3.12)$$

where the volume of the condensate \mathcal{V} and azimuthal speed of sound c_θ is given by

$$\mathcal{V} = 2\pi \int dz d\rho (R + \rho), \quad \text{and} \quad c_\theta^2 = \frac{2\pi R}{\mathcal{V}} \int dz d\rho \frac{c^2}{1 + \rho/R}. \quad (3.13)$$

Note that the term containing ρ doesn't contribute to \mathcal{V} because of its odd symmetry. Under a thin ring approximation ($\rho/R \ll 1$) it doesn't contribute to c_θ as well. By applying Hamilton's principle of least action to the action in Eq. (3.12), we get the wave

equation

$$\left(\partial_t^2 + \frac{\dot{\mathcal{V}}}{\mathcal{V}} \partial_t - \frac{c_\theta^2}{R} \partial_\theta^2 \right) \delta\phi = 0. \quad (3.14)$$

Eq. (3.14) describes the evolution of scalar fields in a toroidal BEC. The term proportional to the change in volume $\frac{\dot{\mathcal{V}}}{\mathcal{V}}$ is analogous to the cosmological phenomenon of Hubble friction which is responsible for exponentially attenuating scalar fields in an expanding universe. In Chapter 6, I will discuss an experiment where we exploit this analogy and simulate Hubble friction in a toroidally shaped BEC.

Chapter 4: Experimental Apparatus

Every successful run of our experiment involves cooling gaseous sodium atoms to quantum degeneracy, shaping them using arbitrary two-dimensional (2D) Optical Dipole Traps (ODT), and acquiring data by directly imaging the atomic sample. In this chapter, I will describe the apparatus we built to perform the above steps. Compared to the previous version of this experiment at NIST, we made significant modifications in this setup. The NIST experiment used a glass cell, but we designed this experiment using a stainless steel vacuum chamber. Fig. 4.1 shows a Computer Aided Design (CAD) diagram of our vacuum chamber. It consists of a source and science chamber maintained at high and ultra-high vacuum, respectively. Atoms are pre-cooled in the source chamber in a 2D Magneto-Optical Trap (MOT). Design details of our 2D MOT are covered in Chapter 5. As shown in Fig. 4.1, the pre-cooled atoms are then transferred from the source to the science chamber using a push beam. I will first give an overview of the vacuum system, then describe the laser cooling setup, followed by a detailed description of the optical system design used for creating arbitrary shaped quasi 2D BECs. Finally, I will examine some of the imaging challenges particular to our experiment and our techniques to overcome them.

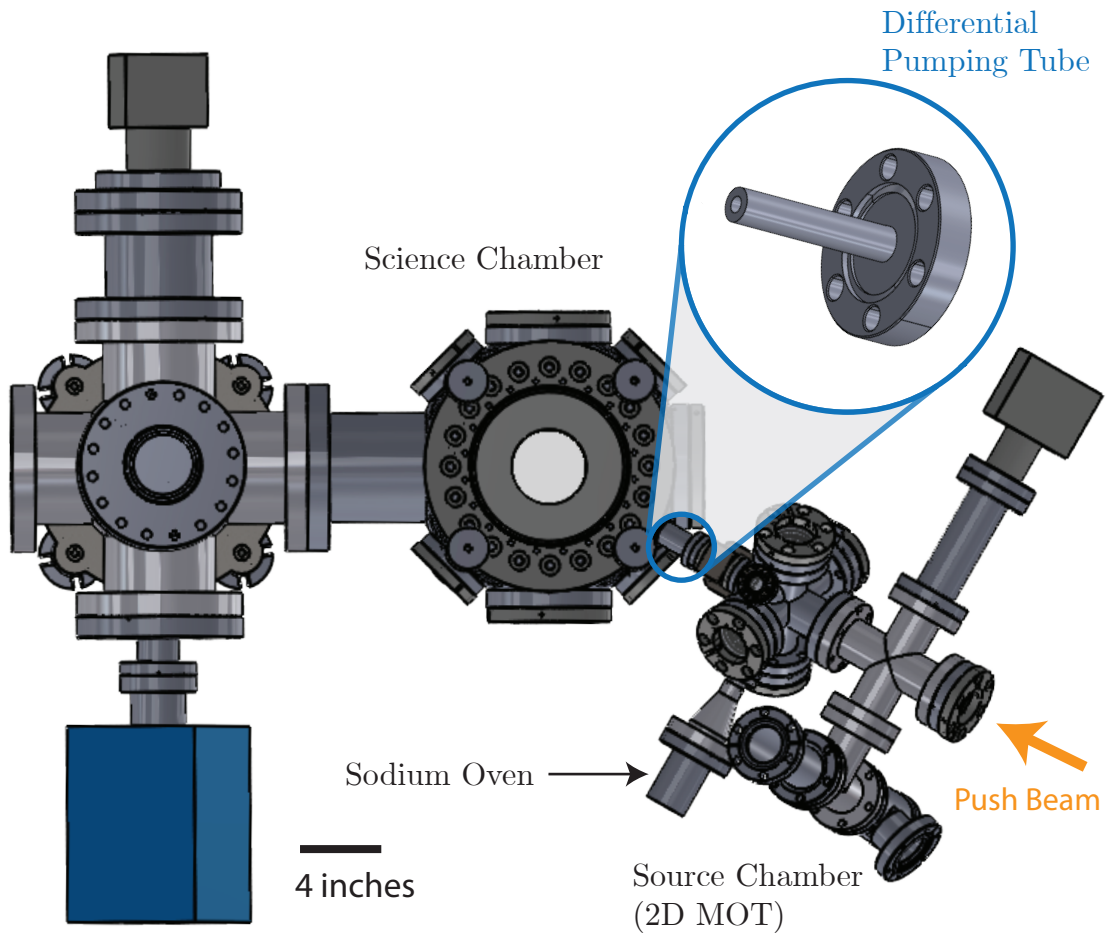


Figure 4.1: Schematic of the vacuum chamber. The source chamber, science chambers, and the sodium oven are indicated. The blue circle points to the location of the differential pumping tube, with the inset showing a schematic of the tube. The yellow line indicates the push laser beam used for transferring atoms from the source to the science chamber.

4.1 Vacuum Chamber

In the absence of vacuum, atoms collide with air molecules gaining enough energy to escape their trapping potentials. This problem worsens if the traps are shallow, as is often the case in ultracold atom experiments, our final ODTs being less than $1 \mu\text{K}$ deep. Moreover, in our experiments, we attain quantum degeneracy by forced evaporation in a

magnetic and optical dipole traps. The efficiency of this technique relies on having long vacuum-limited trap lifetimes. Because of these reasons, quantum degenerate gases can only be produced in Ultra High Vacuum (UHV) conditions.

We perform our experiments in a stainless steel UHV chamber pumped with getter, ion, and titanium sublimation pumps. Since we plan on adding highly magnetic Erbium (magnetic moment $7 \mu_B$) to this system, the chamber is custom-made by Kimball Physics with non-magnetic 316L stainless steel. The vacuum chamber is divided into two sections, source and science chamber, as shown in Fig. 4.1. The source section contains the atomic source, which is heated to about 250 °C, to obtain a vapor of sodium atoms. Given the metal outgassing at these temperatures, maintaining UHV conditions is not possible. Therefore we separate the source section from the science chamber using a differential pumping tube. Fig. 4.1 denotes the location and shows a schematic of the differential pumping tube. Fig. 4.2 is a mechanical drawing of the tube's cross section. The source side is maintained at a pressure of about 10^{-8} torr while the science chamber is maintained at 1.2×10^{-10} torr. Due to its small conductance, the differential pumping tube can hold this pressure differential in steady state. We monitor these pressures with two Agilent UHV 24P ion gauges, one on the source chamber and the other on the science chamber. The science chamber is pumped using a SAES D-500 getter and a Gamma Vacuum 45S ion pump in steady-state. In addition, we have a titanium sublimation pump which is occasionally activated to counter a gradual increase in the science chamber pressure. On the source side, pumping is achieved using a SAES D-100 getter pump.

Gases adsorbed in the metallic chamber limit the vacuum's quality. Therefore, while constructing this chamber, we baked it in two stages. First, we performed a week-

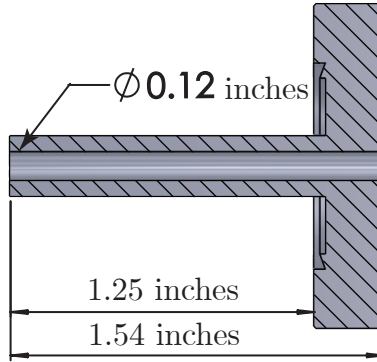


Figure 4.2: Cross-section of the differential pumping tube.

long high-temperature bake at 400 °C without any vacuum viewports. This was performed in a kiln while a turbo pump pumped out most of the adsorbed hydrogen. The second stage was a month-long bake with the vacuum viewports at around 180 °C to outgas water vapor absorbed in the chamber walls. This brought the pressure down to low 10^{-8} torr. After the two bakes, we activated the getter and ion pumps which decreased the pressure to 2.8×10^{-10} torr, followed by titanium sublimation pump activation, which achieved 1.2×10^{-10} torr. The goal of maintaining UHV in the science chamber is to minimize collisions of cold atoms with air molecules. Therefore, the vacuum limited lifetime of an atomic trap serves as a metric to quantify experimental limitations. We measure the drop in atom number in a magnetic trap as a function of the hold duration and measure the lifetime to be 23 s.

4.2 Laser Frequency Stabilization

In our experiment, we perform laser cooling of ^{23}Na atoms along the D_2 line of atomic sodium. Fig. 4.3 shows the various hyperfine levels of the sodium ground

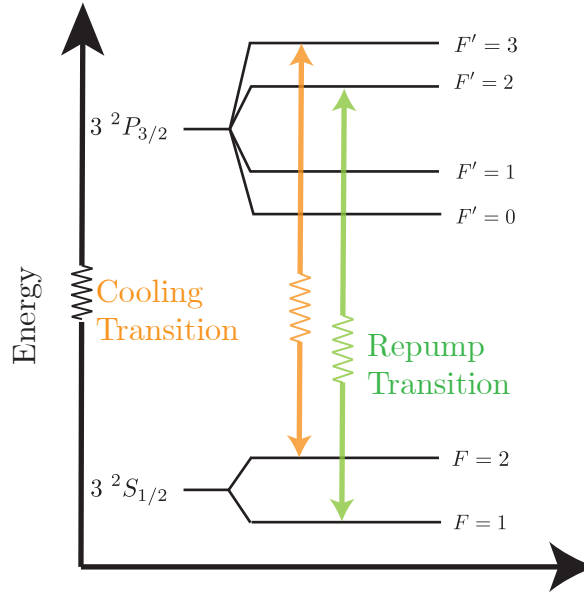


Figure 4.3: Energy levels for the ^{23}Na D_2 transition [2]. The yellow and green lines indicate the cooling and repump transitions separated in frequency by 1.7 GHz.

state $|3^2S_{1/2}\rangle$ and the excited state $|3^2P_{1/2}\rangle$ corresponding to the D_2 transition [2]. We perform Doppler and sub-Doppler cooling along the $|3^2S_{1/2}, F = 2\rangle$ to $|3^2P_{1/2}, F' = 3\rangle$ transition with laser light at 589 nm, as shown by the yellow line in Fig. 4.3. To recycle the atoms which spontaneously decay from the excited state into the $F = 1$ ground state, we add a repump beam corresponding to the $|3^2S_{1/2}, F = 1\rangle$ to $|3^2P_{1/2}, F' = 2\rangle$ transition, as shown by the green line in Fig. 4.3. This beam is roughly 1.7 GHz blue detuned to the cooling line.

For laser cooling, we use two commercial Toptica DL-Pro 589 nm laser systems, one at the cooling transition and the other at the repump transition. Fig. 4.4 shows a schematic of these commercial lasers [3]. It consists of an External Cavity Diode Laser (ECDL) followed by a Tapered Amplifier (TA) and a Second Harmonic Generation (SHG) crystal in a ring cavity. The diode emits light in the infrared (IR), which upon

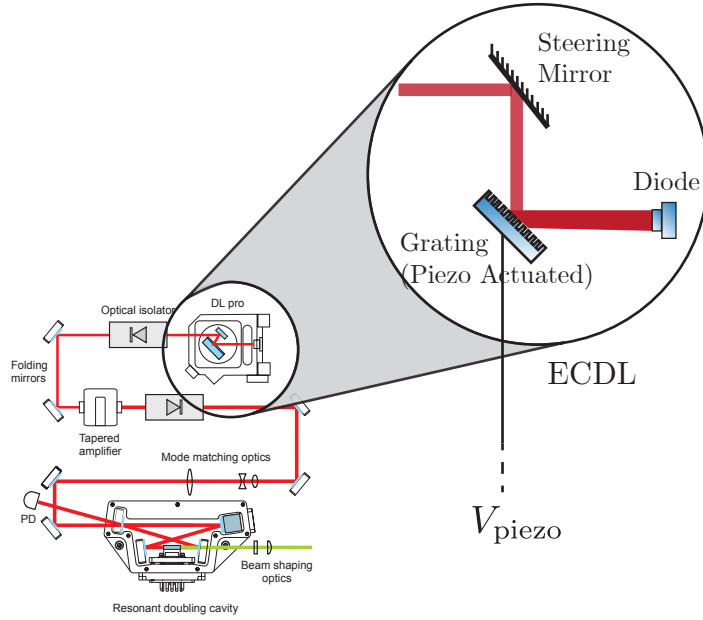


Figure 4.4: Schematic of the optical setup inside the Topptica DL-pro laser [3]. The inset shows a magnified view of the ECDL, indicating the piezo actuated grating, which can be externally controlled via the voltage V_{piezo} .

amplification through the TA, is frequency-doubled to 589 nm. The ECDL has a piezo actuated diffraction grating in the Littrow configuration, as shown in the inset of Fig. 4.4. To control the laser frequency, we provide a feedback signal to this piezo and the diode current. The overall feedback signal is represented by V_{piezo}

The linewidths of the two Topptica DL-Pros lasers is about 2π 30 kHz, estimated by a self heterodyne measurement with 2 km long optical fiber and an Acousto Optical Modulator (AOM). Though these linewidths are much smaller than the 2π 9.8 MHz natural linewidth of the sodium D_2 line, the lasers have a long-term frequency drift of 0.8 MHz over 30 minutes, measured on an Angstrom WSU2 wavemeter. To correct these drifts, we feedback the cooling transition Topptica laser and lock it to the D_2 line obtained via Saturation Absorption Spectroscopy (SAS). Fig. 4.5 is a schematic of the

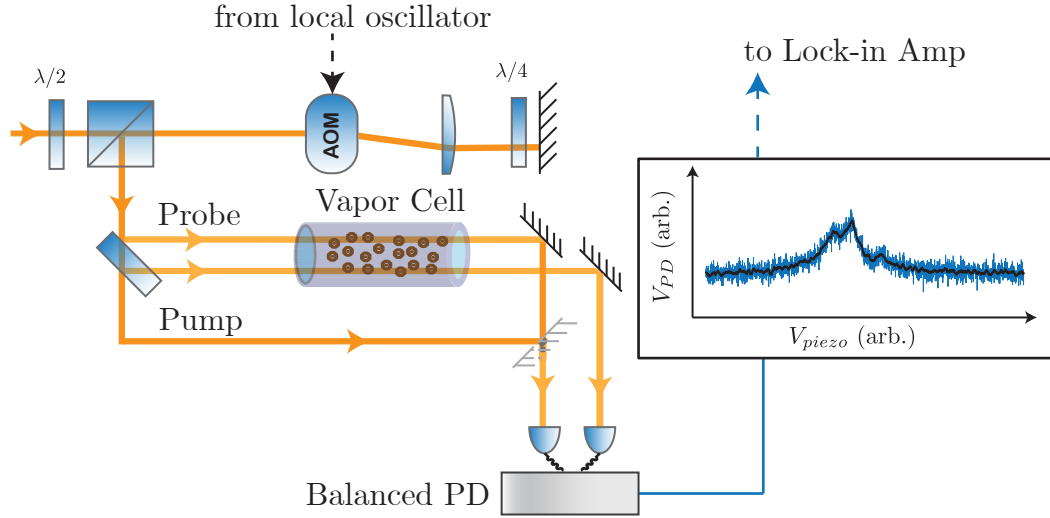


Figure 4.5: Optical schematic of the SAS setup. The yellow lines indicate light from a Toptica DL-pro laser which is first upshifted by 150 MHz and then split into pump and probes. The signal from a balanced photodetector, as shown in the rectangular box, is sent to a lock-in amplifier.

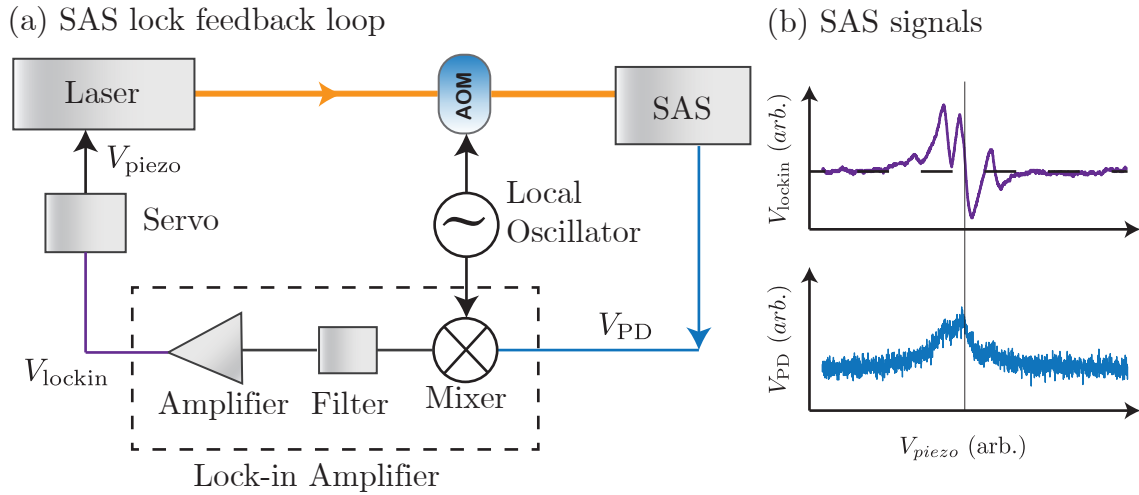


Figure 4.6: (a) Lock-in scheme to obtain the derivative of the SAS absorption signal V_{PD} . The blue and purple lines represent V_{PD} and the derivative signal V_{lockin} respectively. The dashed box indicates the components of a lock-in amplifier. The local oscillator is a Voltage Controlled Oscillator (VCO) that drives the AOM. The servo generates the signal V_{piezo} to control the laser frequency. (b) V_{PD} and V_{lockin} indicated in blue and purple, respectively.

SAS setup. We perform SAS on the crossover of the $|3^2S_{1/2}, F = 2\rangle$ to $|3^2P_{1/2}, F' = 2\rangle$ and $|3^2S_{1/2}, F = 2\rangle$ to $|3^2P_{1/2}, F' = 3\rangle$ transitions. Light from the bare laser is up-shifted by double passing through a 75 MHz AOM and then sent to the vapor cell heated to 150 °C. This beam is split into two low-intensity 40 μ W probe beams and a 1.1 mW pump beam. One of the probe beams is used to obtain a Doppler-free signal. The other probe is subtracted from the Doppler-free signal to eliminate the Doppler broadened dip on a balanced photodetector. The Doppler-free spectroscopy signal V_{PD} thus obtained is shown in the inset of Fig. 4.5. This signal is symmetric about the transition, and therefore, does not give any information about which direction the piezo voltage needs to be driven to correct the drift. However, the phase of the electric field associated with the transmitted probe has odd symmetry about the atomic resonance. To extract this phase information, we perform frequency modulation of the SAS laser beam and use a lock-in amplifier to get a signal proportional to the derivative of the SAS absorption signal V_{lockin} [63]. Fig. 4.6 shows a schematic of the frequency modulation and lock-in scheme used. For the frequency modulation, we dither an AOM at a modulation frequency of 50 kHz. Once the cooling laser is locked to the atomic transition, the repump laser is beatnote locked to the cooling laser in a master-slave configuration. Light from the two locked lasers is frequency shifted using AOMs and then sent to the experiment table via single-mode optical fibers. Tab. 4.1 lists the frequency and intensities of the different beams used to address the atoms.

Table 4.1: Detunings and intensities of the different laser cooling beams. For the first five entries, detunings are from the cooling transition. For the last three entries, detunings are from the repump transition. For reference, the saturation intensity for the cooling transition is $I_{\text{sat}} = 6.26 \text{ mW/cm}^2$

Laser Beam	Detuning from transition (MHz)	Intensity (mW/cm ²)
2D MOT cool	-12	0.98
3D MOT cool	-16	1.13
Zeeman Slower(ZS)	-219	20
Push	+9	9
Polarization Gradient Cooling (PGC)	-39 to -16	1.13
2D MOT rep.	-8	30
3D MOT rep	-8	3
Spin Polarization	-26	0.005

4.3 Optical Dipole Traps

We use three far-detuned laser beams to generate ODTs for our experiment. Fig. 4.7 shows the propagation of the three ODT beams with respect to the science chamber. One of them is red-detuned to the atomic transition and is used for evaporative cooling. The other two are blue-detuned and are used in combination to trap atoms in arbitrary 2D potentials. The subsections below discuss the optical setup for all three laser beams.

4.3.1 Red-detuned Optical Dipole Trap

We use a red-detuned ODT for evaporatively cooling atoms to quantum degeneracy. The forced evaporation scheme will be discussed in Chpt. 5. For this ODT, we use a 1064 nm single beam from an IPG ‘YLR30-1064-LP-SF’ Ytterbium fiber laser. 10 W of 1064 nm power is fiber-coupled into an NKT Photonics ‘aeroGUIDE 15 PM SMA-

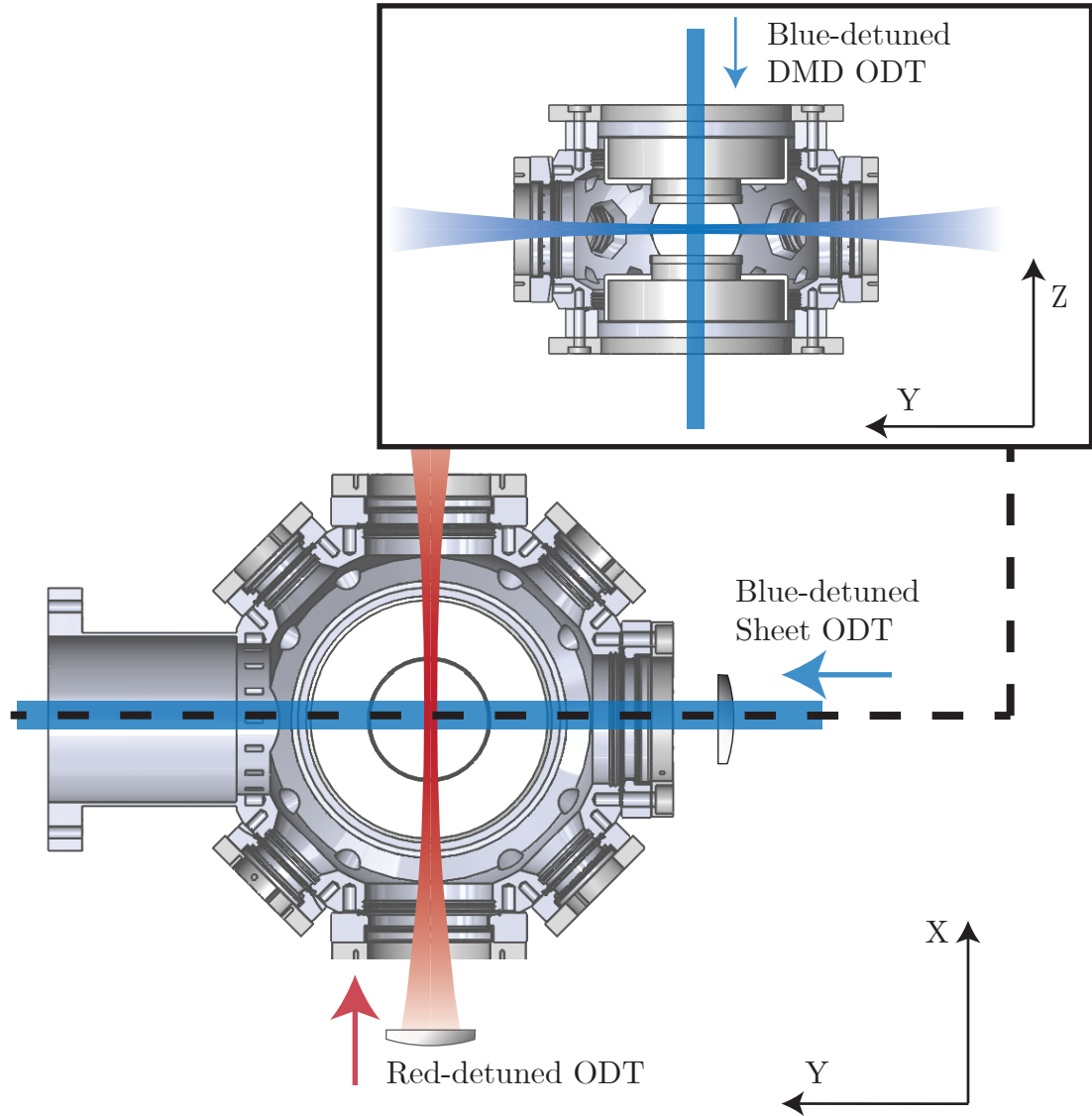


Figure 4.7: Propagation of ODT beams in the science chamber. The main figure shows the red-detuned ODT propagating along positive \mathbf{e}_x and being focused down at the center of the chamber. The blue-detuned sheet ODT propagates along positive \mathbf{e}_y . The inset shows beam propagation on the $\mathbf{e}_y - \mathbf{e}_z$ plane. The blue-detuned DMD ODT propagates along negative \mathbf{e}_z . Gravity acts along negative \mathbf{e}_z .

905' photonic crystal fiber and sent to the experiment table. The light out of the fiber is collimated into a $800 \mu\text{m}$ beam using a LMH-10X-1064 microscope objective with $10\times$ magnification and 0.25 numerical aperture. A 1:5 telescope expands the beam into a 4 mm waist, which is then focused by a 300 mm focal length spherical lens into a beam

waist of $w_0 = 25 \mu\text{m}$ at the plane of the atoms.

4.3.2 Blue-detuned Optical Dipole Trap

Our experiments rely on creating arbitrary shaped 2-dimensional ODT. For this, we use two blue-detuned lasers beams from a 532 nm IPG GLR-30 fiber laser. Blue-detuned laser beams create repulsive potentials and can achieve smaller diffraction limited spot sizes d_{spot} . The diffraction limited spot size is given by $d_{\text{spot}} = \pi\lambda/\text{NA}$, where λ is the wavelength and NA is the numerical aperture of the optical system. Due to their smaller wavelength, blue-detuned ODTs allow us to achieve tighter confinements than red-detuned light. One of the two 532 nm beams is used for vertical confinement (along \mathbf{e}_z) and the other for confinement on the horizontal plane ($\mathbf{e}_x - \mathbf{e}_y$). Fig. 4.8 shows a schematic of the optical system used for vertical confinement. With the help of a cylindrical lens, two spherical lenses, and a π phase plate, we shape the TEM_{00} mode out of a single-mode SM460 optical fiber into an elongated TEM_{01} mode, providing sheet-like confinement for atoms in between the two lobes of the TEM_{01} mode. The vertical width of this sheet trap is about $9 \mu\text{m}$ at the focus of the final lens L_3 . For the planar confinement, we project arbitrary patterns from a Digital Micrometer Device (DMD) onto the plane of atoms through an objective lens stack [64], as shown in Fig. 4.10 (a). The two beams are slightly shifted (≈ 10 MHz) in frequency to avoid any interference effects. Together, they provide arbitrary shaped quasi 2D confinement for BECs.

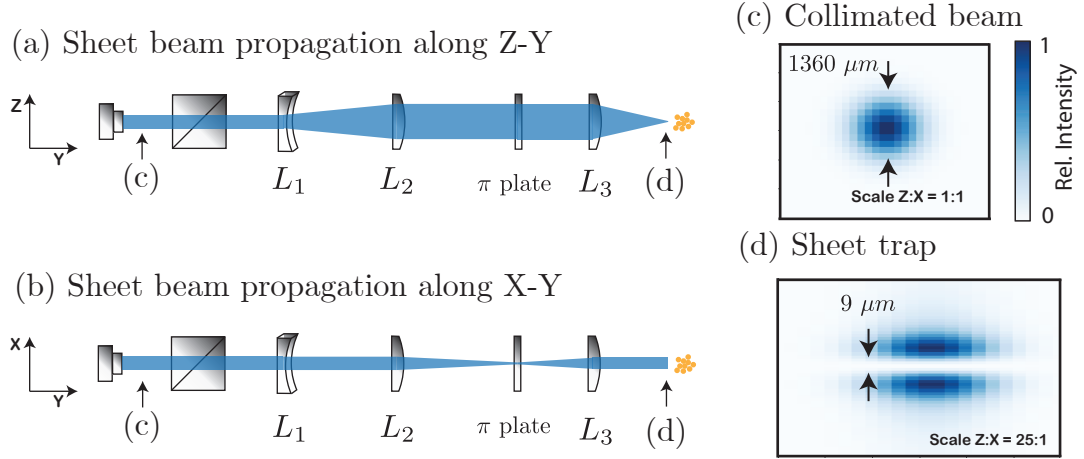


Figure 4.8: Schematic for the sheet trap optical setup. Blue-detuned laser light from a single-mode fiber is collimated and propagated through lenses L_1 , L_2 , L_3 and a π phase plate along the \mathbf{e}_y direction. (a) and (b) shows the beam profile in the $\mathbf{e}_z - \mathbf{e}_y$ and $\mathbf{e}_x - \mathbf{e}_y$ planes, respectively. Figures (c) and (d) show the simulated $\mathbf{e}_z - \mathbf{e}_x$ beam intensity profiles at indicated Y positions, with \mathbf{e}_z along the vertical axis and \mathbf{e}_x along the horizontal. The color bar encodes the relative beam intensity for figures (c) and (d). The atoms, as depicted by the yellow dots, lie close to the front focal plane of lens L_3 . Gravity acts along negative \mathbf{e}_z .

4.3.2.1 Vertical Confinement

The sheet trap is generated using a cylindrical (L_1) and two spherical lenses (L_2 and L_3) and a π phase plate placed at positions, as indicated in Fig. 4.8. The TEM_{00} beam from a single-mode fiber is first collimated into a uniform beam with a $1/e^2$ diameter of $1360 \mu\text{m}$. This then passes first through the cylindrical lens L_1 followed by the spherical lens L_2 . L_1 and L_2 together form a telescope along the vertical direction \mathbf{e}_z thereby magnifying the vertical beam waist by $|f_2/f_1| = 7.5$, where $f_1 = -40 \text{ mm}$ is the focal length of L_1 and $f_2 = 300 \text{ mm}$ is the focal length of L_2 . As a result, the beam at L_2 's front focal plane has a vertical waist $w_z = 5.1 \text{ mm}$, while the horizontal waist gets focused down to a small spot. This elongated beam passes through a π phase plate, which adds

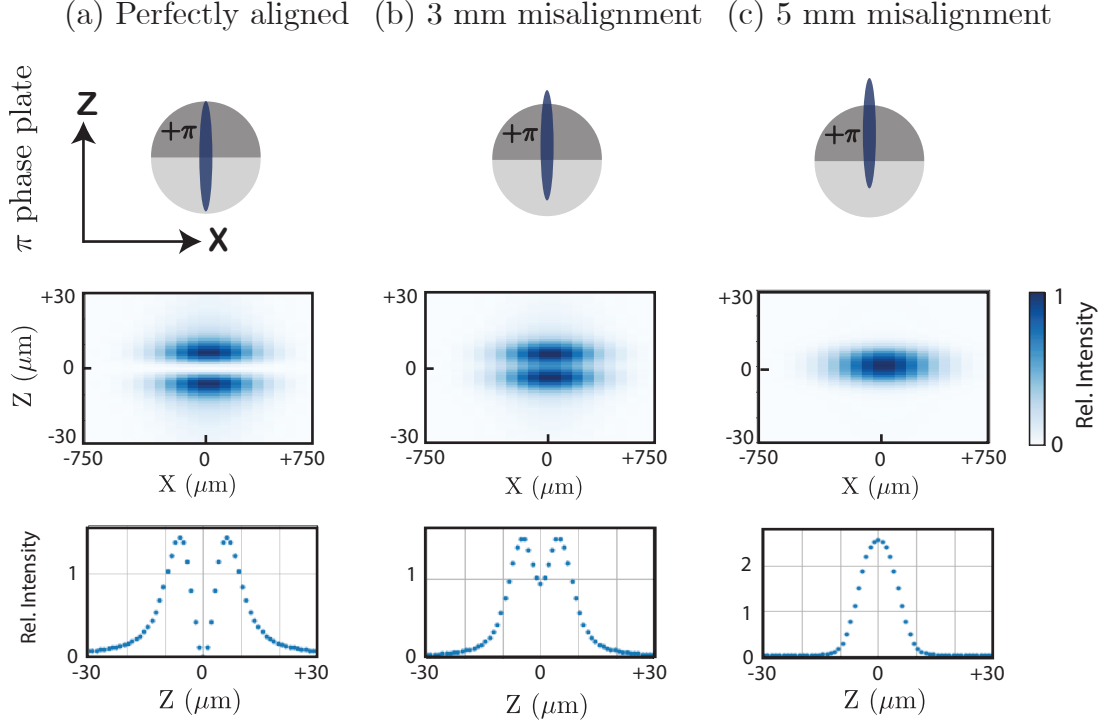


Figure 4.9: Simulations exploring slight vertical misalignment between laser spot and π phase plate. The top panel is a schematic depicting the relative vertical distance between the laser spot and the π phase plate. The elongated beam has a $1/e^2$ beam waist of 5 mm on a phase plate of clear aperture radius 25 mm. The middle panel shows the $\mathbf{e}_z - \mathbf{e}_x$ intensity profile of the beam at the front focal plane of L_3 . The color bar encodes the relative beam intensity for the middle panel. The bottom panel is a vertical cut-out showing the intensity profile along the \mathbf{e}_z axis from the middle panel. (a), (b), and (c) correspond to 0, 3, and 5 mm misalignments, respectively.

a π phase difference between its top ($Z > 0$) and bottom ($Z < 0$) halves [40]. Finally, the beam goes through the final lens L_3 of focal length $f_3 = 200$ mm. L_2 and L_3 form a telescope for the beam along \mathbf{e}_x , while it focuses the \mathbf{e}_z waist into a tight spot. Exploiting the Fourier transform property of lenses, the beam's intensity pattern is determined at the front focal plane of L_3 , as shown in Fig. 4.8 (d) and Fig. 4.9 (a).

The bottom panel of Fig. 4.9 (a) shows that along Z , the intensity has a minimum at $z = 0$, thereby providing vertical trapping. However, along the beam propagation

direction \mathbf{e}_y , the TEM_{01} intensity gradient introduces a not-so-intuitive antitrapping potential, which pushes the atoms away from the focus of the imaging system. Even though the dipole trap potential along the \mathbf{e}_y axis is zero, atoms trapped away from the \mathbf{e}_y axis experience an intensity gradient along \mathbf{e}_y , pushing them away from L_3 's front focal plane. This problem is further exacerbated by slight misalignment in the beam shaping optics. Fig. 4.9 is a simulation of how small misalignments in the π phase plate relative to the beam center can result in blue-detuned light leaking into the dark regions of the sheet trap. As evident from these simulations, a 3 mm misalignment can cause significant distortions to the trapping potential. In our experiment, we use a phase plate with a radius of 25 mm. It is challenging to center this π phase plate on the 5 mm ($1/e^2$ radius) elongated beam to better than 1 mm. Because of these reasons, our final system has some antitrapping, not allowing us to place the BEC at the focus of the sheet trap. Instead, we place the BEC at about a Rayleigh length away from the focus where the antitrapping force is not strong enough to significantly distort the homogeneity of the sheet BEC. Since we do not sit at the beam focus, the resulting trap frequencies are smaller for a given laser power. Taking inspiration from [65], we plan to add a red detuned dipole trap to compensate for this antitrapping potential in future designs.

4.3.2.2 Planar Confinement

For the 2D planar confinement, we use a Texas Instrument DLP7000 DMD. It has a 1024×768 array of individually addressable aluminum micromirrors arranged over a rectangular grid. The DLP7000 has a micromirror pitch of $13.68 \mu\text{m}$ and a maximum

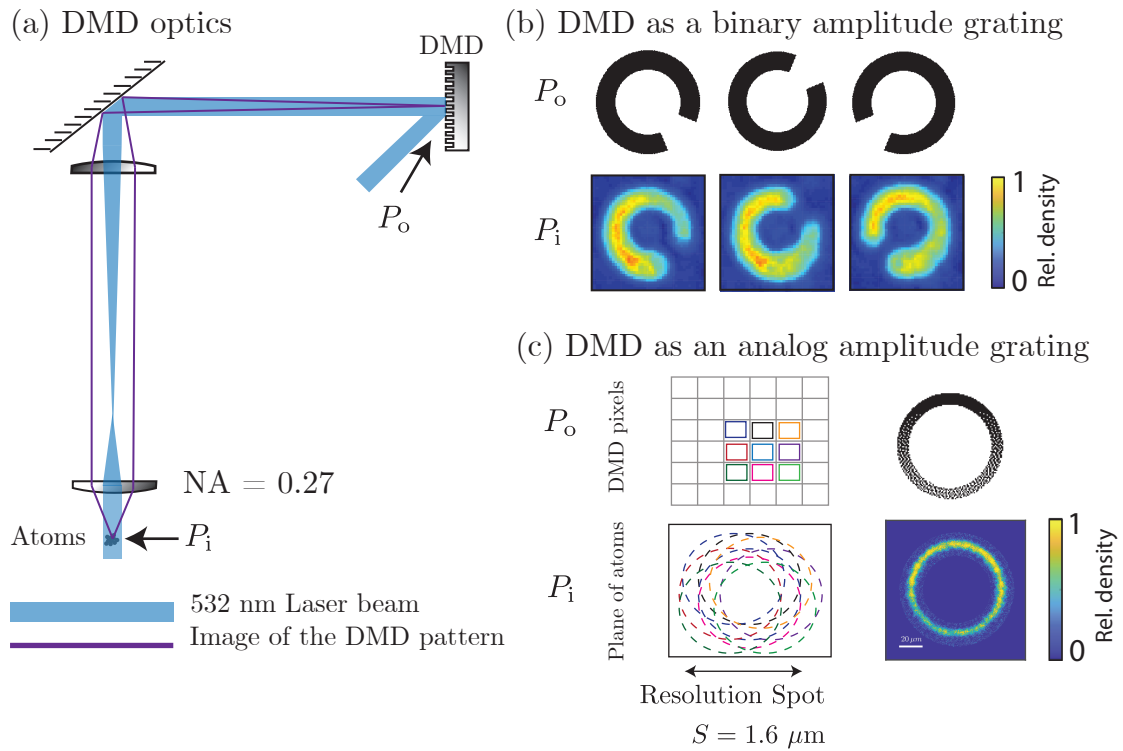


Figure 4.10: (a) Schematic of the DMD optical setup. P_o and P_i refer to the DMD and atom planes, respectively. The purple lines are rays representing imaging of the DMD pattern onto the plane P_i . The blue lines indicate the spatial profile of the collimated laser beam as it travels through the optics. (b) DMD being used as a binary amplitude grating. The top panel shows binary patterns imprinted onto the DMD plane P_o . The dark and bright regions represent micromirrors in the OFF and ON positions, respectively. The bottom panel shows the resultant atomic density distribution on the atom plane P_i . (c) DMD being used as an analog amplitude grating using halftoning. The right panel shows the overlap between the images of adjacent DMD pixels when projected through the imaging system. The right panel shows halftoning implemented in our system.

pattern projection rate of 32 kHz, allowing for a fast dynamic display of patterns essential for our experiments. This is in contrast to phase Spatial Light Modulators (SLM) which have a maximum update rate of a few hundred hertz, making them too slow for our purposes. Fig. 4.10 (a) shows a schematic of the optical imaging system used for the projection of DMD patterns. These micromirrors are bi-stable, limiting the DMD to a binary amplitude grating, as shown in Fig. 4.10 (b). However, one can perform analog

modulation of the dipole trap beam's spatial intensity profile using halftoning techniques. Fig. 4.10 (c) shows how halftoning exploits the limited resolution of the projection optics to create continuous gradients of intensity. Due to the finite size of the Point Spread Function (PSF), the projection of the individual DMD pixels overlaps, creating a continuous gradient in intensity. We use the Jarvis Halftoning algorithm [66] to choose the appropriate binary DMD patterns to achieve this.

Since the DMD is a 2D array of micromirrors, it acts as a diffraction grating. Therefore, care needs to be taken while aligning the DMD optics, to maximize the laser power in only one of the diffraction orders. In our system, the blaze condition is achieved for a 42° incidence angle with respect to the DMD surface. This reflects the first order at a 66° angle. Given our space constraints, such steep angles makes aligning optics difficult. Since we are not starved for 532 nm laser power, we do not operate the DMD in the blaze condition but at a 24° incidence angle which results in a reflection normal to the DMD surface. The normal reflection additionally ensures that the DMD pattern is normal to the optical axis of the imaging system, as shown in Fig. 4.10 (a).

4.4 Imaging

In ultracold atom experiments, observations are made by directly imaging the atomic sample. Our experiments rely on the accurate estimation of the in-situ column density $n_{2D}(x, y)$. These column densities are typically obtained via absorption imaging, where a probe laser beam with detuning δ is made to pass through the atomic sample. The atomic sample with a volume density $n(x, y, z)$ absorbs the probe light, resulting in a decrease in

the transmitted intensity $I(x, y, z)$ given by the Beer-Lampert's law [42, 67]

$$\frac{dI}{dz} = -n \sigma_0 \frac{I}{1 + I/I_{\text{sat}} + (2\delta/\Gamma)^2}, \quad (4.1)$$

where I_{sat} is the saturation intensity, Γ is the natural linewidth, and σ_0 is the absorption cross section. We perform resonant absorption imaging between the stretched states of $|3^2S_{1/2}, F = 2\rangle$ and $|3^2P_{1/2}, F' = 3\rangle$ levels using a σ^- polarized probe. As a result, $\delta = 0$, and $\sigma_0 = 3\lambda_0^2/2\pi$, where λ_0 is the resonance frequency of the transition. Integrating Eq. (4.1) along \mathbf{e}_z gives

$$n_{2D}(x, y) \sigma_0 = -\ln\left(\frac{I_a}{I_p}\right) + \frac{I_p - I_a}{I_{\text{sat}}}, \quad (4.2)$$

where $n_{2D}(x, y) = \int n(x, y, z) dz$ is the column density, $I_p(x, y)$ and $I_a(x, y)$ are the cross-sectional probe intensities before and after absorption, respectively. We use Eq. (4.2) to estimate the column density n_{2D} . The optical density (OD) is defined as $\text{OD} = n_{2D}(x, y) \sigma_0$. Typically, the intensities I_a and I_p are measured by capturing the probe intensities in the presence and absence of atoms. Since I_a and I_b are measured in terms of the camera's photoelectron counts, I_{sat} is calibrated in the same units as well.

4.4.1 Partial Transfer Absorption Imaging

As evident from Eq. (4.2), the transparency of the atomic cloud has a non-linear dependence on the atomic density (n or n_{2D}). Consider the situation of resonant ($\delta = 0$) absorption imaging when $I_p \ll I_{\text{sat}}$. The transmitted probe intensity I_a decreases

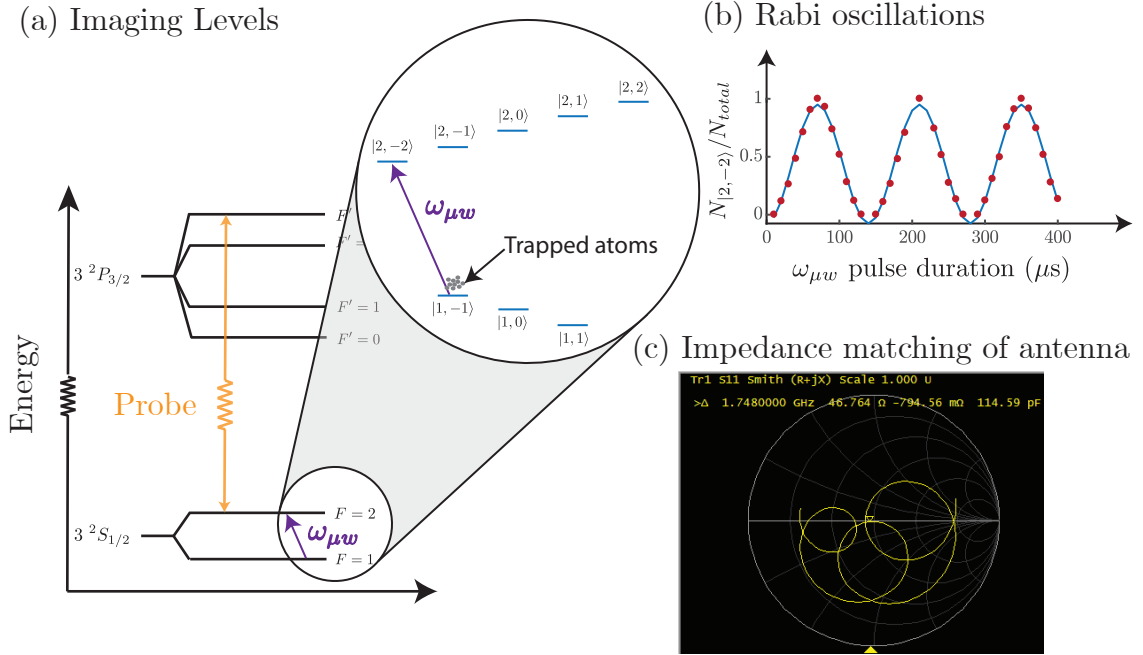


Figure 4.11: Partial Transfer Absorption Imaging. (a) The atomic levels involved in imaging the atomic sample. The inset shows a magnified view of the transitions induced by microwaves. The splitting in the hyperfine levels of the ground state is caused by a constant magnetic field applied throughout the experiment. (b) Rabi oscillations for the transition $|F = 1, m_F = -1\rangle$ to $|F = 2, m_F = -2\rangle$. (c) Smith chart for the impedance matched microwave antenna.

exponentially with an increase in the column density n_{2D} given by

$$I_a = I_p e^{-\sigma_0 n_{2D}}. \quad (4.3)$$

BECs when imaged in-situ have large column densities ($\sigma_0 n_{2D} > 4$). As a result, small density variations lead to a negligible change in I_a . Due to the camera's limited dynamic range, it is often difficult to resolve small density variations in traditional in-situ absorption imaging. For our experiments, we excite collective modes in a BEC and monitor its time evolution. As such, the precision of our measurements relies heavily on being able to resolve small density perturbations accurately. To this end, we image only

a fraction of our atomic sample, thus ensuring that we are far away from the saturation condition of Eq. 4.3 [68]. While the BEC is prepared in the ground state $|3^2S_{1/2}, F = 1, m_F = -1\rangle$, by applying microwaves pulses close to the sodium clock transition of 1.77 GHz, we transfer a small fraction (typically 5%) of the atoms to the $|3^2S_{1/2}, F = 2, m_F = -2\rangle$ state. These atoms are then imaged with a probe beam resonant to the $|3^2S_{1/2}, F = 2\rangle$ to $|3^2P_{1/2}, F' = 3\rangle$ transition. The energy levels and associated transitions are shown in Fig. 4.11 (a). The microwave pulse duration provides a convenient handle on the fraction of atoms imaged as shown in Fig. 4.11 (b). This method has the additional advantage of being minimally destructive, since the atoms which are not transferred to $|3^2S_{1/2}, F = 2\rangle$ do not interact with the probe laser.

For exciting these microwave transitions, the old NIST experiment used a half-wave dipole antenna. Unlike our metallic vacuum chamber, the NIST BEC was produced in a glass cell. Switching from a glass cell to a metallic chamber poses two problems. First, metal surfaces alter the radiation pattern of an antenna. Second, a dipole antenna needs to be placed farther from the atoms than in a glass cell due to the chamber's geometry. As a result, with the NIST half-wave dipole antenna and a 10W amplifier (ZHL-10W-2G+), we obtained an order of magnitude smaller rabi frequency, thereby making our experiment sensitive to decoherence effects due to electronic noise on our bias magnetic fields. The solution to this problem would be a more directional source of microwaves. Commercial horn antennas have excellent directional properties. However, 1.7 GHz horn antennas, such as the RF-Lambda RW430HORN15A, are much bigger than any of our chamber viewports. With these limitations in mind, we decided to use a full-wave loop antenna. This has three advantages. First, a loop antenna can be wound around a viewport,

thereby not restricting optical access. Second, such an antenna can be placed around our recessed top or bottom viewports, closer to the atoms. Third, loop antennas are much more directional than half-wave dipole antennas. Overall, these factors help increase the radiation intensity at the location of the atoms. We measured a rabi frequency of 5 kHz with the loop antenna, which was five times larger than that with a half-wave dipole antenna. Fig. 4.11 (b) shows the Rabi oscillations obtained in our experiment with a full-wave loop antenna. To harness the full power of the microwave amplifier, the loop antenna was impedance matched to the 50Ω output impedance of the amplifier, using a triple stub tuner. Fig. 4.11 (c) is a smith chart of the frequency response of the antenna after being impedance matched at 1.748 GHz with the stub tuner.

4.4.2 Probe Reconstruction

As described in the previous sub-sections, absorption imaging involves measuring the cross sectional intensities I_a and I_p using a camera. Fig. 4.12 is a schematic describing the process. As the probe moves through the atomic sample, atoms absorb light and cast a shadow on it. The intensity pattern obtained from this image I_a is compared with the reference intensity pattern I_p , to infer the column density information according to Eq. (4.2). Therefore, conventional absorption imaging involves acquiring two images¹, \mathcal{A} and \mathcal{P} for estimating I_a and I_p , respectively.

Ideally, these two images should be identical except for the shadow formed by the atoms. However, in practice, no two shots are the same. This happens due to many

¹A third image is acquired to estimate the background noise, which is then subtracted from the two primary images.

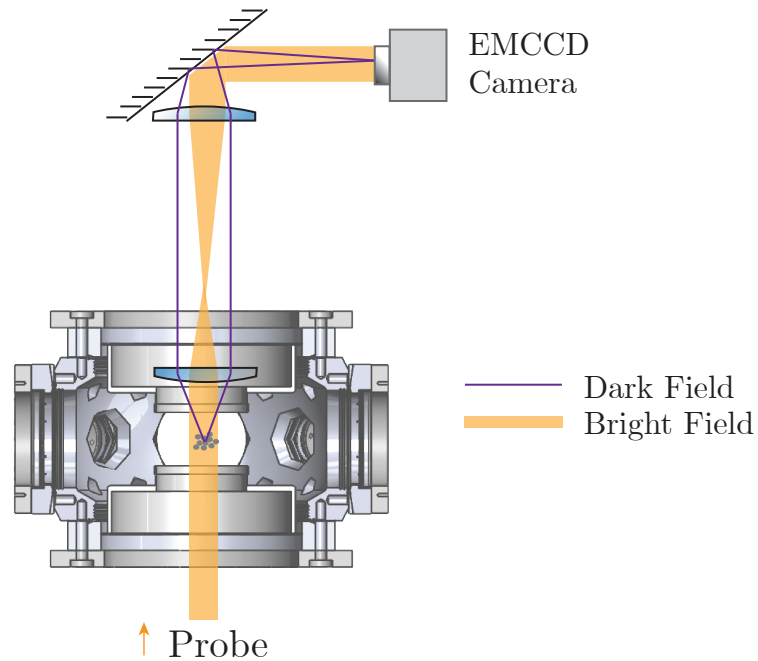


Figure 4.12: (a) Schematic of absorption imaging optical setup. The dark field created by the atoms cast a shadow on the probe.

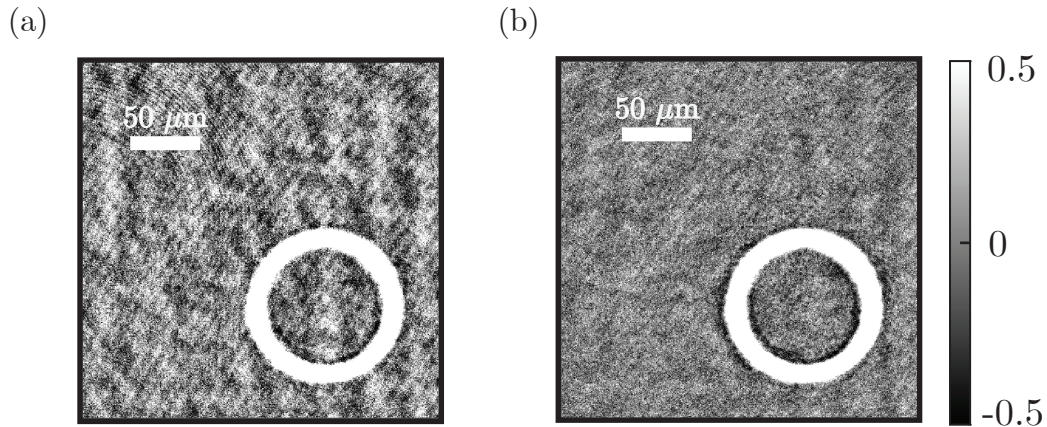


Figure 4.13: Optical densities obtained via absorption imaging without (a) and with (b) PCA. The gray bar indicates optical densities for both (a) and (b).

reasons, including mechanical vibrations. As a result, due to an inaccurate estimation of the reference intensity I_p , traditional absorption imaging results in optical densities with a noisy background, as shown in Fig. 4.13 (a). To get a more accurate estimate

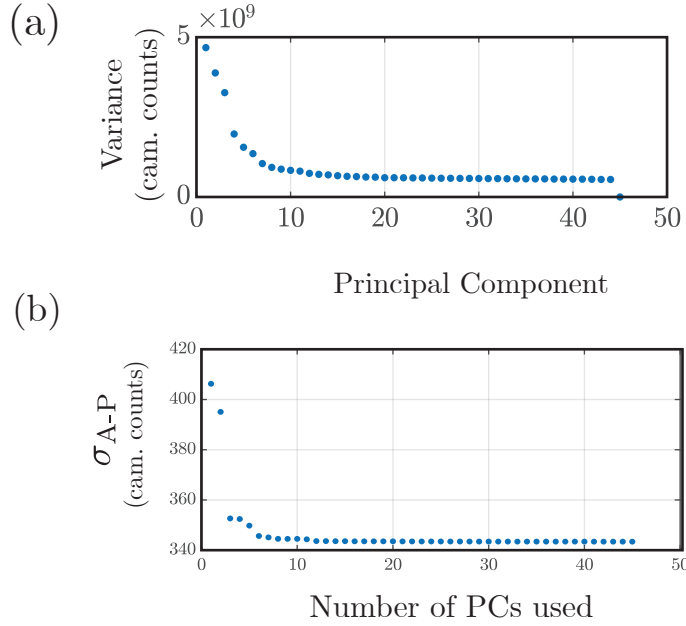


Figure 4.14: Principal Component Analysis. (a) The variance along each of the principal components. (b) σ_{A-P} as a function of the number of principal components used for reconstructing the reference image \mathcal{P} .

of I_p , we reconstruct the reference image \mathcal{P} from \mathcal{A} by projecting it onto an eigenbasis generated by many previously acquired reference images. This basis spans all possible reference images. We use the orthogonalization technique Principal Component Analysis (PCA) to convert the set of reference images into an eigenbasis. PCA has the advantage of sorting eigenvectors in order of decreasing variances such that most of the shot-to-shot variation is captured by the first few principal components, as shown in Fig. 4.14 (a). This reduces the dimensionality of the image reconstruction process. For Fig. 4.13, we have used 45 reference images to generate an eigenbasis. The optical densities obtained via PCA are less noisy, as shown in Fig. 4.13 (b). For the difference image $\mathcal{A} - \mathcal{P}$, we evaluate the standard deviation across all pixels, as more and more principal components are included in the reconstruction. This is plotted as σ_{A-P} in Fig. 4.14 (b). As evident

from this plot, the standard deviation saturates by the time seven principal components are included, thus demonstrating the dimensionality reducing of the reconstruction process. The higher-order principal components are just one-pixel wide, representing photon shot noise.

Chapter 5: Production of BEC

In the previous chapter, I gave a detailed layout of our apparatus and a brief overview of typical experimental techniques used. This chapter describes the procedure employed to cool Sodium atoms to Bose-Condensation and further shape the BEC into arbitrary 2D patterns. Like most alkali atoms, Sodium is typically cooled by laser cooling and forced evaporation techniques. Our experiment employs laser cooling followed by forced evaporation in magnetic and hybrid magnetic and optical traps. Our new apparatus uses a 2D MOT as a high-flux source of cold sodium atoms, as opposed to the previous version of this apparatus [4, 38, 39], which used a Zeeman slower. First, I describe our 2D MOT pre-cooling procedure, followed by the various laser cooling steps in the science chamber. Then, I detail our forced evaporation scheme, which combines cooling in magnetic and optical trap to exploit the best of both traps. Finally, I end by describing the steps involved in efficiently transferring the BEC into a purely optical trap. For each of these procedures, wherever possible, I provide a time trace of experimental parameters that are critical to that step.

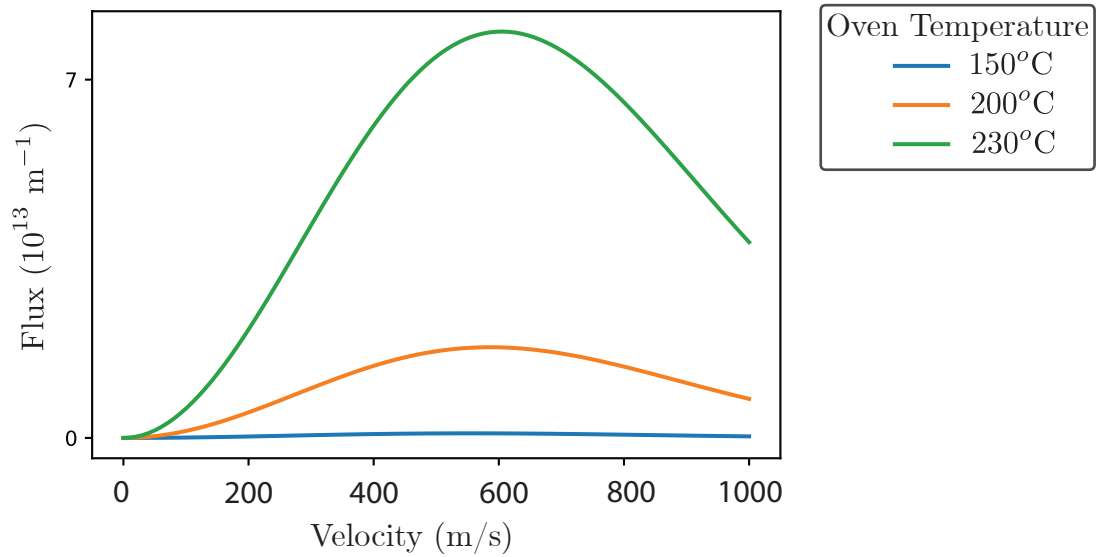


Figure 5.1: Flux vs. sodium atomic velocity at different temperatures. The blue, orange and green curves correspond to 150°C, 200°C, and 230°C, respectively. As a point of reference, 3D MOT velocities are usually less than 100 m/s.

5.1 2D MOT Source

To start the cooling process, a source capable of producing a high flux of cold sodium atoms is needed. Since these atoms are eventually captured in a 3D MOT, the 3D MOT capture velocity (typically less than 100 m/s) sets an upper limit on the temperature of the captured atoms. To create sodium vapor, solid sodium metal is resistively heated. The oven temperature determines the flux and velocity distribution of atoms in this vapor. Fig. 5.1 depicts the flux of gaseous Sodium atoms at three different oven temperatures. Here, the velocity distribution is determined using the Maxwell Boltzmann function, and the temperature-dependent vapor pressure of sodium [2], which gives the overall flux. Fig. 5.1 shows that only a tiny fraction of the atoms effusing out of the oven are within the 3D MOT capture velocity. As a result, faster atoms need to be cooled before being

loaded into the 3D MOT.

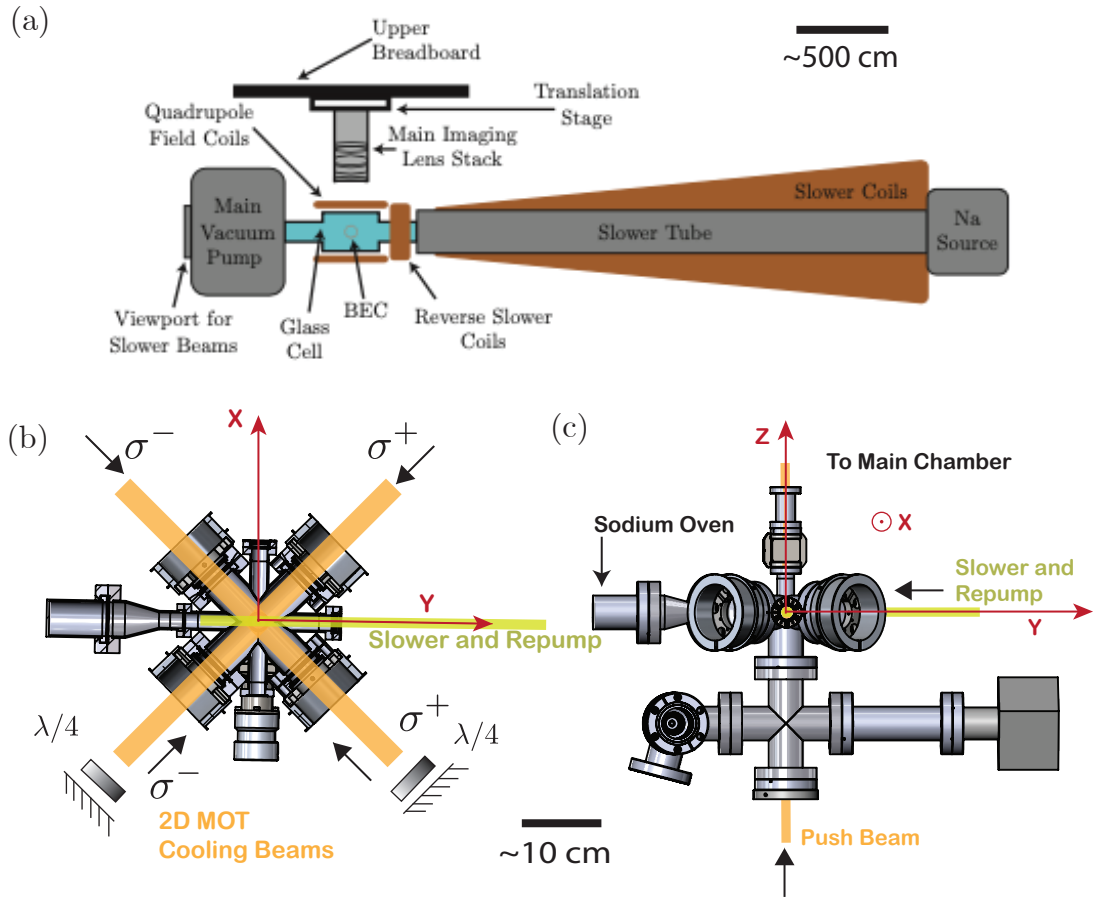


Figure 5.2: (a) Schematic of the old NIST experiment [4]. The main chamber is separated from the sodium source by a long Zeeman slower tube wound by magnetic field coils creating a space-varying magnetic field. (b) and (c) are two orthographic views of the 2D MOT chamber. The cooling arms cool atoms in the $\mathbf{e}_x - \mathbf{e}_y$ plane, as shown in (b). The push beam pushes atoms into the main chamber along the \mathbf{e}_z direction, as shown in (c). Sodium atoms effuse out of the oven in the positive \mathbf{e}_y direction. The slower beam is propagated along negative \mathbf{e}_y . The black bars at the top right and bottom center are scale bars for (a) and (b)/(c), respectively.

To this end, the previous version of this experiment used a Zeeman Slower [4, 38]. Zeeman Slowers slow faster atoms into a much slower range of velocities by Doppler cooling along a spatially varying magnetic field [28]. However, they have two significant disadvantages. First, they are complex and bulky as they have carefully engineered

electromagnets that span about a meter. Fig. 5.2 (a) shows the Zeeman slower apparatus used in the NIST lab. Second, the electromagnets require large currents with millisecond turn-off times, limiting control and detection sensitivities for magnetic field-sensitive experiments. Since we plan on making a dual-species BEC with Erbium which has a relatively high magnetic moment ($7\mu_0$), a Zeeman Slower is not ideal. Therefore, in the current version, we have replaced the Zeeman Slower with a 2D MOT [69–71]. Fig. 5.2 (b) and (c) shows a schematic of our 2D MOT setup. The working principle of a 2D MOT is the same as a 3D MOT, with the difference that it cools and traps only along two dimensions, as shown in Fig. 5.2 (b). Along the third dimension, a blue detuned laser beam pushes the pre-cooled atoms into the 3D MOT, as shown in Fig. 5.2 (c). We based our 2D MOT on the design in [71]. Permanent magnets generate a quadrupole magnetic field with a 36 G/cm linear field at the center of the 2D MOT. A unique feature of the design in [71] is the introduction of a Zeeman Slower beam which provides additional Doppler cooling for high-velocity atoms effusing out of the oven. We observe a five-fold increase in the 3D MOT atom number due to the introduction of this beam. This beam enters the chamber through a vacuum viewport exactly opposite to the oven, as shown in Fig. 5.2 (b) and (c). Thus, the window has a direct line of sight with the oven. At oven temperatures above 170 °C, it gets coated with a layer of shiny sodium metal. Therefore, we heat the window to a temperature of 150 °C by placing a 3” long and 1” wide Thorlabs lens tube in front of the window and heat it using resistive heating tapes. Due to space constraints, our sodium crucible is installed horizontally, thus increasing the risk of molten sodium migrating to other parts of the chamber. We installed an additional nozzle between the crucible and the rest of the 2D MOT chamber to avoid this migration.

5.2 Laser Cooling

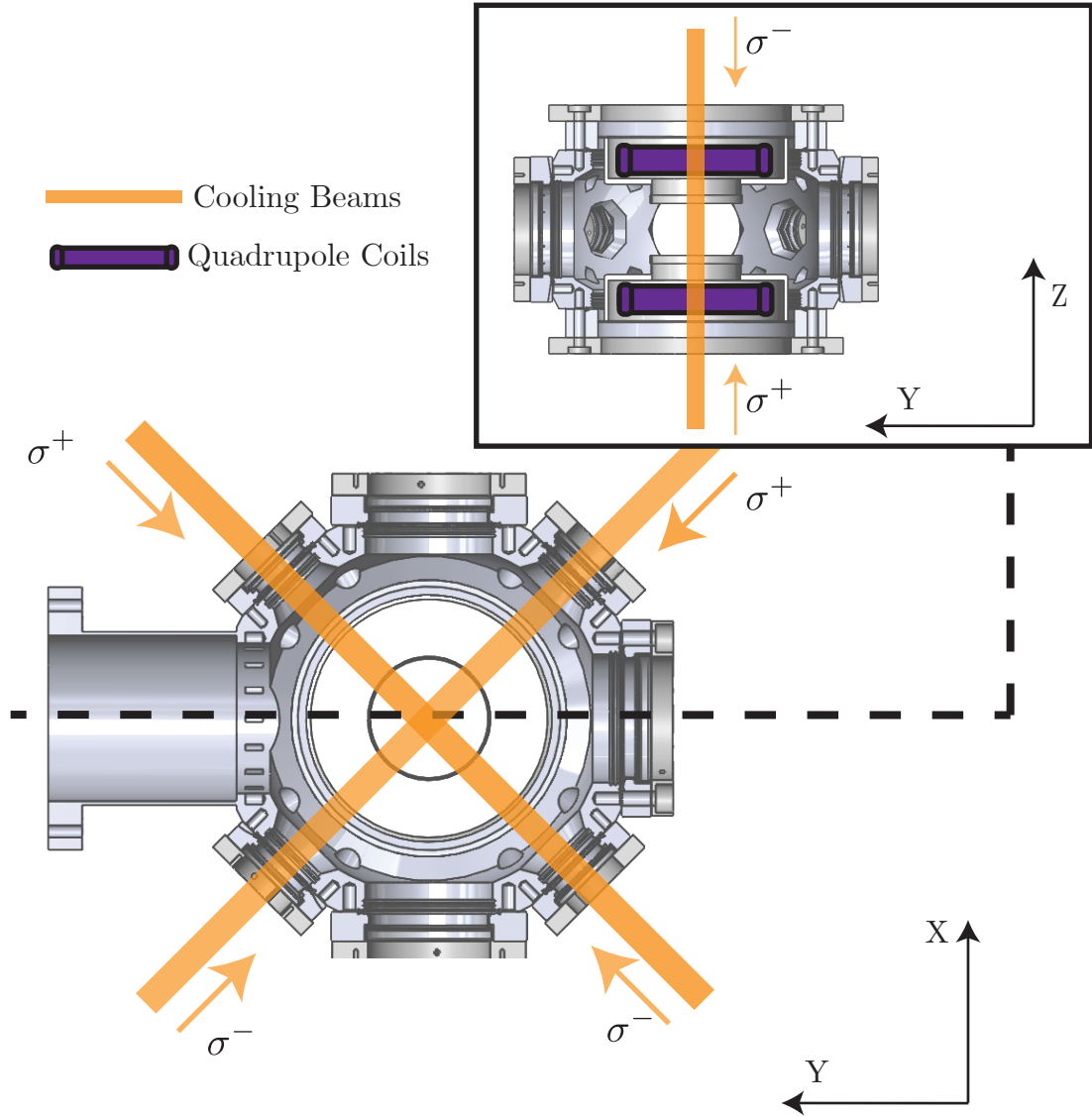


Figure 5.3: Cross-sectional views of the science chamber with the 3D MOT cooling beams depicted in yellow and quadrupole coils in purple.

Once the atoms are pre-cooled in the 2D MOT, a push beam transfers these atoms into the science chamber through the differential pumping tube. The push beam is 9 MHz blue-detuned from the cooling transition to address atoms with positive velocities relative

to the beam's wave vector. It is carefully aligned to the differential pumping tube to ensure that the atoms reach the center of the science chamber, where they are trapped in a 3D MOT. The push beam is not perfectly collimated but made to diverge slightly so that by the time it reaches the center of the chamber, its intensity drops enough to not push atoms out of the 3D MOT. The powers and detunings of the different 2D and 3D MOT beams can be found in Tab. 4.1.

Fig. 5.3 shows a schematic of our 3D MOT setup. Six circularly polarized laser beams intersect orthogonally at the center of the science chamber. These 3D MOT cooling beams are 16 MHz red detuned to the cooling transition and just 1.13 mW/cm^2 or $0.18 \times I_{\text{sat}}$ in intensity. These intensities are significantly lower than most ultracold atom experiments and can be attributed to an inefficient Polarization Gradient Cooling stage, limiting the 3D MOT capture velocity. This also results in a larger mismatch between the 3D and 2D MOT capture velocities, leading to much slow loading rate of the 3D MOT. Currently it takes around 10 s to load our 3D MOT to saturation, which is more than three times the $\approx 3 \text{ s}$ loading rate of the NIST experiment.

To generate the 3D MOT magnetic field, a pair of coils in the anti-Helmholtz configuration is used to produce a linear magnetic field gradient of 10.3 G/cm at the center of the science chamber. The magnetic field and the six laser beams form the 3D MOT providing a velocity and position-dependent force that cools and traps atoms close to the center of the chamber. In addition to the gradient coils, we have three pairs of Helmholtz coils along the three directions \mathbf{e}_x , \mathbf{e}_y and \mathbf{e}_z . These are capable producing constant bias magnetic fields at the center of the chamber. We use them to correct for the residual magnetic field or generate known magnetic fields whenever needed. We operate

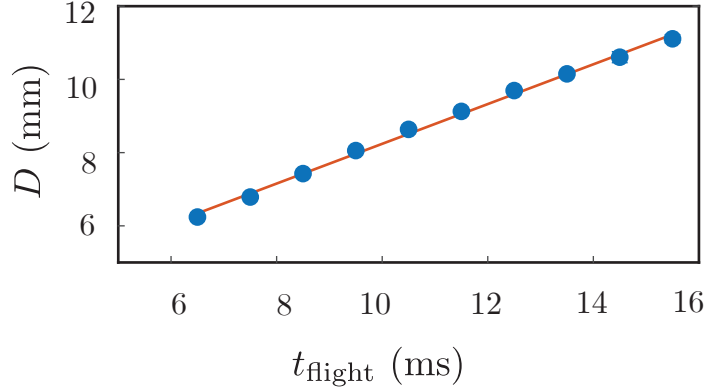


Figure 5.4: 3D MOT $1/e^2$ diameter D vs. time of flight t_{flight} . The red curve is a fit to the blue data points according to Eq. (5.1). The temperature of the thermal atomic cloud is estimated to be $T = 294(25) \mu\text{K}$ by measuring the rate of expansion, as described in the text.

the experiment with a “dark SPOT” MOT [72] which gives us atomic densities higher than a traditional MOT. We place a glass plate with a black dot in the repump’s path. The dark spot is imaged onto the center of the 3D MOT, creating a region with no repump. As a result, atoms in the dark region decay into the $F = 1$ state and fall out of the cycling cooling transition, thereby shielding them from the re-radiation forces that limit densities in traditional MOTs. In our experiment, we image a black dot of radius ≈ 5 mm onto the chamber’s center. The repump beam with the dark spot has 5 mW of power spread in a ring around the dark region. We trap 370×10^6 atoms cooled to a temperature of $294(25) \mu\text{K}$ in the 3D MOT. The temperature T is measured by releasing the atomic cloud in time of flight (TOF) and looking at its diameter D as a function of TOF, t_{flight} , as shown in Fig. 5.4. The sudden release of the atomic cloud converts all its energy $k_B T$ into kinetic energy $\frac{1}{8}m\frac{d}{dt}D$, where k_B is the Boltzmann constant, and m is the mass of a sodium atom.

As a result, fitting the data to the equation,

$$D = \sqrt{\frac{8k_B T}{m}} t + D_0, \quad (5.1)$$

gives us an estimate of the atomic temperature. Here, D_0 is the in-situ diameter of the atomic cloud.

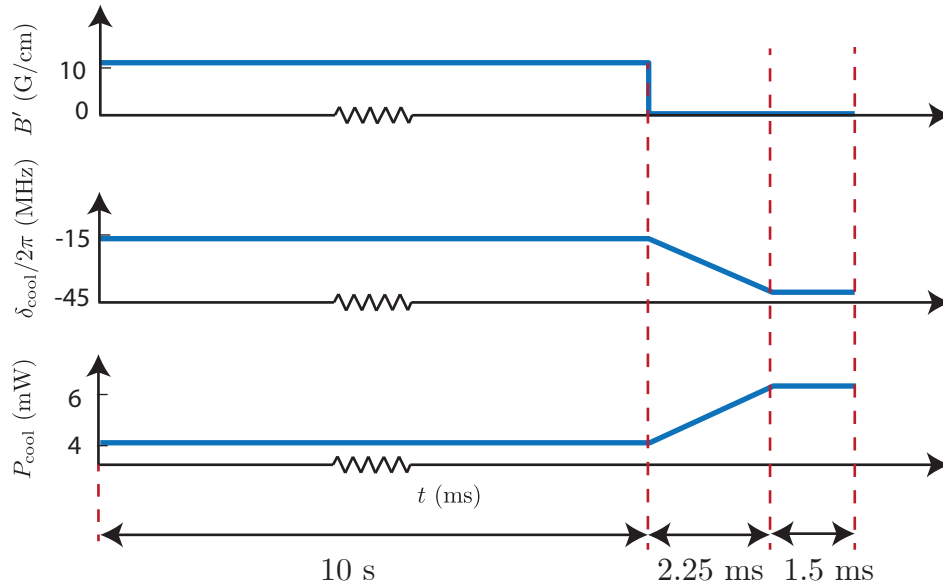


Figure 5.5: Critical laser cooling parameters vs. time t . Magnetic field gradient B' , cooling laser beam detuning δ_{cool} and power P_{cool} during 3D MOT and PGC stages. The vertical dashed red lines separate the laser cooling steps into three sections. The first 10 s long section is the 3D MOT loading. PGC is performed for the remaining 2.25 ms and 1.5 ms sections.

After cooling atoms in the 3D MOT, the magnetic field gradient is turned off, and the atoms are subjected to Polarization Gradient Cooling (PGC) [30,73]. The cooling light is detuned linearly from -16 MHz to -39 MHz in 2.25 ms and then held at -39 MHz for 1.5 ms. Even though PGC reduces the temperature of the atoms to $178 \mu\text{K}$, it is significantly higher than most Sodium BEC apparatuses [30]. Our current protocol to tune the cooling

light frequency is by varying an AOM's frequency, whose operational bandwidth limits the detunings we use for PGC. In the future, we plan to programmatically vary the laser lock point instead, allowing for a frequency sweep of more than 200 MHz, hopefully leading to a more efficient PGC. PGC marks the end of the laser cooling process. Fig. 5.5 summarizes the variation of different experimental parameters throughout the laser cooling process.

5.3 Forced Evaporation

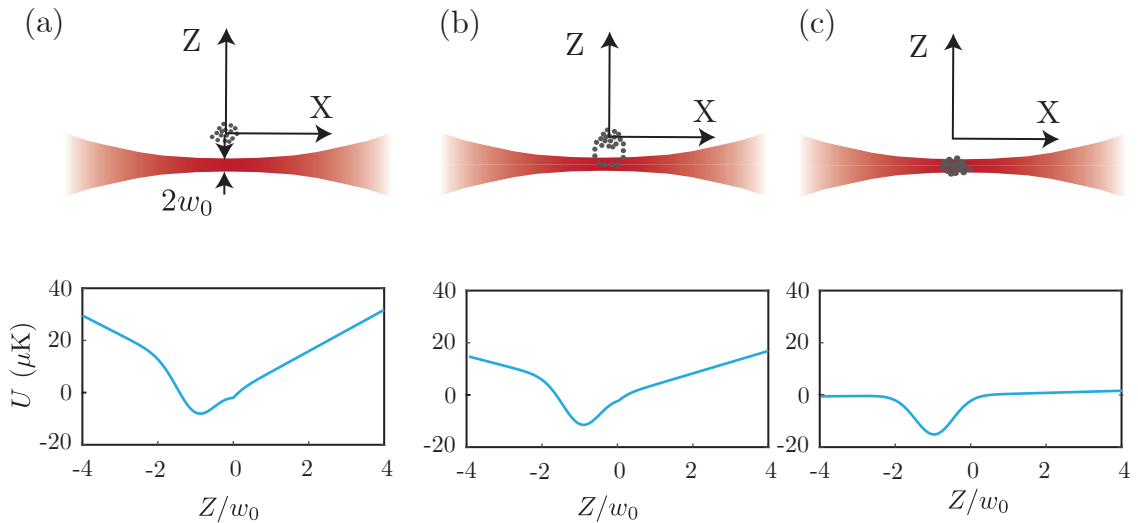


Figure 5.6: Schematic of the transfer of atoms from a quadrupole magnetic trap to a hybrid magnetic and optical trap. (a), (b), and (c) depict three snapshots during the transfer process as the magnetic field gradient is reduced from 228 G/cm (a) to 120 G/cm (b) and finally dropped to 7.3 G/cm (c). Gravity acts along the negative \mathbf{e}_z direction. The gravity compensation field gradient is 8 G/cm. The top row is a schematic of the single IR beam dipole trap. The origin marks the center of the magnetic trap. Atoms are adiabatically transferred into the hybrid trap as the field gradient is lowered. The bottom panel shows the change in potential energy landscape U along \mathbf{e}_z at $(x, y) = (0, 0)$, as the field gradient is reduced.

Unlike laser cooling, forced evaporation doesn't have a fundamental lower limit on

temperature, which makes it an ideal choice for attaining extremely cold atomic samples [6,32]. At a given temperature, there are always some atoms in the high energy tail of the Maxwell-Boltzmann distribution. Forced evaporation is a process where these energetic atoms are ejected out of the system, thereby reducing the average energy of the ensemble [74, 75]. The remaining atoms thermalize via inter-atomic collisions, resulting in net cooling. Since the technique relies on collisional thermalization, atomic densities need to be high enough such that thermalization times are shorter than the vacuum-limited sample lifetime or other inelastic collision processes. Typically forced evaporation is performed in a magnetic trap or an ODT. While magnetic traps are tunable to large volumes, ODTs can confine atoms to tiny dimensions, limited only by a laser beam's diffraction-limited spot size. As a result, magnetic traps are ideal for mode matching low-density and high-volume 3D MOTs, whereas ODTs help attain high densities for speedier evaporation. Ref. [76] uses a hybrid magnetic and optical trap to exploit the best of both techniques for Bose condensation of Rubidium atoms. In our experiment, we implement a similar scheme to achieve a Sodium BEC.

For the magnetic trap, we use a pair of current-carrying coils in the anti-Helmholtz configuration to generate a quadrupole trap. At the trap center, these coils produce a 1.30 G/cm linear field gradient for every ampere of current. A Lambda EMI 20-500 power supply powers the coils in constant voltage mode. This power supply is voltage limited at 20V. Since the coil circuit has a resistance of 103 m Ω , the power supply limits us to a maximum current of 190 A or a field gradient of 252 G/cm. In addition to the high field gradients, specific steps of the experiment require faster switching. The huge coils make the circuit highly inductive, resulting in long switching times from one state to

another. Therefore we connected a bank of nine IXYS IXFN230N20T power MOSFETs, in series to the coil, to quickly turn off the current. As a result, the turn-off time is limited only by the 200 ns response time of the MOSFETs. These MOSFETs are connected in parallel to each other to distribute the power dissipation equally, also water-cooled. A proportional integral (PI) servo controls the MOSFET gate voltage to open or close the circuit by monitoring the difference between the desired and the measured current through the coils. To measure the coil current, we use an Ultrastab LEM-IT-500-S hall probe sensor. For the ODT, we use a far red-detuned, 1064 nm single beam, focused to a spot size of $w_0 = 25 \mu\text{m}$, as described in Sec. 4.3.1. Fig. 5.6 (c) shows a schematic of the hybrid trap indicating the relative spacing between the IR beam and the center of the magnetic trap. While the IR beam provides confinement along its radial direction, a weak magnetic field gradient ensures confinement along the beam's longitudinal axis \mathbf{e}_x .

Our forced evaporation scheme starts with radio-frequency (RF) evaporation in the magnetic trap, followed by an adiabatic transfer into a hybrid magnetic and optical dipole trap, and finally ends with evaporation in the hybrid trap. Of the three magnetic sublevels of the $F = 1$ state, only the $m_F = -1$ is magnetically trappable. Therefore to capture most of the atoms into the magnetic trap, atoms are spin-polarized into the $|F = 1, m_F = -1\rangle$ ground state by first applying a DC magnetic field and then shining a σ^- polarized laser beam propagating along the magnetic field. The magnetic field defines a quantization axis and lifts the degeneracy between the various hyperfine magnetic sublevels. On application of the σ^- polarized light, atoms are transferred into the stretched state $|F = 1, m_F = -1\rangle$. This light is 26 MHz red detuned to the repump transition. After spin-polarization, we quickly turn on the magnetic field gradient to a relatively low value

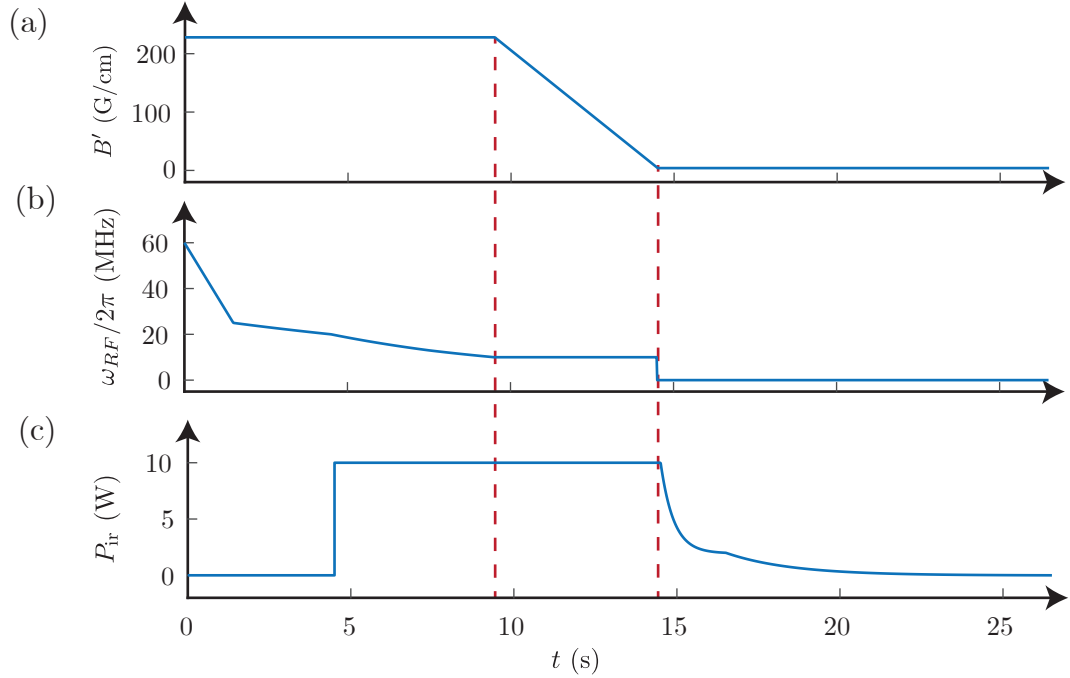


Figure 5.7: Critical forced evaporation parameters vs. time t . Magnetic field gradient B' (a), RF frequency ω_{RF} (b), and IR ODT power P_{ir} (c) during RF evaporation, adiabatic transfer and hybrid trap evaporation stages. The vertical dashed red lines indicate the separation of the three stages.

of 68 G/cm in 2 ms. The smaller field gradient results in a larger trap volume, enabling efficient atom transfer into the magnetic trap. We capture 250 M atoms of the 370 M laser-cooled atoms (67 %) into the magnetic trap. Once captured, we compress the trap by ramping the magnetic field gradient to 228 G/cm in 100 ms, resulting in higher densities and a shorter re-thermalization time. RF evaporation is then performed by addressing atoms in the high energy tail, providing enough energy to spin-flip to the magnetically untrappable $|F = 1, m_F = 1\rangle$ state. Fig. 5.7 plots the variation of critical parameters during the forced evaporation process. We start with addressing higher energy atoms with RF at 60 MHz and gradually sweep the frequency down to 10 MHz in 9.5 s, as shown in Fig. 5.7 (b). The initial sweep from 60 to 25 MHz is performed in a 1.5 s linear

ramp, followed by three exponential ramps for 25 to 20 MHz, 20 to 13 MHz, and 13 to 10 MHz in 3, 3, and 2 s, respectively. The RF radiation is generated using an Agilent 33250A function generator that goes through an RF amplifier and is then applied to the atoms using a loop antenna wound around a 2" lens tube placed near the bottom recessed window. Due to Majorana spin flips near the center of the quadrupole field [77–79], we see a significant loss of atoms if the RF frequency is swept below 10 MHz. Therefore we stop here and perform the rest of the evaporation in the hybrid trap.

During the last 5 s of RF evaporation, we turn on the IR beam to full power. Once the RF sweep is complete, we perform an adiabatic relaxation of the magnetic trap to transfer atoms into the hybrid trap in 5 s. The vertical red dashed lines in Fig. 5.7 indicate the start and end of the adiabatic expansion process where the field gradient is linearly ramped from 228 G/cm to 7.3 G/cm in 5 s. This adiabatic expansion results in cooling of the atomic ensemble, as shown in Fig. 5.6. As the field gradient is lowered, the more energetic atoms are initially held in the quadrupole trap's low-density tail away from the dense cloud of colder atoms. Once the gradient falls below the gravity compensation value of 8 G/cm, the hot atoms are ejected out of the trap resulting in a net cooling of the ensemble. Lowering the gradient below gravity compensation lets us perform forced evaporation by lowering the IR power since the magnetic trap will no longer trap the ejected hot atoms. We achieve quantum degeneracy by ramping the IR power from 10 W to 50 μ W in 12 s as shown in Fig. 5.7 (c). The IR power is dropped in two exponential ramps: the first being 10 W to 2 W in 2 s, followed by 2 W to 50 μ W in the remaining 10 s. Fig. 5.8 (e) and (i) shows an in-situ image of the atomic cloud at the end of IR evaporation. The resulting cloud is cigar-shaped and expands anisotropically when released from the

hybrid trap, confirming that the evaporation results in Bose condensation.

5.4 Transfer to Purely Optical Traps

Once the sodium atoms are Bose condensed, we shape the BEC into arbitrary 2D patterns using two blue detuned beams from a 532 nm IPG GLR-30 fiber laser. Sec. 4.3 describes the construction of these ODTs. Fig. 5.8 (a)-(d) plots the time variation of experimental parameters critical to the transfer process. The sheet trap is turned on at full power during the final 10 s of evaporation in the hybrid IR trap. This is followed by linearly ramping the IR power to zero in the next 100 ms while the magnetic field gradient is still maintained at 7.3 G/cm. I will refer to this sheet and weakly confining field gradient as the ‘hybrid sheet trap’. The region between the first two vertical dashed lines depict the transfer from the hybrid IR to the hybrid sheet trap. Fig. 5.8 (e)-(l) are in-situ ODs of the BEC at different stages of the transfer process. The hybrid sheet is significantly shallower than the hybrid IR trap at full power. As a result, turning the sheet beam on during IR evaporation doesn’t alter the BEC’s shape in the $\mathbf{e}_x - \mathbf{e}_y$ direction, as shown in Fig. 5.8 (i). However, it helps efficiently transfer atoms from the hybrid IR to the hybrid sheet trap. Fig. 5.8 (f) and (j) shows an in-situ image of the hybrid sheet trap, where the weak field gradient provides the planar $\mathbf{e}_x - \mathbf{e}_y$ confinement. The radial confinement of this disk can be altered by either changing the field gradient or the bias magnetic field in the \mathbf{e}_z direction. Since the field gradient is a crucial parameter affecting evaporation, we tune the \mathbf{e}_z magnetic field bias to alter the disk size.

Once in the hybrid sheet trap, we switch the DMD beam on and project a dark

circular disk with a radius similar to the BEC in the hybrid sheet trap. Fig. 5.8 (g) and (k) show the in-situ ODs of the BEC at the end of this step. The third (from left) vertical line also denotes this in Fig. 5.8 (a)-(d). We then linearly turn the field gradient to zero in 500 ms. The BEC is now trapped in a purely optical trap and has an OD as shown in Fig. 5.8 (h) and (l). Throughout the transfer of atoms across different magnetic and ODTs, we maintained a small non-zero magnetic field bias. As a result, the trapped atoms are maintained in the $|F = 1, m_F = -1\rangle$ state. Once we transfer atoms into this purely optical disk trap, we can project different patterns on the DMD and obtain arbitrary shaped quasi 2D BECs. Once the BEC is shaped in this purely optical trap, we are ready to perform experiments on it. For example, Chapter 6 describes one such experiment, where the shape of the BEC is altered dynamically during an experiment to simulate the expansion of universe.

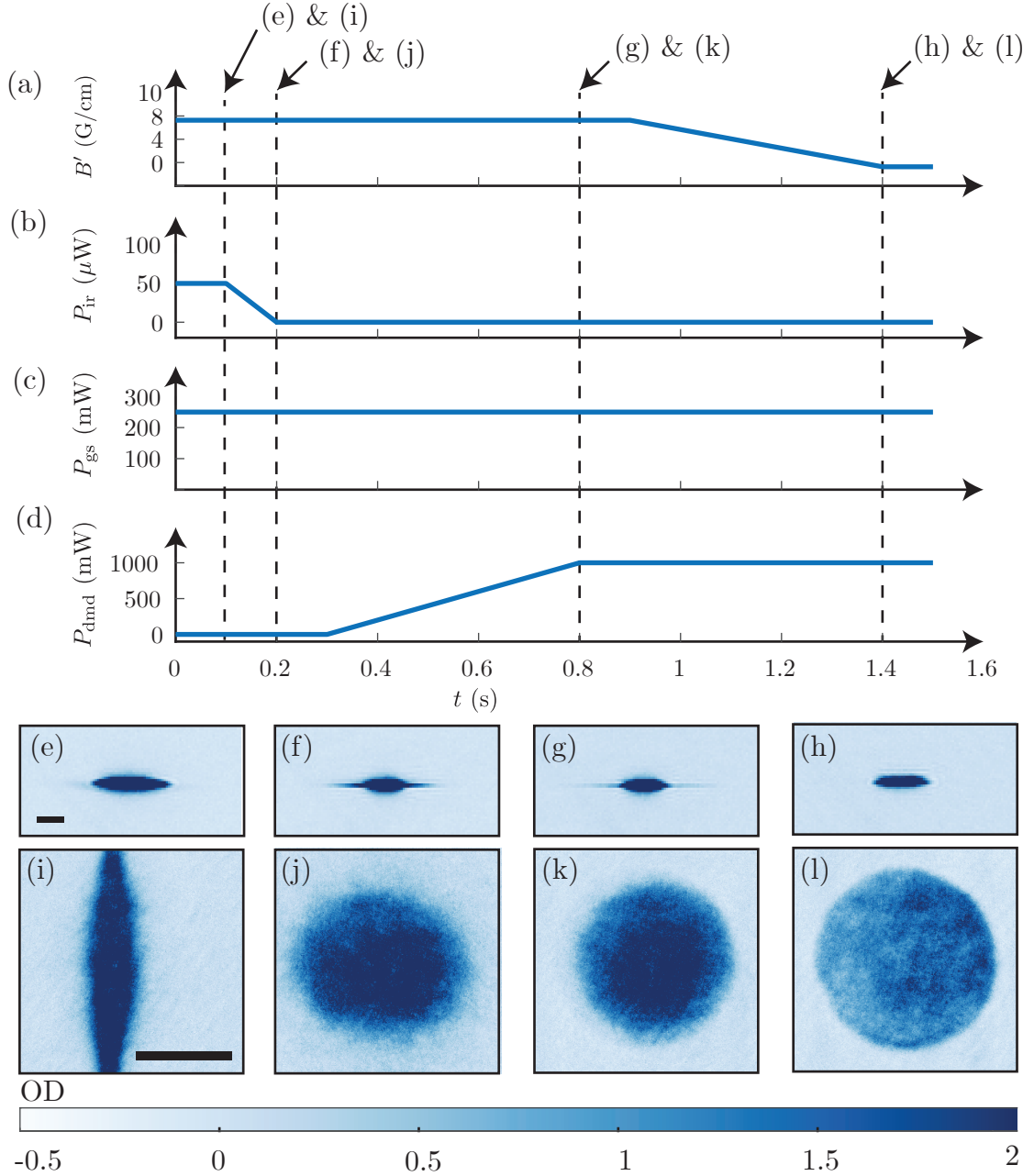


Figure 5.8: Transfer of BEC into purely optical traps. Critical parameters, magnetic field gradient B' (a), IR ODT power P_{ir} (b), sheet trap ODT power P_{gs} (c), and DMD ODT power P_{dmd} (d) vs. time t . The vertical dashed lines indicate the instant when the in-situ ODs (e)-(l) were imaged. (e)-(h) are ODs on a vertical plane, with the horizontal axis pointing along the IR beam (\mathbf{e}_x) and gravity acting along the vertical axis (\mathbf{e}_z). (i)-(l) are ODs on a horizontal plane, with the horizontal axis pointing along the sheet trap beam (\mathbf{e}_y) and the vertical axis pointing along the IR beam (\mathbf{e}_x). The black bars in (e) and (i) correspond to $50 \mu\text{m}$, the length scales being the same for all horizontal and vertical images separately. The color bar at the bottom depicts the OD scale for (e)-(l).

Chapter 6: The Hubble Friction Experiment

The massive scale of the universe makes the experimental study of cosmological phenomena difficult. Moreover, since performing controlled experiments is mostly impossible, experimental verification of cosmological hypotheses relies on few naturally occurring test cases. This has resulted in the emergence of the field of Analogue Gravity which deals with developing analogous table-top experiments to simulate cosmological systems. Unruh established one such analogy in 1981, where he demonstrated the similarity between sound waves in a moving fluid and fields at a black hole event horizon, thereby hinting at the possibility of simulating Hawking radiation in a moving fluid [51]. Since then, analogous systems have been realized in various physical platforms ranging from classical fluids to cold atomic systems. In this chapter, I will describe our approach towards creating an analogous system for studying the inflationary dynamics of the early universe.

Our table-top setup comprises a toroidally shaped BEC of ^{23}Na atoms, which we use to simulate the universe's expansion and contraction. The toroidal BEC is shaped using the sheet and DMD traps, as described in Sec. 4.3, and serves as our analogous universe. Since the DMD has a maximum frame update of 32 kHz, we can dynamically vary the radius of this toroid during the experiment, hence simulating expansions and contractions of our BEC universe. Finally, we wish to study the evolution of scalar fields

in the early universe. Analogous to fluctuating scalar fields, our quasi-2D BEC system can have azimuthally traveling collective modes or phonons. In a typical experimental sequence, we imprint phonons by creating density perturbations on the toroidal BEC by halftoning binary patterns on the DMD, as described in Sec. 4.3. Because of the aspect ratio of the toroid, the energy needed to excite non-azimuthal phonon modes is much higher, thereby limiting our system to primarily have azimuthal phonons.

Exploiting the above analogy, in a previous work [41], our group simulated elements of an expanding universe, including the redshifting of phonons in analogy to the redshifting of photons. In a recent work [80], we have simulated and studied the cosmological phenomenon of Hubble friction in detail. Hubble friction is the phenomenon responsible for exponential decay of scalar fields in an expanding universe. This chapter starts with a pre-print version of our recent work [80] in Sec. 6.1, followed by some supplemental material that was instrumental in designing and understanding the experiment. All authors significantly contributed towards the publication. The experimental setup was designed and constructed by me, Monica Gutierrez Galan, Madison Anderson, and Hector Sosa Martinez. The data acquisition was done by me, Monica, and Hector. I performed the data analysis.

6.1 Publication: Hubble Attenuation and Amplification in Expanding and Contracting Cold-Atom Universes

6.1.1 Abstract

In the expanding universe, relativistic scalar fields are thought to be attenuated by “Hubble friction”, which results from the dilation of the underlying spacetime metric. By contrast, in a contracting universe this pseudo-friction would lead to amplification. Here, we experimentally measure both Hubble attenuation and amplification in expanding and contracting toroidally-shaped Bose-Einstein condensates, in which phonons are analogous to cosmological scalar fields. We find that the observed attenuation or amplification depends on the temporal phase of the phonon field, which is only possible for non-adiabatic dynamics, in contrast to the expanding universe in its current epoch, which is adiabatic. The measured strength of the Hubble friction disagrees with recent theory [J. M. Gomez Llorente and J. Plata, *Phys. Rev. A* **100** 043613 (2019) and S. Eckel and T. Jacobson, *SciPost Phys.* **10** 64 (2021)], suggesting that our model does not yet capture all relevant physics. While our current work focuses on coherent-state phonons, it can be extended to regimes where quantum fluctuations in causally disconnected regions of space become important, leading to spontaneous pair-production.

6.1.2 Introduction

During the early universe’s rapid expansion, primordially fluctuating scalar fields are thought to have been exponentially redshifted and attenuated by the expanding spacetime

metric, where “Hubble friction” contributes to the latter [81]. Unlike true friction, Hubble friction is non-dissipative and therefore, while it attenuates scalar fields in an expanding universe, it would amplify them in a contracting universe. In previous work [41], our group showed that an atomic Bose-Einstein condensate (BEC) in an expanding toroidal trap could simulate elements of an expanding universe, including the redshifting of phonons in analogy to the redshifting of photons. Here, we build upon these studies by: including contracting universes; measuring both Hubble attenuation and amplification with five-fold increased precision; and showing that the magnitude of Hubble friction disagrees with recent theoretical work [62, 82].

While the study of astrophysical systems is ordinarily limited to observations, the development of well-controlled laboratory systems has enabled tabletop realizations of general relativistic phenomena. Examples from a variety of physical platforms ranging from classical fluids to cold atomic systems include: the realization of acoustic black hole horizons [83–85]; stimulated and spontaneous Hawking radiation [24, 86, 87]; and scattering processes around rotating black holes [88]. With their unprecedented control and measurement capabilities, ultracold atoms are an emerging platform for realizing minimal models relevant to high energy physics [89], astrophysics [23, 51, 90, 91], and cosmology [21, 41, 54, 92].

In BECs, phonons are scalar fields that evolve approximately according to an effective spacetime metric defined by the background BEC [21]. For toroidally-shaped BECs, expanding or contracting 1D universes can be simulated by dynamically changing the BEC’s radius and observing the evolution of azimuthal phonons. Unlike the expansion observed in the photon-dominated epoch of the universe, we explore non-adiabatic expansions

and contractions where the rate of the metric change exceeds the oscillation frequency.

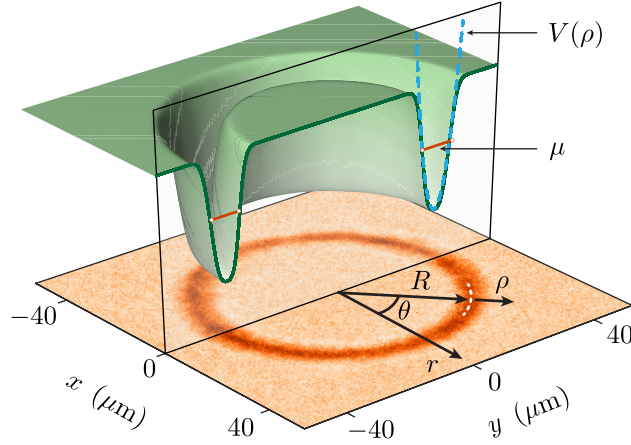


Figure 6.1: Ring-trapping potential and resulting atomic density. The green surface schematically depicts the trapping potential; the orange lines mark the typical chemical potential μ . The blue-dashed curve shows a power law fit to the potential (up to μ) around $\rho = 0$ giving exponent 2.02(3) for this example. The measured 2D density $n_{2D}(\rho, \theta)$ is shown in the $\mathbf{e}_x - \mathbf{e}_y$ plane (with peak density $165 \mu\text{m}^{-2}$) and the white dashed arc marks the mean radius R . Because of the short $500 \mu\text{s}$ TOF, the observed width of the ring is slightly in excess of that anticipated from the in-situ T-F approximation.

Phonons are predominately phase excitations with respect to the BEC's order parameter.

For a toroidal BEC with radius $R(t)$ (see Fig. 6.1), azimuthal phonons with mode number m , have an approximate phase profile $\delta\phi_{1D}(\theta, t) \equiv \delta\phi(t) \sin(m\theta)$ independent of r and z and obey the wave equation [62]¹

$$\left\{ \partial_t^2 + \left[2\gamma + \frac{\dot{\mathcal{V}}(t)}{\mathcal{V}(t)} \right] \partial_t + \omega_m^2(t) \right\} \delta\phi(t) = 0 \quad (6.1)$$

at low energy (i.e., small m). Here, the instantaneous angular frequency is $\omega_m = mc_\theta(t)/R(t)$, for speed of sound $c_\theta(t)$. Because this manuscript focuses exclusively on the $m = 1$ mode, we omit the m subscript in what follows. The quantity in square brackets is reminiscent

¹Eq. (3.14) derived in Chapter 3

of damping because it multiplies the first derivative of time. It includes two terms: a phenomenological damping constant γ^2 and the non-dissipative ‘‘Hubble friction’’ $\dot{\mathcal{V}}/\mathcal{V}$ arising from the changing metric defined by the background condensate. We model the external potential (see Fig. 6.1) as quadratic in z and power law in $\rho = |r - R|$; in the Thomas-Fermi (T-F) and thin-ring approximations, these lead to the BEC’s 3D volume $\mathcal{V} \propto R^\alpha$ and speed of sound $c_\theta \propto R^{-\alpha/2}$, where the value of the constant α depends on the potential [62]. Rather than detecting $\delta\phi_{1D}$, we measure the associated density perturbation $\delta n_{1D}(\theta, t) = \delta n(t) \sin(m\theta)$. The relationship between $\delta\phi$ and δn is $\partial_t \delta\phi = -(g/\hbar)(\delta n/R^\alpha)$, in terms of the Gross–Pitaevskii equation [45] interaction constant g .

In our experiments, the potential $V(\rho)$ is nominally fixed during expansion or contraction, predicting $\dot{\mathcal{V}}/\mathcal{V} = \gamma_H \dot{R}/R$ with strength $\gamma_H = \alpha$. In expanding systems ($\dot{R} > 0$) the Hubble friction term attenuates phonons, while in contracting systems it amplifies them. In the non-adiabatic regime $\dot{R}/R\omega_m$, the timing of expansion or contraction relative to the phonon’s temporal phase becomes important for subsequent dynamics. We show this enhances or diminishes the impact of Hubble friction: because the Hubble friction term includes the product of \dot{R}/R and $\delta n(t) \propto \partial_t \delta\phi(t)$, tuning the timing of expansion or contraction relative to the oscillation changes the degree of amplification or attenuation.

²This phenomenological damping term can account for Landau and Beliaev damping mechanisms [93] as well as imperfections in the confining potential.

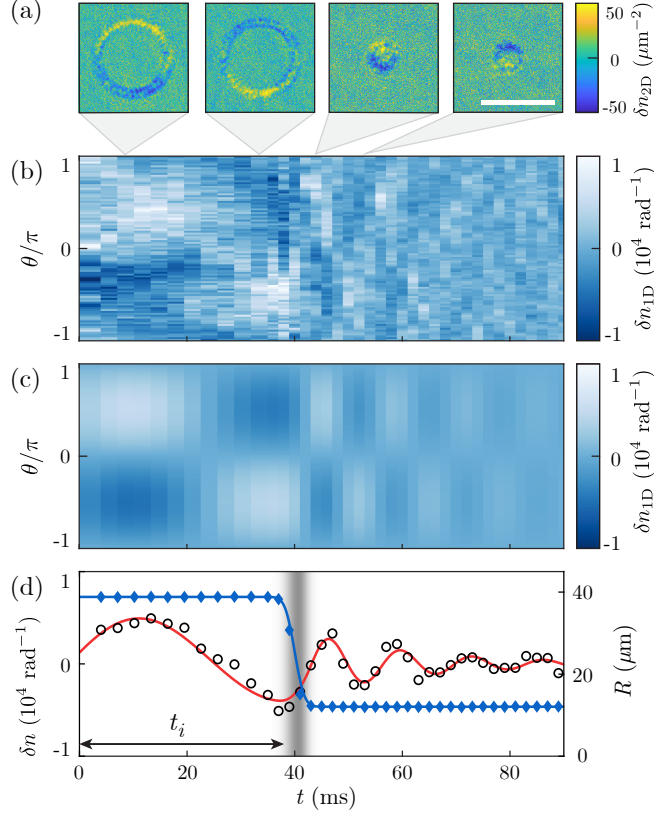


Figure 6.2: Phonon evolution in a contracting toroidally-shaped BEC, averaged over three measurements. (a) Density perturbations for a ring with $R_i = 38.4(6) \mu\text{m}$ at 10 ms and 35 ms, and $R_f = 11.9(2) \mu\text{m}$ at 45 ms and 53 ms. The density scale of images before contraction is multiplied by 2. The horizontal bar corresponds to $80 \mu\text{m}$. (b) Experimental measurements and (c) fit to Eq. (6.1) of angular density perturbation δn_{1D} as a function of azimuthal angle θ and time t , where the ring contraction occurs at t_i . (d) Phonon amplitude δn as a function of time. The circles plot the phonon amplitude obtained from fitting each time-slice of (b) to a sinusoid. The red curve is the instantaneous amplitude from the fit in (c). The diamonds are the measured mean radius of the BEC and the blue line is the programmed radius of the trap. The grayscale bar encodes the value of $|\dot{R}/R|$, with a maximum of $328(11) \text{ s}^{-1}$ at $t_{\text{peak}} = 41 \text{ ms}$. The arrow indicates $t_i = 38.2 \text{ ms}$.

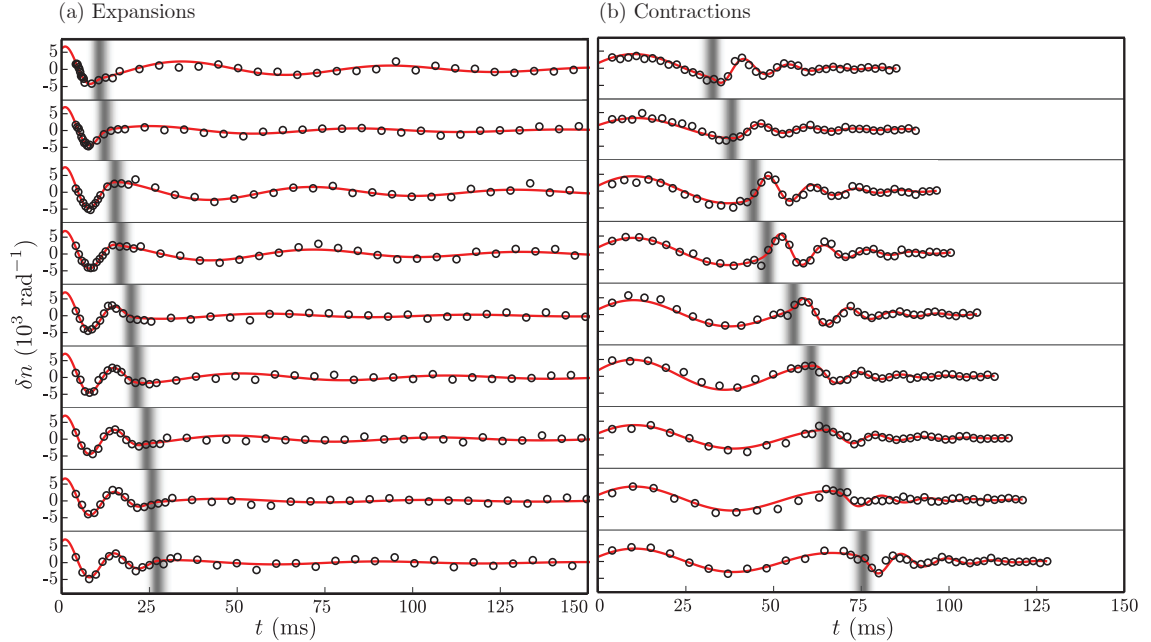


Figure 6.3: Phonon amplitude δn as a function of time t for (a) expanding and (b) contracting tori. The symbols, curves, and grayscale bars are all as notated in Fig. 6.2(d). The expansion data (a) used $R_i = 11.9(2) \mu\text{m}$ and $R_f = 38.4(6) \mu\text{m}$, and vice versa for contraction (b). t_i is varied from 6.5 ms to 23 ms for expansion and from 27 ms to 70 ms for contraction. Here, the red curves show simultaneous fits to our complete data set, as discussed in the text.

6.1.3 Experiment and Results

Our experiments [39, 76] begin with quasi-2D BECs with $N \approx 1 \times 10^5$ atoms confined in a pair of blue-detuned ($\lambda = 532$ nm) optical dipole traps. The chemical potential is $\mu \approx h \times 2.7$ kHz. The harmonic vertical confinement, with frequency $\omega_z/2\pi \approx 1.2$ kHz, is provided by a horizontally propagating Hermite-Gauss TEM_{01} beam. We generate nearly arbitrary space and time-dependent potentials in the r - θ plane by imaging $\lambda = 532$ nm laser light reflected by a digital micro-mirror device (DMD) onto the BEC. We use these potentials to create toroidal traps with radius R (see Fig. 6.1) ranging from $12 \mu\text{m}$ to $39 \mu\text{m}$ and radial width $\approx 5 \mu\text{m}$.

An azimuthal phonon excitation with mode number $m = 1$ is generated by perturbing the toroidal BEC with a potential $V_{\text{ph}} \sin(m\theta)$ ³. This repulsive potential—generated by the DMD—is applied for 2 ms, imprinting the phonon’s phase modulation onto the BEC. After imprinting, the phonon evolves for an initial time t_i from 6.5 ms to 70 ms, at which point the torus is expanded or contracted using an error function profile [41], with 10 %-90 % rise time 3.6 ms, and continues to evolve for up to ≈ 150 ms. For expansion, the initial and final radii are $R_i = 11.9(2) \mu\text{m}$ and $R_f = 38.4(6) \mu\text{m}$; these are reversed for contraction⁴. We detect the phonon at various points during the complete evolution using partial transfer absorption imaging (PTAI [68]) after a short 500 μs time of flight, giving the 2D density $n_{2\text{D}}(\rho, \theta)$ [see Fig. 6.1].

The phonon excitation’s density perturbation [see Fig. 6.2(a)] is $\delta n_{2\text{D}} = n_{2\text{D}} - n_{2\text{D}}^0$, where $n_{2\text{D}}^0$ is the density with no phonon present. Integrating along r gives the azimuthal density perturbation $\delta n_{1\text{D}}(\theta, t)$. Figure 6.2(b) shows the time evolution of $\delta n_{1\text{D}}$, and Fig. 6.2(c) shows the resulting fit to Eq. (6.1), from which we obtain both the red- or blueshift (via c_θ) and the Hubble friction (from γ_{H}). In our system, the phenomenological damping γ is observed to depend on radius, and we parameterize γ in terms of the quality factor $Q = \omega/2\gamma = c_\theta/2R\gamma$, which eliminates most of the radial dependence present in γ , (see [39, 47]).

Because the 3.6 ms expansion or contraction is a small fraction of the phonon oscillation period, the overall fit is insensitive to how Q interpolates between Q_i to Q_f . We therefore assume a simple linear dependence of Q on R . As shown in Fig. 6.2(b), our

³ V_{ph} is set to 0.8 times the overall potential depth.

⁴All uncertainties in this paper are the uncorrelated combination of 1- σ statistical and systematic uncertainties.

data typically has less than one oscillation before R changes; to reduce the uncertainty in Q_i and $\omega(R_i)$, we include fixed-radius rings in a simultaneous fit. These fits include as free parameters γ_H , Q_i , Q_f , α as well as the initial amplitude δn_i , temporal phase φ_0 , and speed of sound $c_{\theta,i}$. $c_{\theta}(t) = c_{\theta,i} (R(t)/R_i)^{-\alpha/2}$ follows the expected scaling.

Figure 6.2(d) summarizes the outcome of this fit. The red curve is the time-dependent density perturbation δn obtained from the full fit, while the circles plot δn from independent fits to $\delta n \sin(\theta)$ of each time-slice in Fig. 6.2(b). The blue curve displays the radius of the DMD pattern while the diamonds plot R obtained from a 2D T-F fit to the observed density distribution ⁵. The gray band plots \dot{R}/R during contraction, with maximum $\dot{R}/R \approx 1.53 \times \omega$.

We study the hypothesized impact of the phonon phase on the Hubble friction during expansion or contraction by changing t_i [see Fig. 6.2(d)], thereby phase-shifting the phonon by $(c_{\theta,i}/R_i)t_i$. We define t_{peak} as the time when the Hubble friction reaches its peak strength, i.e., when $|\dot{R}/R|$ is maximal. The phase of the phonon at t_{peak} is $\varphi_{\text{peak}} \equiv \int_0^{t_{\text{peak}}} dt \omega(t) + \varphi_0$. Figure 6.3 shows example time-traces with multiple t_i for both expansion and contraction, providing a complete picture to investigate the strength of Hubble friction. The black circles show the time evolution of the phonon amplitude $\delta n(t)$ for a range of t_i for both expansions (a) and contractions (b).

The red curves in Fig. 6.3 show the results of global fits of Eq. (6.1) to our complete dataset, which includes 17 contractions and 11 expansions. The parameters γ_H , α , Q_i , Q_f , $c_{\theta,i}$ and δn_i are global, i.e., they are shared across all time traces. For each time trace, δn_i

⁵By contrast with Ref. [41], the BEC follows the contraction profile without overshoot or oscillation because of tighter radial confinement.

is scaled by the atom number $N(t)$ for that trace, and $c_{\theta,i}$ is correspondingly scaled by $\propto N(t)^{\alpha/2}$ ⁶; this accounts for both atom loss during and after expansion or contraction and for overall drifts in atom number during data acquisition. Each global fit includes 7 additional time-traces, each with constant R , roughly from R_i to R_f . Because $c_{\theta}(R) \propto R^{\alpha/2}$ in stationary rings, these additional datasets further constrain α . We performed separate global fits for expansion and contraction data, giving an independent measure of their Hubble friction coefficients. Finally, we perform these global fits in eight different ways, with the number of fit parameters varying between 32 and 101. Each fit yields different best-fit values, but generally they agree within $2\text{-}\sigma$. These fitting methods differ on whether the temporal and azimuthal phases are shared across the time traces and if atom number varies within each time trace. Due to the large number of data points, the degrees of freedom, in excess of 1×10^4 , do not vary significantly between the different methods. We take the mean of the values obtained from the eight methods as the best fit value. Their standard deviation is added in quadrature to the average $1\text{-}\sigma$ uncertainty from the fit to obtain the final uncertainty in the measurement.

Table 6.1: Best fit global parameters.

	Q_i	Q_f	α	γ_H	$c_{\theta,i}$ (mm/s)	δn_i (rad ⁻¹)
Expansion	3.5(1)	4.4(2)	0.47(1)	0.28(4)	5.42(2)	7.47(13)
Contraction	7.8(3)	3.5(1)	0.52(3)	0.36(3)	4.36(4)	4.50(5)

Table 6.1 lists the best-fit values, with γ_H different for contraction and expansion. The values of α are in agreement with each other and are about $1/2$. For our power-law

⁶This can be derived from Eq.(4.8) and Eq.(4.20) of [62]

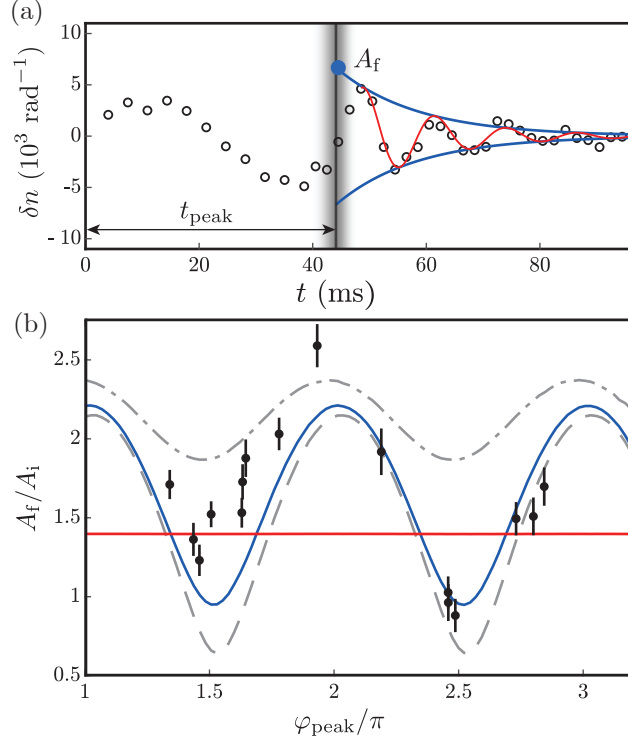


Figure 6.4: Phonon amplitude vs. phase. (a) Data (black circles), fit (red curve), and oscillation envelope (blue curve) used to extract the amplitude A_f at t_{peak} . The grayscale bar is as notated in Fig. 6.2(d). (b) Ratio of amplitudes A_f/A_i vs. φ_{peak} , the oscillation's phase at t_{peak} . The black circles plot the data. The gray dashed, blue solid, and gray dashed-dot curves show the prediction of Eq. (6.1) for $\gamma_H = 0, 0.36, \text{ and } 1$, respectively, with $\alpha = 0.52$. The red line indicates the prediction for an adiabatic contraction.

potential model [62], α ranges from $1/2$ (for a harmonic potential) to 1 (for a hard-wall potential). Our average value of $\alpha \approx 0.495$ suggests that we have a harmonic potential in both z and r .

Lastly, we confirm our expectation that the phonon phase φ_{peak} has a marked impact on the amplitude following expansion or contraction in the non-adiabatic limit. Our experiments probe $1.3 < \varphi_{\text{peak}}/\pi < 2.9$. Fig. 6.4(a) illustrates our process for obtaining the final amplitudes A_f where we fit the oscillatory behavior to an exponentially decaying sinusoid with the amplitude and temporal phase as free parameters (the remaining parameters

are drawn from the global fits). By contrast, the initial amplitude A_i is obtained from our global fit, from the envelope of the decaying sinusoid evaluated at t_{peak} . Figure 6.4(b) plots the fractional change in amplitude A_f/A_i versus φ_{peak} with black circles, and the solid blue curve depicts A_f obtained from our global fits ⁷. Our simulations (grey curves) show that the significant oscillations for $\gamma_H = 0$, give way to more uniform gain with increasing γ_H . The measured values of A_f/A_i are generally larger than would be expected for $\gamma_H = 0$, showing Hubble amplification due to contraction. Unlike Ref. [41], which probed $1.8 < \varphi_{\text{peak}}/\pi < 2.1$, where A_f/A_i has little dependence on Hubble friction, our greater range of φ_{peak} allows us to better constrain γ_H . In addition to the overall oscillation, there appears to be some additional dependence on ϕ_{peak} not captured by our model (data below $\phi_{\text{peak}}/\pi < 2$ generally lie above the $\gamma_H = 0.36$ curve, and above for $\phi_{\text{peak}}/\pi > 2$). This additional dependence may indicate a more complicated damping process for our phonons that could obscure our fitting for γ_H .

The observed oscillatory dependence of A_f on φ_{peak} results from the rapid non-adiabatic, i.e. superluminal, contraction in this experiment. The solid red curve emphasizes this point by plotting the simulated behavior for a slow adiabatic contraction, computed with $\gamma = 0$. No dependence on φ_{peak} is present in this limit, as the phonon would undergo many oscillations during expansion and therefore lose any dependence on initial phase. The deviation from the adiabatic curve is associated with “classical” stimulated emission or absorption into or out of the phonon field, in much the same way that these processes have been observed in acoustic black holes [23]. Direct observation of spontaneous

⁷The phenomenological damping term in Eq. (6.1) leads both A_i and A_f to decrease in a common-mode manner with increasing φ_{peak} , but that decrease is absent in the ratio A_f/A_i .

processes, i.e. pair production [25], would require an increase in our detection threshold. While here we averaged three images per time point, the observation of spontaneous Hawking radiation in Ref. [91] required a $\approx 10^4$ image dataset.

Our data generally agrees with the predictions of Refs. [62, 82], with the notable exception $\gamma_H \neq \alpha$. Because we create large-amplitude phonons to maximize our detection signal, it is possible that this leads to non-linear damping effects [48], compromising our measurement of γ_H , and potentially causing the additional dependence on ϕ_{peak} seen in Fig. 6.4(b). Likewise, the simple scaling of c_θ with R holds only in the thin-ring approximation, and our smallest rings have thickness to mean radius ratio of 0.45. For future experiments, our system is flexible enough to explore different metric scalings: to date we focused on quasi-one-dimensional universes, we could also potentially simulate two-dimensional (disc or square condensate) expansions or contractions where $\gamma_H > 1$, as suggested in Ref. [62]. Our experimental setup could also readily explore other analogue gravity systems such as black hole horizons in 2D systems, where, for example the acoustic metric resulting from quantized vortices could open new directions [94].

6.2 Model for the Toroidal Potential and Scaling Laws

The analysis in Sec. 6.1 assumes a power-law model for the trap potential. This section defines the trap potential V and derives relevant scaling laws essential for data analysis. The discussion here follows Ref. [62]. A cylindrically symmetric trap potential

$V(\rho, z)$ can be described by the power-law

$$V(\rho, z) := \mu [(\rho/\rho_\mu)^{n_\rho} + (z/z_\mu)^{n_z}], \quad (6.2)$$

where μ is the chemical potential of the BEC, n_ρ and n_z are the power-law exponents, and ρ_μ and z_μ are the T-F widths along \mathbf{e}_ρ and \mathbf{e}_z , respectively. Since the volume V is independent of the chemical potential μ , the T-F widths scale according to

$$\rho_\mu \propto \mu^{1/n_\rho} \quad \text{and} \quad z_\mu \propto \mu^{1/n_z} \quad (6.3)$$

The time evolution of a cylindrically symmetric BEC wavefunction $\psi(\rho, z, t)$ is given by the time dependent GP equation

$$-\frac{\hbar^2}{2m} \nabla^2 \psi + V\psi + g|\psi|^2 \psi = i\hbar \frac{\partial \psi}{\partial t}. \quad (6.4)$$

Under the T-F approximation, the spatial derivatives can be neglected. Assuming a stationary time dependence $i\hbar \partial_t \psi(\mathbf{r}, t) = \mu \psi$, Eq. (6.4) can be expressed as

$$\mu = g|\psi|^2 + V, \quad (6.5)$$

where $|\psi|^2$ is the atomic density. Integrating Eq. (6.5) over the entire BEC volume gives the expression

$$gN = \int d\rho dz (R + \rho) [\mu - V(\rho, z)], \quad (6.6)$$

where N is the total atom number. Solving the integral on the LHS of Eq. (6.6), it can be shown (see Ref. [62] for details) that

$$\mu \propto (R\rho_\mu z_\mu)^{-1}. \quad (6.7)$$

Using Eq. (6.7) and (6.2),

$$\mu \propto R^{-\alpha}, \quad (6.8)$$

where

$$\alpha = \frac{1}{1 + 1/n_\rho + 1/n_z}. \quad (6.9)$$

This further gives rise to two other scaling laws for the volume \mathcal{V} and azimuthal speed of sound c_θ

$$\mathcal{V} \propto R\rho_\mu z_\mu \propto R^\alpha \quad \text{and} \quad c_\theta^2 \propto R^{-\alpha} \quad (6.10)$$

These scaling laws were used for data analysis.

6.3 Simulation: Impact of Phonon Phase on Hubble Friction Strength

One of the goals of this project was the precise determination of Hubble friction strength. We performed multiple simulations of the differential Eq. (6.1) to estimate the impact that different experimentally controllable parameters would have on the strength of Hubble friction. To better understand how these parameters affect the Hubble friction,

I will rewrite Eq. (6.1) by making the substitutions $\dot{\mathcal{V}}/\mathcal{V} = \gamma_{\text{H}} \dot{R}/R$, and $\omega_{\text{m}} = mc_{\theta}/R$.

The resulting differential equation is

$$\left\{ \frac{\partial^2}{\partial t^2} + \left[2\gamma(t) + \gamma_{\text{H}} \frac{\dot{R}(t)}{R(t)} \right] \frac{\partial}{\partial t} + \frac{mc_{\theta}(t)}{R(t)} \right\} \delta\phi(t) = 0, \quad (6.11)$$

where the phase perturbations $\delta\phi$ are related to the density perturbations δn by

$$\frac{\partial \delta\phi}{\partial t} = -\frac{g}{\hbar} \frac{\delta n}{R^{\alpha}}. \quad (6.12)$$

As evident from Eq. (6.11), the Hubble friction strength depends on the value of $\gamma_{\text{H}} \dot{R}/R(t)$, and therefore its magnitude increases as the rate of change of radius \dot{R} increases. Our radial trap frequency is about 500 Hz which sets an upper limit on $|\dot{R}/R|$. Due to trap inhomogeneities, we cannot make a uniform ring larger than 40 μm in radius. Even though we can make rings with very small radii, doing so would violate the thin-ring approximation assumed in the derivation of Eq. (6.1) and (6.11). Therefore, we limit our ring radii between 12 and 44 μm and perform expansions and contractions with $|\dot{R}/R|$ less than 328 s^{-1} .

The other quantity that affects Hubble friction strength is the phase of δn when $|\dot{R}/R|$ achieves its maximum value (φ_{peak}). From Eq. (6.11) and (6.12), the third term can be shown to be proportional to $\dot{R}/R(t) \delta n$. Hubble friction results in maximum attenuation or amplification if the phase of δn is such that it attains its maximum value when $|\dot{R}/R(t)|$ is maximum. To investigate this hypothesized impact we solved the differential Eq. (6.11) for different phonon phases φ_{peak} . The remainder of this section

discusses simulations that were performed to understand the impact of the phonon phase φ_{peak} .

6.3.1 Simulation Model

To determine the time evolution of $\delta\phi$ or δn , in addition to Eq. (6.11) and (6.12), we need the time-evolution of R , c_θ , and γ . Both in the experiment and the simulations, radius R is varied according to

$$R(t) = \begin{cases} R_i, & \text{if } t < t_i \\ R_i + \frac{R_f - R_i}{2} \left[1 + \text{erf} \left(5 \left(\frac{t - t_i}{t_{\text{exp}}} - 0.5 \right) \right) \right], & \text{if } t_i < t < t_i + t_{\text{exp}} \\ R_f, & \text{if } t > t_i + t_{\text{exp}}, \end{cases} \quad (6.13)$$

where t_i denotes the start of ring dynamics and $t_{\text{exp}} = 10$ ms is the duration of ring dynamics. Since, $c_\theta \propto R^{-\alpha/2}$ (see Eq. (6.10)), we assume

$$c_\theta(t) = c_{\theta i} \left(\frac{R(t)}{R_i} \right)^{-\alpha/2}, \quad (6.14)$$

where $c_{\theta i}$ is the azimuthal speed of sound in the initial ring of radius R_i . As described in Sec. 6.1, γ is expressed in terms of the quality factor as

$$\gamma(t) = m c_\theta(t) / 2 R Q(t), \quad (6.15)$$

where we assume a linear dependence of Q on radius R given by

$$Q(t) = \frac{Q_i - Q_f}{R_i - R_f} R + \frac{Q_f R_i - Q_i R_f}{R_i - R_f}, \quad (6.16)$$

where Q_i and Q_f are quality factors in the initial and final rings. We use equations (6.13), (6.14), (6.15), and (6.16) along with the differential equation (6.11) and the density phase relationship (6.12) to determine the time evolution of δn .

6.3.2 Simulation Results

We solve the differential equation as described in the previous sub-section, to determine the impact of φ_{peak} on Hubble friction strength. Fig. 6.5 is one such simulation for contraction experiments. In Fig. 6.5 (a), we start with a ring with initial radius $R_i = 38 \mu\text{m}$ and then contract it to a final radius $R_f = 12 \mu\text{m}$ according to Eq. (6.13). The initial and final quality factors are assumed to be $Q_i = Q_f = 10$. The contraction starts at time t_i . The blue line indicates the ring radius as a function of time t . As the ring contracts, phonons evolve according to Eq. (6.11). We plot the amplitude of the phonon's density perturbation δn as the black curve in Fig. 6.5 (a). As is evident from the frequency of oscillations, phonons experience a blue-shift in frequency upon contraction. The time t_{peak} refers to the time when $\left| \dot{R}/R \right|$ attains its maximum value. The phase of the phonon at t_{peak} is given by $\varphi_{\text{peak}} \equiv \int_0^{t_{\text{peak}}} dt \omega(t) + \varphi_0$. We determine the amplitude of the decaying phonon envelope for both the initial and final phonons at the instant $t = t_{\text{peak}}$. These amplitudes are referred to as A_i and A_f respectively, as shown in Fig. 6.5 (a).

We study the hypothesized impact of the phonon phase φ_{peak} on the Hubble friction

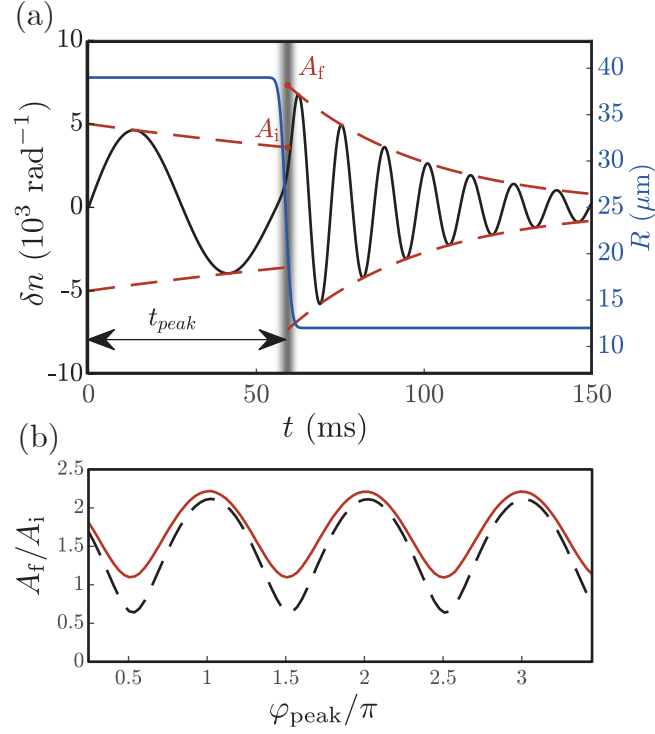


Figure 6.5: Simulations to study the impact of phonon phase φ_{peak} on Hubble friction strength. (a) Phonon amplitude (solid black curve), and oscillation envelope (dashed red curve) used to extract the amplitude A_i and A_f at t_{peak} . The blue curve denoted the radius R as a function of time t . The grayscale bar is as notated in Fig. 6.2 (d). t_{peak} is the time when $|\dot{R}/R|$ attains maximum value. (b) Ratio of amplitudes A_f/A_i vs. φ_{peak} , the oscillation's phase at t_{peak} . The solid red and dashed black curves correspond to a value of γ_H of 0.5 and 0, respectively.

by changing t_i [see Fig. 6.5 (a)], thereby phase-shifting the phonon by $(c_{\theta,i}/R_i)t_i$. Fig. 6.5 (b) summarizes this result where we plot the ratio A_f/A_i as a function of the phonon phase φ_{peak} . The dashed black and solid red lines are obtained by setting the value of γ_H to 0 and 0.5, respectively. As a result, the black line represents the situation in the absence of Hubble friction and contrasts it to the red curve which represents a non-zero Hubble friction. As evident from Fig. 6.5 (b), there is a significant difference between the black and red ratios A_f/A_i only for certain specific values of the phase φ_{peak} . At all other phases, the difference is small, indicating a strong dependence of the Hubble friction strength on

the phase φ_{peak} . This simulation served as our motivation for varying the phase φ_{peak} in the experiment.

6.4 Mode Purity of the Phonons

The experiments in this chapter are performed with $m = 1$ azimuthal phonons imprinted by halftoned binary patterns on a DMD. Though the patterns were selected to imprint only $m = 1$ phonons, due to imperfections in the projected optical perturbation, the excited phonons should be a linear combination of all possible phonon modes m . These experiments follow the trap loading procedure described in Sec. 5.4. The final ODT in Sec. 5.4 was a disk-shaped trap, as shown in Fig. 5.8 (h) and (l). Once the atoms are transferred into this purely optical trap, the disk DMD pattern is adiabatically changed to a ring of radius R_i . Atoms are then allowed to rest for 500 ms before the perturbation is applied.

To project azimuthal phonons, we impart a perturbing potential $V_{\text{ph}} \sin(\theta)$ using a DMD [39]. While smaller V_{ph} results in long-lived phonons with weaker density perturbations δn , large V_{ph} results in stronger density perturbations that decay quickly. For our experiments, we wish to detect δn with large signal-to-noise ratio over multiple oscillation periods. Therefore the value of V_{ph} was a trade-off between the long decay times and large signal-to-noise ratio. It was empirically determined to be 0.8 times the overall potential depth. Sec. 2.2.3 discusses typical damping mechanisms for BEC collective excitations. Since we mostly imprint the lowest order azimuthal modes, we expect Landau damping to be the primary mechanism for decay. Landau damping is a

finite temperature effect which thermalizes BEC phonons by scattering with other thermal phonons [46].

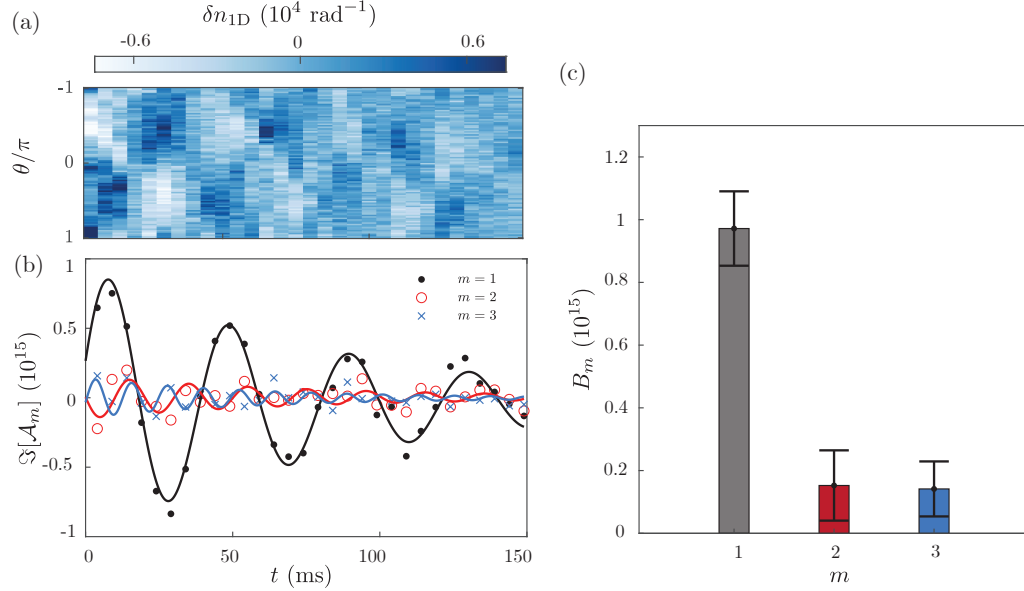


Figure 6.6: Relative contributions of different azimuthal modes in the imprinted phonon. (a) Raw data n_{1D} for phonons in a torus of radius $R = 31.8 \mu\text{m}$. (b) The black dots, red open circles and blue crosses show the time evolution of $\Im[\mathcal{A}_m]$ for modes with $m = 1, 2$, and 3 , respectively. The colored solid lines represent decaying sinusoidal fits according to Eq. (6.18). Each colored fit curve corresponds to the data points of the same color. (c) The amplitude B_m (see Eq. (6.18)) for the three modes evaluated from the fits in (b).

Since the DMD is a binary amplitude grating, we use Jarvis halftoning [66] to create smooth intensity gradients for imprinting phonons with mode number $m = 1$. Fig. 6.6 demonstrates the purity of the modes generated by this process. Fig. 6.6 (a) is the raw data corresponding to azimuthal density perturbation $\delta n_{1D}(\theta, t)$ as a function of time t and azimuthal angle θ for phonons in a torus with fixed radius $R = 31.8 \mu\text{m}$. To estimate the relative contribution of the different phonon modes, we evaluate the azimuthal spatial Fourier coefficient $\mathcal{A}_m(t)$ for the three lowest energy modes (m equal to 1, 2, and 3),

according to

$$\mathcal{A}_m(t) = \frac{\int \delta n_{1D}(\theta, t) \exp(i m \theta) d\theta}{\int \delta n_{1D}(\theta, t) d\theta}. \quad (6.17)$$

Fig. 6.6 (b) plots the time-evolution of the imaginary part of \mathcal{A}_m for the three modes. We fit $\Im[\mathcal{A}_m]$ with a decaying sinusoidal function

$$B_m \exp(-\omega_m t/2Q) \sin(\omega_m t + \vartheta), \quad (6.18)$$

where ϑ is the temporal phase at $t = 0$, Q is the quality factor, and B_m is the initial amplitude. The solid lines in Fig. 6.6(b) indicate these fits. Fig. 6.6(c) shows the initial amplitude B_m for the three modes. The error bars correspond to the 95% confidence interval in the fitted values of B_m . B_m of the desired $m = 1$ mode is 6.5(9) and 6.9(8) times larger than the $m = 2$ and $m = 3$ modes, respectively, indicating that while our oscillations are primarily $m = 1$, we may have a small admixture of other modes.

Expansion and contractions are performed by dynamically varying the ring radius in subsequent DMD frames. Leveraging the DMD's 32 kHz frame update rate, we smoothly transition from the initial to final radii in 90 frames, such that the ring radius changes by a distance corresponding to at most one DMD pixel in consecutive frames. To resolve small density variations, we detect the phonons at different evolution times using PTAI, where only 5-12% of the atoms are imaged. The transferred fraction is varied based on the overall density of the sample to maintain similar levels of signal-to-noise ratio. Even though we use the minimally destructive PTAI, only one image is acquired per repetition

of the experiment.

6.5 Fitting Method

In this section, we give a detailed description of our fitting methods. Our raw data comprises of azimuthal density perturbations $\delta n_{1D}(\theta, t)$ corresponding to expanding, contracting, and fixed-radii tori. As mentioned in Sec. 6.1.3, we perform the global fits in eight ways to mitigate potential systematic biases introduced by a fit parameter. Performing fits in eight different ways allowed us to investigate any potential systematic bias that 85 (i.e. $85 = 117 - 32$) of the 117 fit parameters might have caused. These methods enumerated in roman numerals I-VIII vary in the number of fit parameters ν_{fit} . Methods I and V assume the same temporal and azimuthal phases, methods II and VI assume same azimuthal but different temporal phases, methods III and VII assume same temporal but different azimuthal phases, and methods IV and VIII assume different azimuthal and temporal phases across the datasets. Methods I to IV assume a constant atom number throughout the ring dynamics. Since we observe an atom number loss of up to 20 % during ring dynamics, we analyze the data with fitting methods V to VIII, which fit the atom number $N(t)$ to an exponentially varying function of time and accordingly accounts for a change in $c_\theta(t) \propto N(t)^{\alpha/2}$. These differences in the fit methodology are reflected in the number of fit parameters ν_{fit} . Tab. 6.2 and Tab. 6.3 list the fit results obtained from each of the eight fitting methods for expansions and contractions, respectively. For both tables, the fit values corresponding to the eight methods agree within $2\text{-}\sigma$.

Table 6.2: Fit results of the eight different techniques when applied to the expansion data sets.

Mtd.	ν_{fit}	Q_i	Q_f	α	γ_H	$c_{\theta,i}$ (mm/s)	δn_i (rad ⁻¹)
I	32	3.5(1)	4.3(2)	0.48(1)	0.30(3)	5.44(1)	7.47(11)
II	43	3.5(1)	4.4(2)	0.47(1)	0.32(3)	5.44(1)	7.50(11)
III	43	3.5(1)	4.4(2)	0.47(1)	0.28(3)	5.42(1)	7.41(11)
IV	54	3.5(1)	4.5(2)	0.47(1)	0.29(3)	5.42(1)	7.41(11)
V	55	3.5(1)	4.3(2)	0.47(1)	0.26(3)	5.42(1)	7.52(11)
VI	66	3.5(1)	4.4(2)	0.46(1)	0.29(3)	5.41(1)	7.54(12)
VII	66	3.5(1)	4.5(2)	0.46(1)	0.24(3)	5.41(1)	7.44(11)
VIII	77	3.5(1)	4.5(2)	0.46(1)	0.27(3)	5.40(1)	7.45(11)

Table 6.3: Fit results of the eight different techniques when applied to the contraction data sets.

Mtd.	ν_{fit}	Q_i	Q_f	α	γ_H	$c_{\theta,i}$ (mm/s)	δn_i (rad ⁻¹)
I	32	7.7(2)	3.6(1)	0.51(1)	0.34(2)	4.38(1)	4.45(4)
II	49	7.6(2)	3.4(1)	0.49(1)	0.37(2)	4.40(1)	4.48(4)
III	49	7.7(2)	3.6(1)	0.51(1)	0.33(2)	4.38(1)	4.47(4)
IV	66	7.7(2)	3.5(1)	0.49(1)	0.37(2)	4.41(1)	4.49(4)
V	67	7.7(2)	3.6(1)	0.55(1)	0.37(2)	4.31(1)	4.53(4)
VI	84	7.9(2)	3.5(1)	0.53(1)	0.40(2)	4.33(1)	4.52(4)
VII	84	7.8(2)	3.7(1)	0.55(1)	0.35(2)	4.32(1)	4.55(4)
VIII	101	8.1(2)	3.5(1)	0.53(1)	0.39(2)	4.34(1)	4.54(4)

The large number of fit parameters result from including seven datasets corresponding to fixed-radius tori in the simultaneous fits. As mentioned in Sec. 6.1.3, dynamic datasets typically have less than one oscillation before the radius changes. Therefore we include the fixed-radius datasets to reduce the uncertainty in Q_i and $\omega(R_i)$. In addition to the global fit parameters listed in Tab. 6.1, the fit includes the amplitude, quality factor, azimuthal and temporal phases of the seven fixed-radius tori datasets as fit parameters. This sets the minimum value of fit parameters ν_{fit} to 32; 6 corresponding to the global

parameters listed in Tab. 6.1, 14 corresponding to the temporal and azimuthal phases of the seven stationary tori, and 12 corresponding to the amplitude and quality factor of six of the seven fixed-radius tori. The phonon in one of the seven fixed-radius tori is identical to the initial phonon of each dynamic dataset. Therefore its amplitude and quality factor are assumed to be the same as the global parameters δn_i and Q_f , respectively. Since the dynamic datasets typically have less than one oscillation before the radius changes, this allows us to constrain the value of δn_i and Q_f . Fig. 6.7 shows the phonon evolution in the stationary ring. The black circles denote the measured value of δn , and the red curve corresponds to the simultaneous fits. Given the variation in amplitude, quality factor, azimuthal and temporal phases across the seven fixed-radius datasets, these had to be included as independent fit parameters.

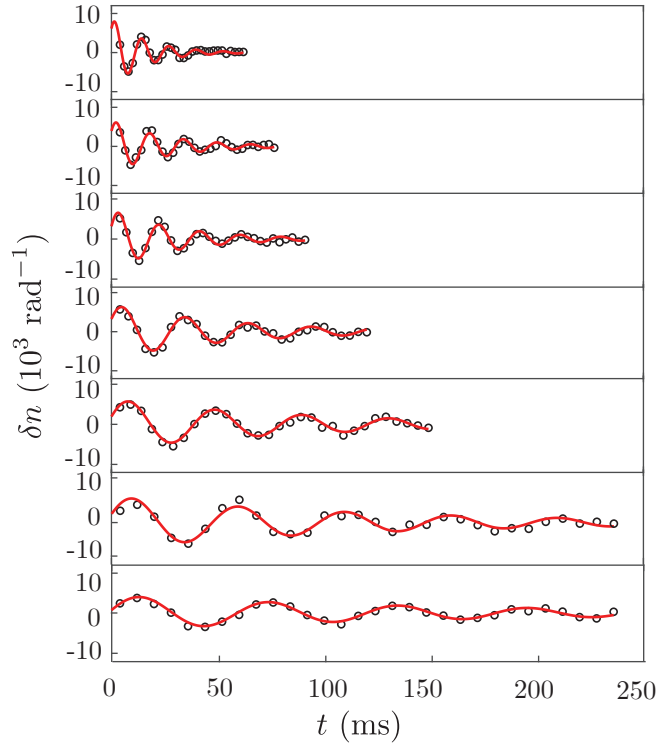


Figure 6.7: Phonon amplitude δn as a function of time t for stationary tori of radii 11.9, 14.3, 16.7, 24.0, 31.2, 38.4 and 43.2 μm from top to bottom. Here, the red curves show simultaneous fits to the complete data set, as discussed in Sec. 6.1.3.

Chapter 7: Towards Erbium BEC: Scanning Transfer Cavity Lock

One of the goals when designing and building the new apparatus was to make a dual-species degenerate gas mixture with Sodium and Erbium. Even though we haven't produced an Erbium BEC, significant progress has been made. For example, in 2017, we successfully demonstrated an Erbium 2D MOT in the same vacuum chamber as the sodium 2D MOT, thereby creating a single compact source of cold atoms for both species. In addition, my colleague Madison Anderson has constructed an inductive oven for producing a high flux of Erbium atoms. You can find more about that in her thesis, expected shortly.

Erbium is a rare-earth metal from the lanthanide series with atomic number 68. It has relatively high melting and boiling points of 1529° C and 2900° C, respectively. Atomic Erbium has six stable isotopes ^{162}Er , ^{164}Er , ^{166}Er , ^{167}Er , and ^{168}Er . ^{167}Er is a fermion while all others are bosons. Since the first experimental realizations of BECs [6, 7] and Fermi degenerate gases [95–97], the community of quantum gas researchers have laid significant emphasis on tuning inter-atomic interactions to build fully controllable quantum systems. Usually, for ultracold atoms, the interatomic interactions occur via

s-wave scattering, resulting in a mean-field contact potential U_{contact} , given by

$$U_{\text{contact}}(\mathbf{r}) = \frac{4\pi\hbar^2 a}{m} \equiv g \delta(\mathbf{r}), \quad (7.1)$$

where a is the s-wave scattering length, m is the mass of the atom, g is the GP interaction constant, and $\delta(\mathbf{r})$ is the kronecker delta function [98]. As evident from Eq. (7.1), U_{contact} is isotropic and short range. With the use of Feshbach resonances, the scattering length a can be tuned by orders of magnitude [35], thereby giving us a convenient handle on interactions. Since its first realization, Feshbach resonance have been used for many applications [10–13, 99]. In addition to the above interactions, elements with high dipole moment interact via a dipole-dipole potential given by

$$U_{\text{dd}}(\mathbf{r}) = \frac{C_{\text{dd}}}{4\pi} \frac{1 - 3 \cos^2 \theta}{r^3}, \quad (7.2)$$

where θ is the angle between the direction of polarization and the relative position of the particles \mathbf{r} , and C_{dd} is a constant proportional to the magnetic moment squared in the case of magnetic dipole dipole interactions [98]. As evident from Eq. (7.2), unlike U_{contact} , U_{dd} is anisotropic and long-range, making dipolar atoms like Erbium an exciting candidate for studying quantum phases, otherwise not possible with alkali atoms. Erbium has a relatively high permanent magnetic dipole moment of $7 \mu_B$, where μ_B is the Bohr magneton. In contrast, alkali metals such as Sodium have a dipole moment of about $1 \mu_B$. In addition to the high magnetic moment, bosonic Erbium has multiple Feshbach resonances densely packed into a small range of magnetic fields. Recent results from the

Ferliano group have revealed that ^{168}Er and ^{166}Er have 190 and 189 resonances over a 70 G range [100]. Compare this with ^{23}Na , which is known to have just three resonances at 853, 907, and 1195 G [101, 102].

In 2005, the experimental realization ^{52}Cr (dipole moment = $6 \mu_B$) BEC, opened up the field of ultracold mixtures of dipolar atoms [103]. This was soon followed by ^{164}Dy (dipole moment = $10 \mu_B$) [104] in 2011 and ^{168}Er [105] in 2012. Given its potential for studying strongly correlated many-body systems, we wish to add an Erbium BEC to our system and exploit these long-range and anisotropic interactions. The first step towards Bose condensing Erbium atoms is to laser cool them. For this, we need a laser that is frequency stabilized to the atomic transition of interest. The rest of this chapter will first give a quick overview of the Erbium atomic structure and then describe the design and implementation of a locking scheme to frequency-stabilize a 583 nm laser for laser cooling Erbium in a 3D MOT.

7.1 Laser Cooling of Erbium

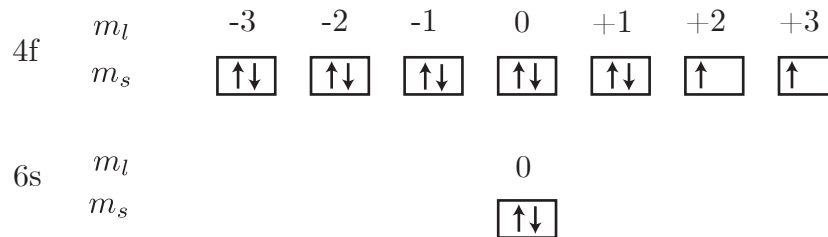


Figure 7.1: The Erbium ground state.

Early cold atom experiments focused on Bose-condensing alkali metals due to

their relatively simple energy level structure and high elastic to inelastic collision rate constants. The energy diagram for Erbium is much more complex and has multiple transitions that could be used for laser cooling [1]. The ground state of Erbium has the electronic configuration $[\text{Xe}] 4f^{12} 6s^2$, where $[\text{Xe}]$ represents the fully-filled atomic Xenon electronic configuration. Fig. 7.1 shows how the 4f and 6s shells of atomic Erbium are filled with electrons in the ground state. The two unpaired 4f electrons have angular momentum magnetic quantum number $m_l = +2, +3$, resulting in a large magnetic moment with orbital angular momentum quantum number $L = 5$. The total electronic spin $S = 1$ and the total angular momentum quantum number $J = 6$. As a result, the Erbium ground state can be expressed as ${}^3\text{H}_6$ in the term notation. In the case of heavier elements, the spin-orbit interaction is no longer small compared to interactions of spin and angular moments individually, thereby resulting in a breakdown of the L-S coupling scheme. All inner and outer electrons independently couple via the L-S coupling scheme, resulting in two total angular momentum quantum numbers J_1 and J_2 . The electrons in $[\text{Xe}]$ and the 4f shell qualify as inner electrons, while all others are considered outer. As a result, the atomic states are represented as coupling between these two J states via *jj* coupling scheme. Fig. 7.2 is the energy level diagram of Bosonic Erbium. Since Bosonic Erbium has zero nuclear spin, there is no hyperfine splitting.

Erbium has five possible laser cooling transitions [1], each with $J = 7$. Of these, we use the broad 27 MHz, 401 nm line for 2D MOT and the narrow 583 nm transition for 3D MOT. The excited state for the 2D and 3D MOT transitions are $[\text{Xe}] 4f ({}^3\text{H}_6) 6s 6p ({}^1\text{P}_1^o)$ and $[\text{Xe}] 4f ({}^3\text{H}_6) 6s 6p ({}^3\text{P}_1^o)$, respectively. The terms in parenthesis indicate the L-S coupling between the inner and the outer electrons, separately. The linewidth and other

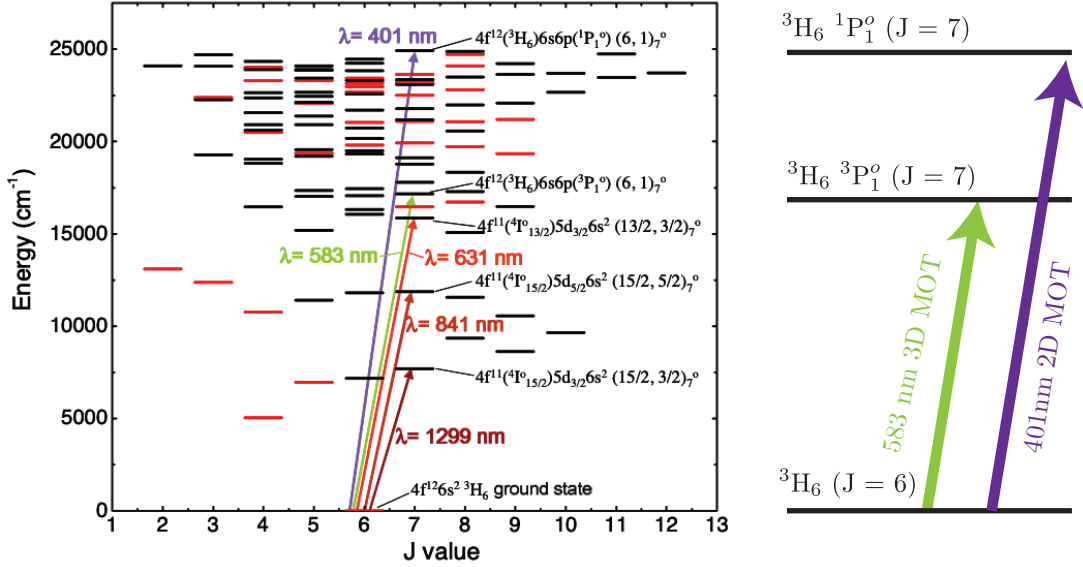


Figure 7.2: Laser cooling transitions in atomic Erbium [1]. The purple and green arrows indicate the cooling transitions used for the 2D MOT and 3D MOT, respectively.

parameters for these transitions are tabulated in Table 7.1. Below the 3D MOT excited state $[Xe] 4f (^3H_6) 6s 6p (^3P_1^o)$, Erbium has two metastable states. However, [1] estimates the transition rates to these states to be 0.017 s^{-1} and 0.0049 s^{-1} , which is much smaller than the fluorescence decay rate of the 3D MOT excited state to the ground state (10^6 s^{-1}). As a result, there is practically no leakage to dark states, and a re-pump is not needed. All we need is a laser locked at the 583 nm atomic transition with a line width and frequency stability better than 170 kHz. For the rest of the chapter, I will describe a simple and robust method to achieve such a lock by utilizing available frequency stabilized lasers in the lab.

Table 7.1: Erbium laser cooling transitions [1].

	λ (nm)	Γ (s^{-1})	$\Delta\nu$ (MHz)	I_{sat} (mW/cm^2)
2D MOT	400.91	1.7×10^8	27	56
3D MOT	582.84	1.0×10^6	0.17	0.11

7.2 Frequency Stabilization of 583 nm Laser

We use a 583 nm, frequency-doubled semiconductor laser (Toptica SHG DL-Pro) for the Erbium 3D MOT. The linewidth of this laser is supposed to be less than 2π 30 kHz when measured over a 1 s period. We verified it to be 2π 48(2) kHz by a delayed self heterodyne measurement with a 2 km long optical fiber and an 80 MHz AOM. Since the Erbium 3D MOT transition has a 2π 170 kHz natural linewidth, the short-term laser linewidth is good enough, and there is no need to narrow it further. However, over longer durations, the laser frequency drifts at an approximate rate of 33 kHz/s (measured on an Angstorm High Finesse WSU2 wavemeter), under typical laboratory conditions. This corresponds to a drift equal to the Erbium 3D MOT transition linewidth in about 5 s. Therefore, we need to frequency stabilize this laser with a locking scheme capable of responding faster than 5 s or a bandwidth greater than 200 mHz.

Typical laser frequency stabilization schemes such as Saturation Absorption Spectroscopy (SAS) lock the laser to the atomic transition by generating the corresponding signal in a heated vapor cell (for example, see Sec. 4.2). However, these methods rely on significant light absorption by the atomic gas. Erbium with a melting point of 1529°C has a very low vapor pressure at temperatures typically used for heating glass vapor cells. Fig. 7.3 contrasts Erbium vapor pressures with Sodium, for which SAS is used as a locking

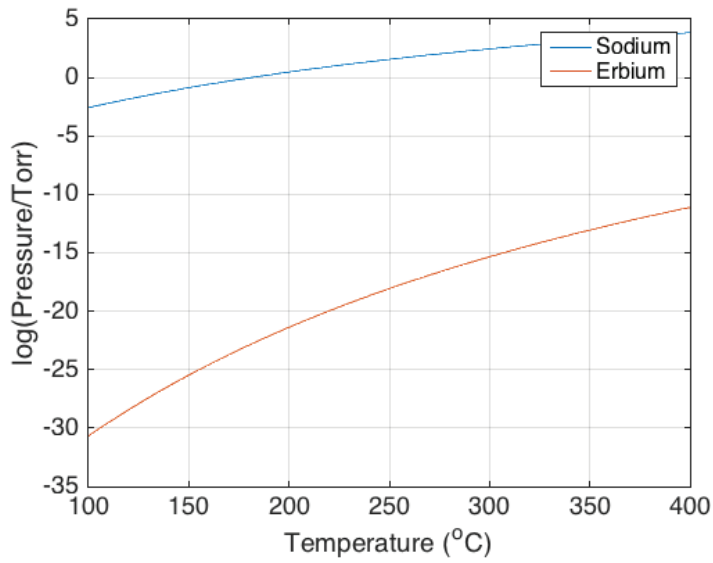


Figure 7.3: Vapor pressure of Sodium and Erbium as function of temperature [5].

scheme (see Sec. 4.2). At a relatively high temperature of 400°C, Erbium has a vapor pressure less than 10^{-10} torr, while for Sodium, it exceeds 10^3 torr. As a result, very few Erbium atoms are vaporized, resulting in a weak absorption and low signal-to-noise ratio. A possible solution is using a heat pipe to heat Erbium to very high temperatures. However, such systems are cumbersome and occupy significant optical table real estate. An alternative could be using an ultra-stable reference such as an Ultra-Low Expansion (ULE) cavity with frequency drifts in the order of tens of milli-hertz per second [106]. However, these are expensive, need special care such as vacuum engineering, and are overkill for our problem.

Since we already have a 589 nm laser locked to the D_2 transition of ^{23}Na , we developed a scheme to use this laser to frequency stabilize the Erbium 583 nm laser in a master-slave configuration. The locked master laser frequency drifts should be much smaller than the Sodium natural linewidth of 2π 9.8 MHz. We measured this drift to be

about 100 kHz over a 30 min period (using an Angstorm High Finesse WSU2 wavemeter), which could be further improved by simply increasing the bandwidth of the master laser locking electronics. One way of transferring this stability is by locking the length of an optical cavity to the master and then locking the slave to this cavity using a Pound Drever Hall (PDH) scheme [107]. Such a scheme can provide sub 100 Hz stability but involves setting up an entire locking apparatus, including cavity and electronics, for each slave laser. We decided to implement a Scanning Transfer Cavity (STC) scheme, which is bandwidth limited due to the piezo's slow scan rate but offers a much simpler system for locking multiple slave lasers to the same master. An STC is a Fabry Perot with piezo actuated length tunability. A beam from the master and each slave laser is sent into the cavity, while its length is scanned periodically. As the length scans, each of these beams resonates with the cavity's natural frequency and result in a transmission peak at the output. The time difference between these peaks gives an estimate of the frequency difference between the different lasers. This information is then used to generate a feedback signal using a servo to stabilize the slave frequency to the master. The scan rate of the STC piezo limits the bandwidth of such a locking scheme. Standard piezos are adequate for achieving our modest bandwidth requirements (200 mHz). In the following sections, I will first explain some of the basics of how Fabry Perot (FP) etalons work and then describe the design and construction of our STC.

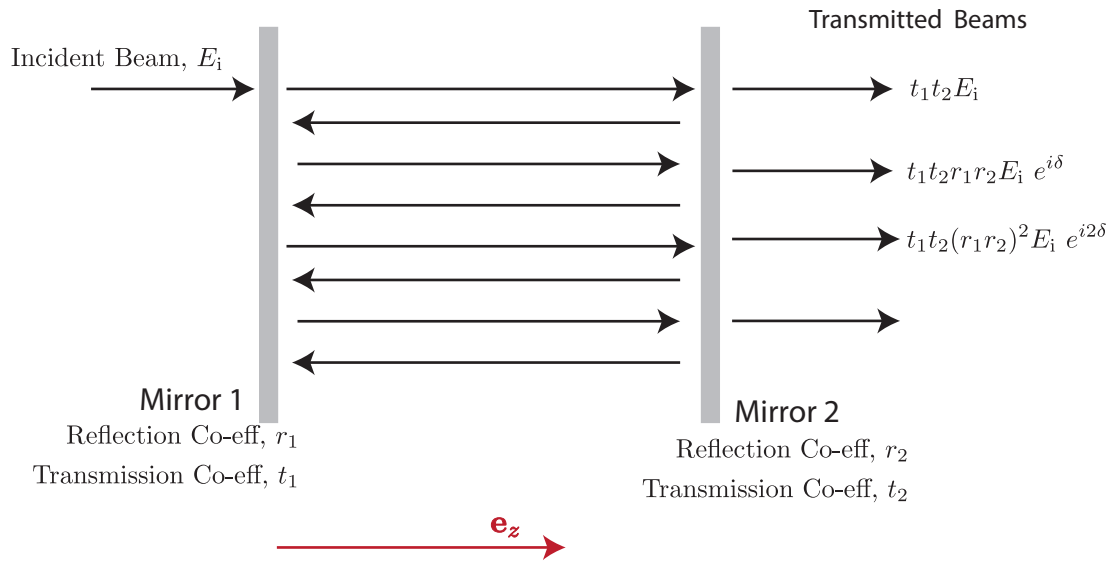


Figure 7.4: Interference in a simple Fabry Perot cavity. The beam on entering the cavity undergoes multiple reflections. These when constructively interfere lead to a maximum in transmission intensity.

7.3 Fabry Perot Etalons

In its simplest form, a Fabry Perot (FP) etalon consists of two parallel mirrors placed at a separation L , as shown in Fig. 7.4. Light enters the cavity from one of the mirrors, reflects multiple times, and eventually transmits through the other mirror. If the frequency of this light is in resonance with the cavity, the multiple paths constructively interfere and result in increased transmission intensity. Fig. 7.4 describes the amplification of light in a plane mirror FP cavity. Consider a monochromatic beam travelling along \mathbf{e}_z with electric field $E_i \propto e^{i\omega t - kz}$, incident on the front surface of the plane mirror cavity. Here t is time, ν is the frequency, and $k \mathbf{e}_z = 2\pi\nu/c \mathbf{e}_z$ is the propagation constant. The phase delay in each round trip is given by $\delta = 4\pi\nu L/c$, where L is the length of the cavity. Transmitted

beams from the different reflections add up to give a total transmission E_t , given by

$$E_t = E_i t_1 t_2 (1 + r_1 r_2 e^{i\delta} + (r_1 r_2)^2 e^{2i\delta} + \dots) = \frac{T}{1 - R e^{i\delta}} E_i, \quad (7.3)$$

where t_1, t_2 and r_1, r_2 are the transmission and reflection coefficients of the two mirrors, respectively, and T and R are defined as $T = t_1 t_2$ and $R = r_1 r_2$. The intensity corresponding to the transmitted electric field I_t is given by

$$I_t = E_t E_t^* = I_i \frac{(1 - R)^2}{(1 - R)^2 + 4R \sin^2 \delta/2}. \quad (7.4)$$

From Eq. (7.4), we see that the transmitted intensity I_t achieves its maximum value when

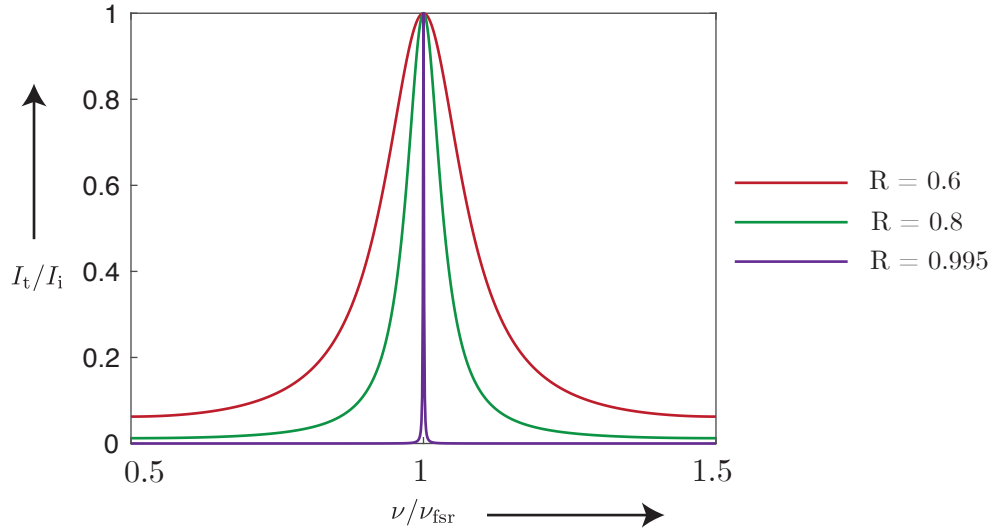


Figure 7.5: Cavity transmission peaks with varying mirror reflectivity R , according to Eq. (7.4). The red, green and purple curves correspond to a reflectivity R of 0.6, 0.8 and 0.995, respectively.

the round-trip phase delay $\delta = 2q\pi$, where q is an integer. This corresponds to frequencies $\nu = q \nu_{\text{fsr}}$, where $\nu_{\text{fsr}} = c/2L$ is the free spectral range of the cavity. Fig. 7.5 shows the

transmitted intensity as a function of laser frequency ν for different reflectivities R . As R increases, the linewidth of the transmission peak $\delta\nu$ decreases, thereby improving the frequency resolution of the cavity. The ratio of free spectral range ν_{fsr} to linewidth $\delta\nu$ is called finesse \mathcal{F} . It can be shown that in the absence of other losses, the finesse is simply a function of the reflectivity of the mirrors and is given by $\mathcal{F} = \pi\sqrt{R}/(1 - R)$ [108, 109]. Since the linewidth $\delta\nu$ is given by $\delta\nu = \nu_{\text{fsr}}/\mathcal{F}$, a high finesse helps achieve a narrow linewidth for a fixed free spectral range.

The finesse of a cavity is degraded by factors such as diffraction and mirror surface irregularities. Additionally, the finesse of a simple plane mirror FP is very sensitive to mirror alignment as small angular misalignments are equivalent to corresponding surface imperfections. In contrast, curved mirrors leave much more room for error as an angular misalignment merely redefines the optical axis [110]. Given the many advantages of resonators with curved mirrors, I will now formally explore the stability of modes in a cavity with mirrors of different curvatures.

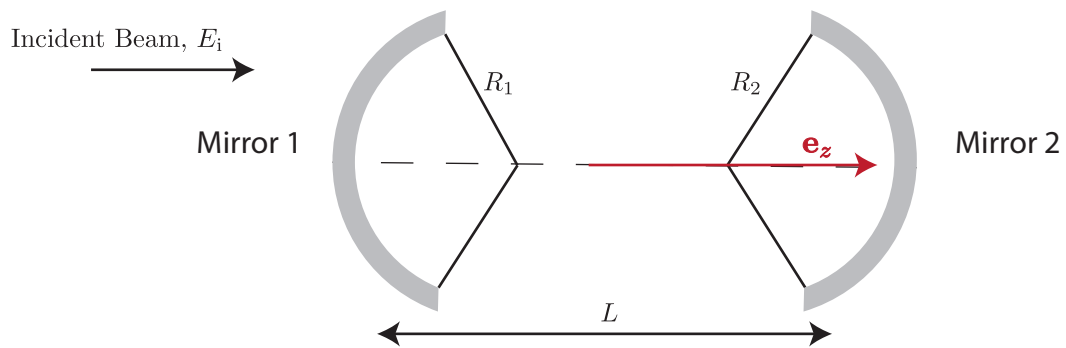


Figure 7.6: Schematic of a Fabry Perot with curved mirrors. The mirrors with radii of curvature R_1 and R_2 are separated by a distance d .

Resonance in a FP is achieved by ensuring the same field distribution after each

round trip. Consider a cavity of length L , made with mirrors of radius of curvatures R_1 and R_2 , as shown in Fig. 7.6. It can be shown that for an electromagnetic wave to replicate itself after each round trip, the geometry of the cavity should satisfy Eq. (7.5) [108, 109]

$$0 \leq \left(1 + \frac{L}{R_1}\right)\left(1 + \frac{L}{R_2}\right) \leq 1, \quad (7.5)$$

Fig. 7.7 graphically depicts the stability condition (Eq. (7.5)) as a function of g_1 and g_2 , where $g_1 = 1 + \frac{L}{R_1}$ and $g_2 = 1 + \frac{L}{R_2}$. The white region indicates the region of stability where Eq. (7.5) is satisfied. As evident from Fig. 7.7, plane parallel (point 1) and concentric (point 3) configurations lie at the edge of the stable region resulting in a fairly unstable modes. A symmetric confocal configuration (point 2) lies within the stable region and is very common for commercial FP cavities. Point 4 indicates the position of our STC which is made using a plane and curved mirror.

To find the resonance condition, we consider eigenmodes of a FP cavity with mirrors of arbitrary curvature. These eigenmodes can be described as Hermite Gauss modes of order (l, m) given by

$$U(x, y, z)_{l,m} = \frac{w_0}{w(z)} H_l \left(\frac{\sqrt{2}x}{w(z)} \right) H_m \left(\frac{\sqrt{2}y}{w(z)} \right) \exp \left(-i(kz - \Phi(l, m; z)) - i\frac{k}{2R}(x^2 + y^2) \right), \quad (7.6)$$

where $H_{n,m}$ are Hermite polynomials, $w(z)$ is the waist of the beam as a function of distance z from the focus in the direction of propagation, and w_0 is the minimum waist at the focus. The phase term $\Phi(l, m; z)$, called the guoy phase is given by $\Phi(l, m; z) = kz - (l+m+1) \zeta(z)$ where ζ is given by $\zeta(z) = \tan^{-1}(z/z_0)$, $z_0 = \pi w_0^2/\lambda$ is the Rayleigh

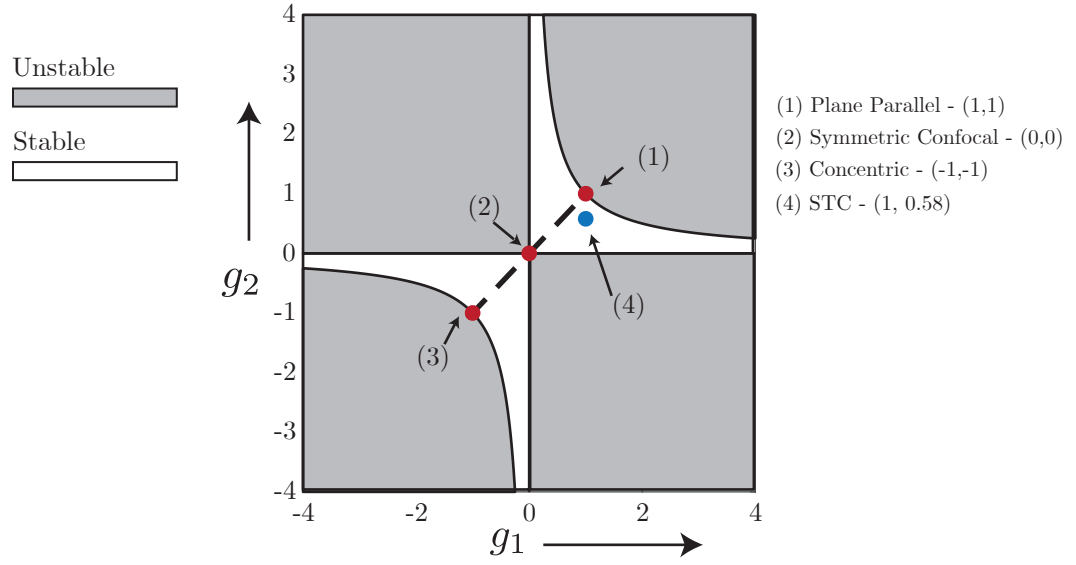


Figure 7.7: Stability diagram for a two mirror cavity based on Eq. (7.5). The red points (1), (2), and (3) indicate positions of plane parallel ($R_1 = R_2 = \infty$), symmetric confocal ($R_1 = R_2 = L/2$), and concentric ($R_1 = R_2 = L$) mirror configurations. The blue point (4) indicates the position of the STC.

length, and l and m are integers. The phase accumulated in each round trip is given by $2kL - 2(l + m + 1) \Delta\zeta$, where $\Delta\zeta$ can be approximated to $\Delta\zeta \approx \cos^{-1}(\pm\sqrt{g_1g_2})$.

Resonance in such cavities occurs for frequencies ν_{lmq} given by

$$\nu_{lmq} = \left(q + (l + m + 1) \frac{\cos^{-1}(\pm\sqrt{g_1g_2})}{\pi} \right) \frac{c}{2L}. \quad (7.7)$$

As evident from Eq. (7.7), geometries with $\cos^{-1}(\pm\sqrt{g_1g_2})/\pi$ equal to 0, 1/2 or 1 exhibit a great deal of degeneracy between axial and transverse modes. These correspond to plane-parallel, confocal and concentric arrangements, respectively. In cavities with degenerate modes, slight geometric deviations cause broadening of the cavity linewidth. Though such broadening eases coupling light into the cavity, it is not ideal for laser stabilization

purposes. For our STC, we use one plane and a $R = 500$ mm concave mirror separated by 210.5 mm. Such a plane-concave mirror configuration not only satisfies the stability criteria of Eq. (7.5) but also avoids degenerate modes. Point 4 in Fig. 7.7 depicts our STC.

7.4 Construction of the Setup

The setup for the STC lock includes a homemade Fabry Perot cavity, an electronic board for converting the analog cavity transmission peaks into digital pulses, and a microprocessor to generate the feedback to control the laser frequency. This section describes the construction of all three parts.

7.4.1 Cavity Construction

The FP cavity acts as a tunable, narrow bandpass filter capable of detecting the master-slave frequency difference with a precision better than the 583 nm Erbium transition natural linewidth. The time difference between the resonance peaks gives an estimate of the frequency difference. As a result, key considerations in its design are [110]

- mechanical stability and isolation from temperature and pressure fluctuations
- attainment of high finesse to obtain a narrow linewidth
- and an optimal optical layout to achieve mode matching.

We will touch upon these aspects in the following sections.

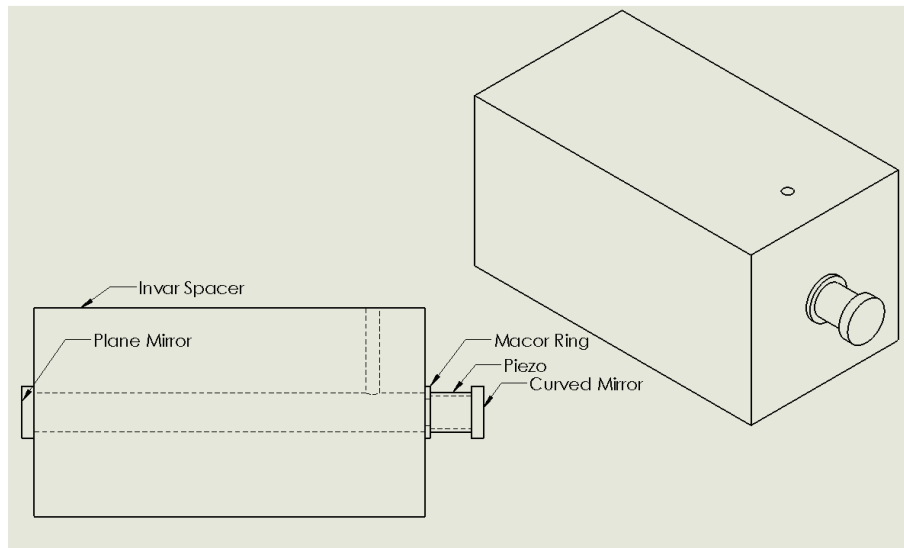


Figure 7.8: Schematic of the scanning Fabry Perot cavity. The curved mirror is attached to the piezo which is epoxied to the invar spacer via a macor ring. The plane mirror is attached on the other end of the spacer.

7.4.1.1 Mechanical and Thermal Stability

Fig. 7.9 is a schematic of the STC. It comprises a 'Invar36' metallic spacer, a piezo to scan the separation between the two resonator mirrors, and a macor ring between the piezo and spacer surfaces. Macor being an insulator avoids short-circuiting the inner and outer electrodes of the piezo. The two mirrors are glued to the ends of this assembly using 'Torr-Seal' epoxy. An important consideration for the cavity design is the drift in its free spectral range with ambient temperature changes. The length L in the expression $\nu_{\text{FSR}} = c/2L$ is the distance between the mirrors. In our case, it is the sum of the lengths of the invar spacer (L_{in}), macor ring (L_m) and piezo (L_p). For a 1°C rise in temperature,

the change in FSR, $\Delta\nu_{\text{fsr}}$ is given by

$$\Delta\nu_{\text{fsr}} = \frac{c}{2L} \frac{\Delta L_{in} + \Delta L_m + \Delta L_p}{L}, \quad (7.8)$$

where $\Delta L_{in/m/p}$ are the corresponding change in lengths. Since, for a 1° C rise in temperature, the fractional change in lengths are given by coefficients of thermal expansion (CTE), the above expression can be re written as

$$\Delta\nu_{\text{fsr}} = \nu_{\text{fsr}} \left(\alpha_{in} + \alpha_m \frac{L_m}{L_{in}} + \alpha_p \frac{L_p}{L_{in}} \right), \quad (7.9)$$

where $\alpha_{in/m/p}$ are the corresponding CTEs. Here, the length of the invar spacer is assumed to be very large compared to the macor and piezo. The CTE and dimensions of the different parts that make up the cavity are tabulated in Table 7.2.

Table 7.2: Thermal expansion of cavity parts.

Part	Material	CTE ($10^{-6}/^{\circ}\text{C}$)	Length (mm)	$\alpha_x \frac{L_x}{L_{in}}$ ($10^{-6}/^{\circ}\text{C}$)
Spacer (in)	Invar 36	1.2	190.5	1.2
Piezo (p)	APC Material- II	–	20	–
Insulating Ring (m)	Macor	5.2	2.54	0.069

It is evident from Table 7.2 that despite macor having a higher CTE, the invar spacer's expansion limits the thermal stability of cavity free spectral range. Invar was chosen for its low CTE. For a cavity with $\nu_{\text{FSR}} = 712 \text{ MHz}$, $\Delta\nu_{\text{fsr}} \approx 903 \text{ Hz}/^{\circ}\text{C}$, much smaller than the linewidth of the Erbium 583 transition. The piezo used is a standard, off-the-shelf ring piezo from 'APC International'. It is 20 mm long and has outer and inner

diameters 19 mm and 16 mm, respectively. The piezoelectric coefficient $d_{31} = -175$, resulting in an axial elongation of $0.467\mu\text{m}$ for every 200 V applied across the inner and outer electrodes. For a 200 mm long cavity, this corresponds to a frequency scan greater than $1.5 \times \nu_{\text{FSR}}$.

7.4.1.2 Finesse and Linewidth

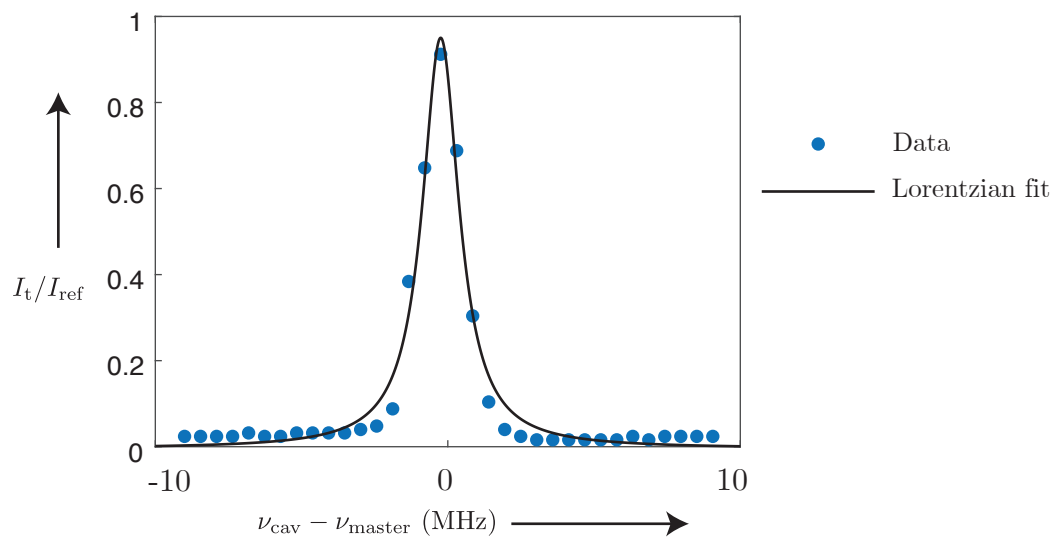


Figure 7.9: Linewidth measurement of the constructed STC. The blue points correspond to measured transmitted intensity I_t as the cavity piezo is scanned. The horizontal axis is the cavity resonance frequency ν_{cav} relative to the master laser frequency ν_{master} which serves as a reference. The black line is a Lorentzian fit to the data giving a linewidth of 1.14 MHz.

Our goal is to make a FP with the smallest possible linewidth. This can be achieved by either using mirrors with high reflectivity or by increasing the length of the FP. While higher reflectivities lead to larger finesse \mathcal{F} , large cavity lengths decrease the free spectral range ν_{FSR} . We use mirrors with 99.5% reflectivity, with an expectation of an ideal finesse of 625. Mirrors with reflectivities higher than this are very expensive. We decided to go with a cavity length of 210.5 mm; any longer would make aligning the laser beam

through the cavity challenging. This gives us a $\nu_{\text{FSR}} = 712$ MHz. Based on the ideal finesse of 625, we expected to get a cavity linewidth of 1.14 MHz. Fig. 7.9 shows one of 589 peaks as the cavity's natural frequency ν_c is varied. By fitting the transmission peak to a Lorentzian line-shape and assuming a 712 MHz FSR, we obtain a linewidth of 1.5(2) MHz, corresponding to a finesse $\mathcal{F} = 469$.

7.4.1.3 Mode matching

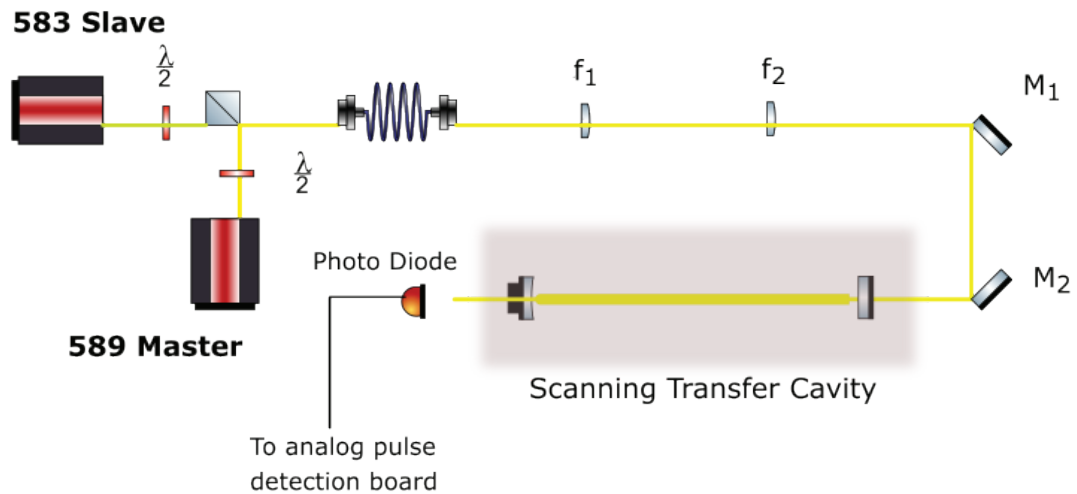


Figure 7.10: Optical setup of the scanning transfer cavity. Light from the two lasers are couple into a fiber and sent to the STC. Lenses with focal length $f_1 = 150\text{mm}$ and $f_2 = 100\text{mm}$ are used to mode match to the cavity.

Fig. 7.10 shows a schematic of the STC and associated optics. To couple maximum light into the (0,0) Hermite gauss cavity mode, the beam's wavefront curvature should match that of the mirrors at their respective locations [111, 112]. This corresponds to a 500 mm curvature at the curved mirror and minimum waist at the flat mirror. Since the length of the cavity (L) is 210.5 mm, the required waist size at the plane mirror can be

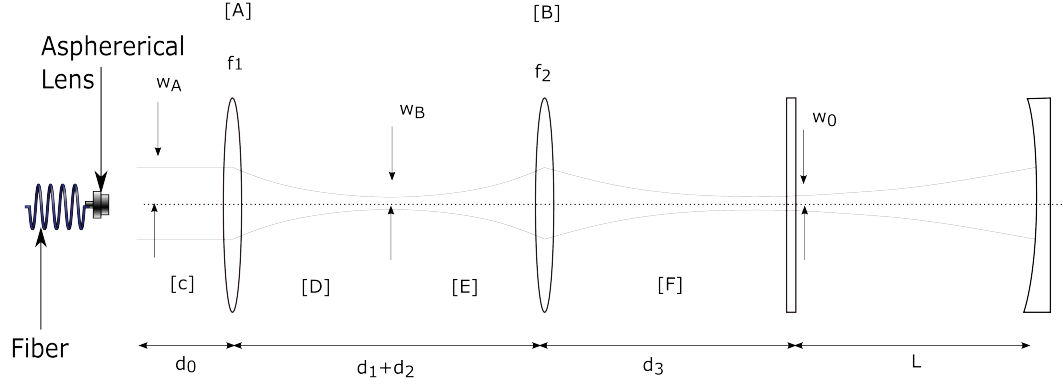


Figure 7.11: Mode matching optics for the cavity. The Gaussian beam from the fiber is collimated using an asphere. Lenses f_1 and f_2 are placed appropriately to achieve mode matching. d_i 's are the distances between the various components. d_0, d_1, d_2 and d_3 are 127, 150, 120 and 317.5 mm respectively.

estimated using Eq. 7.10.

$$R(L) = L\left(1 + \left(\frac{z_R}{L}\right)^2\right) \implies z_R = L\sqrt{\frac{R}{L} - 1} \quad (7.10)$$

$$z_R = \pi w_0^2 / \lambda \implies w_0 = \sqrt{\frac{\lambda z_R}{\pi}}$$

where z_R is the Rayleigh length. This turns out to be 215.133 μm . We achieve this using two lenses of focal lengths f_1 and f_2 . We perform a ray matrix analysis to determine appropriate placement of these lenses [109, 111, 112]. The optical setup is as shown in Fig. 7.11 where capital letters indicate the ray transfer matrix of each optical element. Matrices for the two lenses with focal length f_1 and f_2 are given by Eq. 7.11. C, D, E and F are the matrices for propagation in free space.

$$\begin{aligned}
A &= \begin{bmatrix} 1 & 0 \\ -\frac{1}{f_1} & 1 \end{bmatrix} & B &= \begin{bmatrix} 1 & 0 \\ -\frac{1}{f_2} & 1 \end{bmatrix} \\
C &= \begin{bmatrix} 1 & 0 \\ d_0 & 1 \end{bmatrix} & D &= \begin{bmatrix} 1 & 0 \\ d_1 & 1 \end{bmatrix} & E &= \begin{bmatrix} 1 & 0 \\ d_2 & 1 \end{bmatrix} & F &= \begin{bmatrix} 1 & 0 \\ d_3 & 1 \end{bmatrix}
\end{aligned} \tag{7.11}$$

When solved we obtain the following results.

$$\begin{aligned}
w_B &= \frac{2f_1 w_A}{\sqrt{4d_0^2 - 8d_0 f_1 + 4f_1^2 + k^2 w_A^4}} \\
d_1 &= -\frac{f_1(-4d_0^2 + 4d_0 f_1 - k^2 w_A^4)}{4d_0^2 - 8d_0 f_1 + 4f_1^2 + k^2 w_A^4} \\
d_2 &= \frac{2f_2 w_0^2 + \sqrt{4f_2^2 w_0^2 w_B^2 - k^2 w_0^4 w_B^4}}{2w_0^2} \\
d_3 &= \frac{2f_2 w_B^2 + \sqrt{4f_2^2 w_0^2 w_B^2 - k^2 w_0^4 w_B^4}}{2w_B^2}
\end{aligned} \tag{7.12}$$

In our setup, light out of the fiber is collimated into a beam of $430 \mu\text{m } 1/e^2$ radius, using an aspheric lens. The first spherical lens is placed 127 mm (d_0) away from the asphere. The two lenses have focal lengths $f_1 = 150$ and $f_2 = 100$ mm. This gives a value of 150, 120 and 317.5 mm for d_1 , d_2 and d_3 respectively. Once mode matched, we perform a two-mirror walk with mirrors M_1 and M_2 (see Fig. 7.10) to maximize coupling. This step is tricky as the cavity is single mode. Two things make this process slightly easier. First, we try to align the beam reflected off the first cavity mirror with the input beam. Second, we look at the transmitted cavity mode on a camera while walking the mirrors and scanning the cavity. When roughly aligned, we see multiple modes on the camera as the cavity scans. A photodetector will capture these different modes as multiple peaks for a single free spectral range scan. The rest of the alignment is done with the goal of

eliminating all but one mode.

7.4.2 Electronics

7.4.2.1 Pulse Detection Board

The photodetector at the output of the cavity (see Fig. 7.10) detects the transmitted light. We designed an electronics board to detect peaks in transmission intensity and generate digital pulses whenever they occur. Fig. 7.12 is a schematic of this circuit. The photodetector signal is sent through two channels. One detects voltage values greater than a certain threshold using a commercial comparator. The other detects a local maximum in voltage using a differentiator and comparator in series. The differentiator generates a derivative of the signal, which is compared against a reference. A NAND gate takes the output of these channels and goes to a digital LOW when both conditions are satisfied. Fig. 7.12 depicts how the different components in the circuit work. The LOW pulses generated by the NAND gate serve as the digital input to the microprocessor.

7.4.2.2 Microprocessor

The microprocessor used is a Teensey 3.2 board. An Arduino IDE code evaluates the time difference between two consecutive peaks as the cavity scans. This code also eliminates spurious peaks detected by the photo-diode at the exit of the cavity. We generate an analog feedback signal using the Audrino PI library, which is fed to the slave laser's ECDL grating piezo. While implementing this code, we realized that each cavity transmission peak generates multiple digital pulses, as shown in Fig. 7.13. The

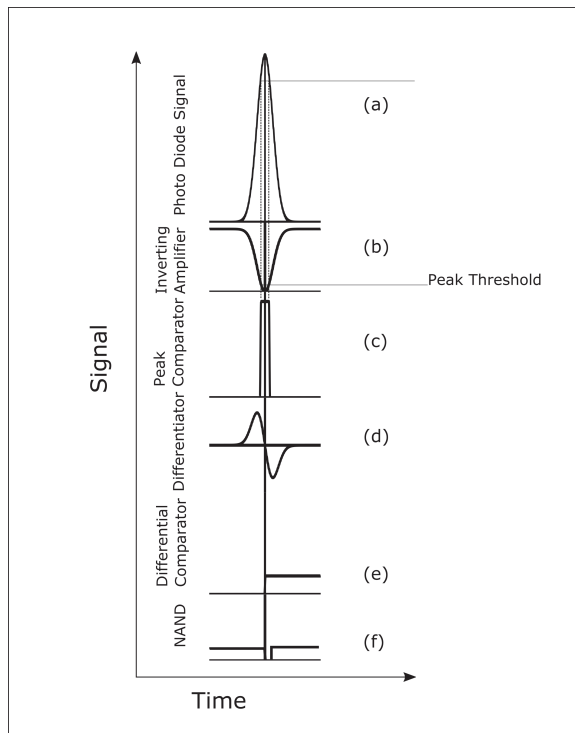
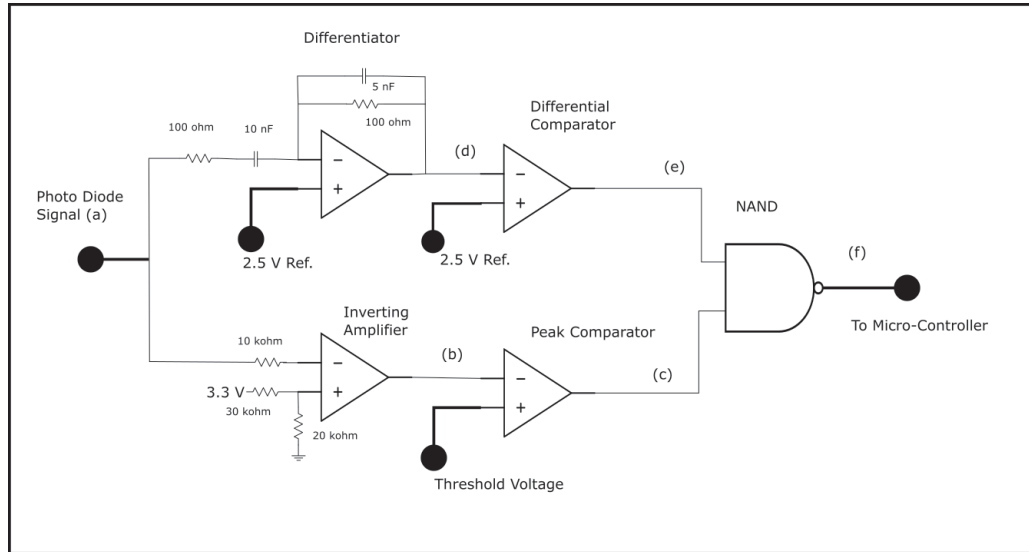


Figure 7.12: Pulse Detection action by the analog board. A voltage pulse (a) detected in the photo diode is sent through a number of electronic components which ultimately drive the NAND gate signal (f) LOW. This digital pulse is fed to the micro controller.

yellow curve in Fig. 7.13 is a transmission peak, and purple pulses are digital inputs generated by the analog pulse detection board. Due to non-uniform motion of the cavity

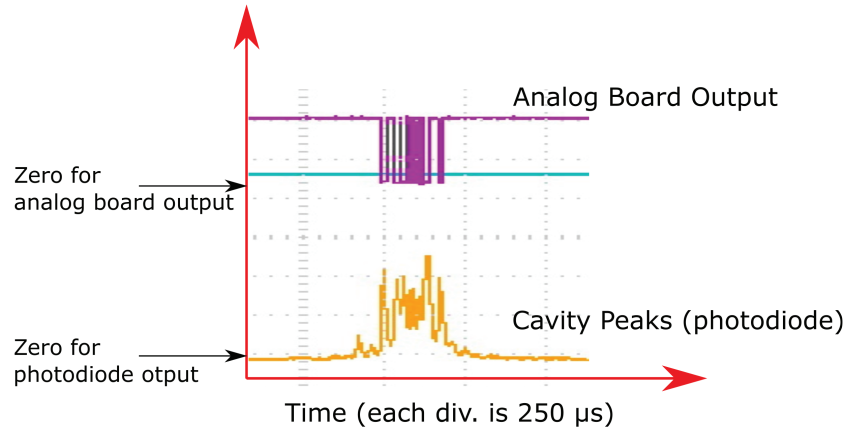


Figure 7.13: Non-uniform motion of the piezo leads to multiple kinks on the cavity transmission peak. The yellow curve is the transmission peak and purple is the digital signal sent to the microprocessor, signaling a transmission peak's occurrence. Each vertical division is 500 mV for yellow and 2V for purple. Each division on the horizontal axis is 250 μ s.

piezo, the transmission peaks have multiple kinks, resulting in multiple digital pulses. The analog board interprets these kinks as separate peaks and sends out false signals to the microprocessor. We get around this problem by rejecting inputs that are spaced closely in time.

7.5 Results and Outlook

The microprocessor's Proportional Integral (PI) output controls the slave's ECDL grating piezo voltage as the cavity scans. PI gains and set-points are digitally controlled by turning rotary encoders on the analog electronics board. We were successful in locking the 583 nm slave to the locked master. Also, we were able to scan the slave by scanning the master laser frequency by 5 MHz in 0.5 s, indicating qualitative stability of the lock for slow drifts, as shown in Fig. 7.14. The frequency stability of the locked laser was

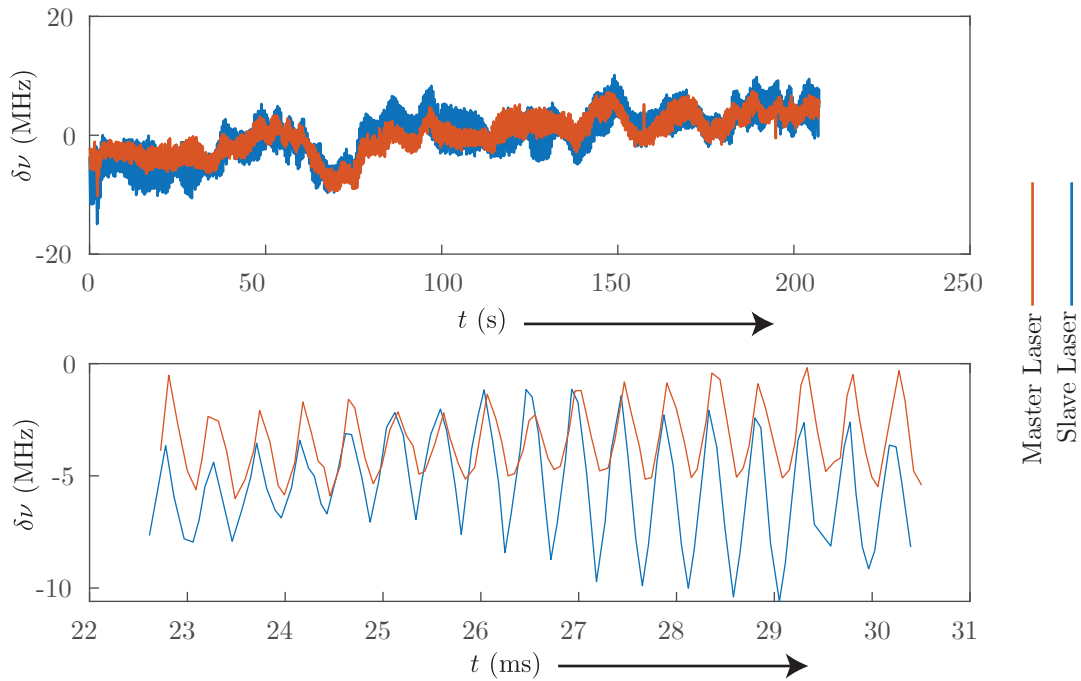


Figure 7.14: Master and slave frequency drifts $\delta\nu$ as the master oscillates and drifts. The master SatAbs lock was dis-engaged and the master laser frequency was modulated by 5MHz in a period of 0.5 s. The top panel is data acquired over long periods and shows the overall drift in the mean frequency. The bottom panel is a zoomed-in version of the top panel. Measurements were made using the 'Angstorm WSU2' wavemeter via a fiber switch.

measured using an 'Angstorm high finesse WSU2' wavemeter. Fig. 7.15 is a histogram of the slave frequency measured over 1 minute of it being locked and unlocked. The locked laser clearly has a smaller spread in frequencies than when it's unlocked. However, the frequency spread is roughly 1.5 MHz, similar in magnitude to the cavity linewidth. Ideally, we expect the cavity to resolve frequencies much smaller than its linewidth. In this case, the sub-optimal resolution can be attributed to the non-uniform motion of the cavity piezo, as shown in Fig. 7.13. The analog board reads these kinks as individual peaks and sends the information to the microprocessor. Though the microprocessor code

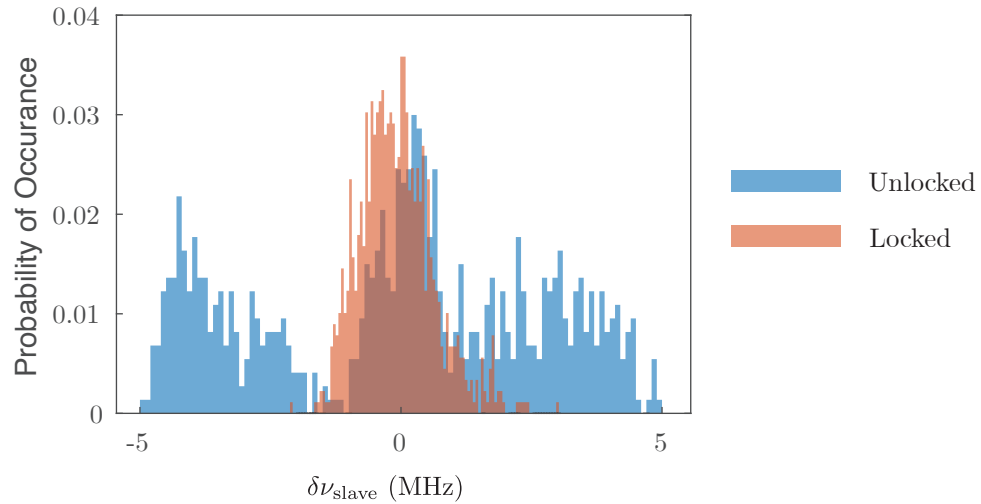


Figure 7.15: Histogram of the slave frequencies as it is locked (red) and unlocked (blue). Measurements were made using the 'Angstrom WSU2' wavemeter via a fiber switch.

picks only one of the many digital pulses, this could correspond to any position on the cavity peak. As a result, we should expect uncertainty in frequency estimation equal to the cavity linewidth. To investigate this hypothesis, we look at the cavity transmission peaks as we scan the laser frequency but hold the piezo stationary. Fig 7.16 (a) shows the cavity transmission peaks when the cavity is scanned, but the laser frequency is held constant. Fig 7.16 (b) corresponds to the opposite case where the laser is scanned, but the cavity is held stationary. The kinks in the transmission peaks appear only when the cavity is scanned, thereby indicating a non-uniform piezo motion. Even though this STC setup has failed to stabilize the 583 nm slave laser within the Erbium atomic transition natural linewidth (2π 170 MHz), we have successfully identified a major shortcoming in the scanning motion of the piezo. A possible reason for the non-uniform motion could be the excessive weight of the piezo. By replacing this with a lighter piezo and stacking the cavity vertically we might be able to relieve some of the strain in its free movement,

thereby eliminating the kinks in the cavity transmission peaks.

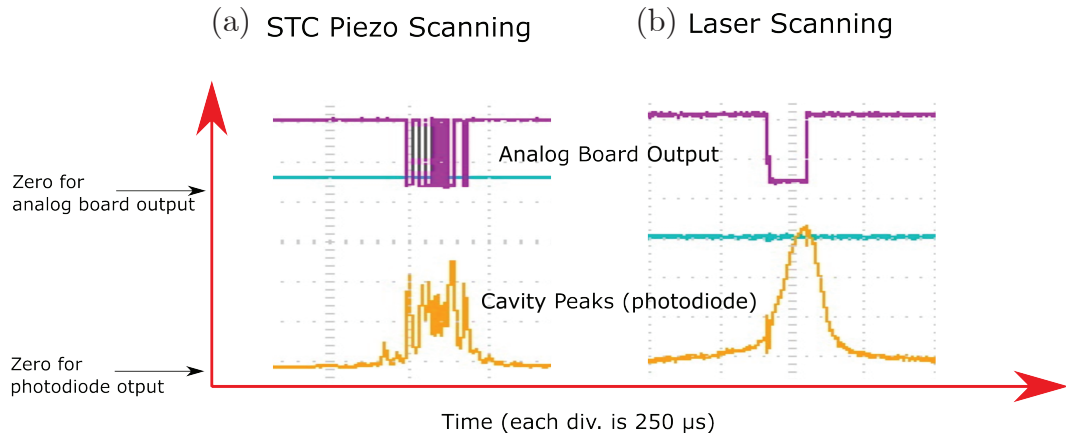


Figure 7.16: Cavity transmission peaks (yellow curve) and corresponding pulses generated by analog board (purple) as the cavity (a) or laser (b) is scanned in frequency. Each vertical division is 500 mV for yellow and 2V for purple. Each division on the horizontal axis is 250 s. The above data was taken by scanning the cavity and laser at 3.4 GHz/s.

Chapter 8: Conclusions and Outlook

While building this new apparatus, we made several improvements to alleviate many of the problems faced in the previous setup. For example, the imaging system in the previous experiment had a numerical aperture of 0.09 and the response was heavily aberrated [38]. The current experiment has an improved imaging system with a numerical aperture of 0.28 and is designed for minimal aberrations [64]. One can gauge the degree of improvement by comparing the typical radial trap frequencies of the toroidal traps. In this apparatus, we make rings with radial trap frequencies $\omega_r = 2\pi \cdot 500$ Hz, a factor of five better than the NIST experiment. Moreover, for the NIST experiment, it was impossible to create uniform rings without making significant corrections to the spatial mode of the DMD ODT beam. For the analogue cosmology experiment, tighter radial confinement has allowed us to explore rapid expansion and contractions without exciting collective modes in the radial direction, thereby making our system more 1D than the NIST version. In future, we plan to exploit this improved resolution for a better phonon detection threshold and attempt to observe spontaneous pair production. Some progress has been made in this direction (see Appendix A). Additionally, the improved resolution will help create weak links of much smaller dimensions, enabling the study of tunneling effects in a superfluid ring and building upon our previous work in atomtronic circuits [17–19].

Another significant improvement was switching the Zeeman slower source with a more compact 2D MOT. This source is at least three times smaller in volume and doesn't have large electromagnets with long tun-off times. Since we plan on making a dual-species BEC with highly magnetic Erbium, this is particularly useful. The long-range and anisotropic nature of dipole-dipole interactions in Erbium makes it an exciting candidate for strongly correlated many-body physics. Erbium has many Feshbach resonances which are densely packed. Its bosonic isotopes ^{168}Er and ^{166}Er , have respectively 190 and 189 resonances over 70G [100]. This makes Erbium a promising candidate for applications involving tuning interactions, not limited to but including analogue cosmology.

Appendix A: Characterizing Imaging Aberrations

To extend the cosmological analogy to the quantum domain, we plan on exploring the phenomena of pair production in the early universe [21, 92, 113–116]. As illustrated by our previous work [41], this involves the precise detection of spontaneously generated excitations, which relies on the ability to resolve spatial correlations caused by them. The healing length of condensates ξ determines the length scale of these correlations. Eq. (A.1) defines the healing length [33] as

$$\xi = \sqrt{\frac{\hbar^2}{2m\mu}}, \quad (\text{A.1})$$

where m is the mass of an atom, and μ is the chemical potential of the BEC. Fig. A.1 helps in visualizing these length scales in the context of imaging systems with different resolutions. Fig. A.1 (a) corresponds to a system whose spatial resolution is limited by the pixel size l_{min} , as indicated by the grid. Fig. A.1 (b) corresponds to a system whose resolution spot size is significantly larger than the camera pixel size. The solid and dashed circles represent atoms as imaged by the two imaging systems. The thermal De-Broglie wavelength λ_{dB} represents the spatial extent of atoms. These appear as objects of size R when imaged through an imaging system with a finite resolution, as shown in Fig. A.1 (b). Fig. A.1 (c) depicts these length scales in the Fourier domain, indicating the spatial

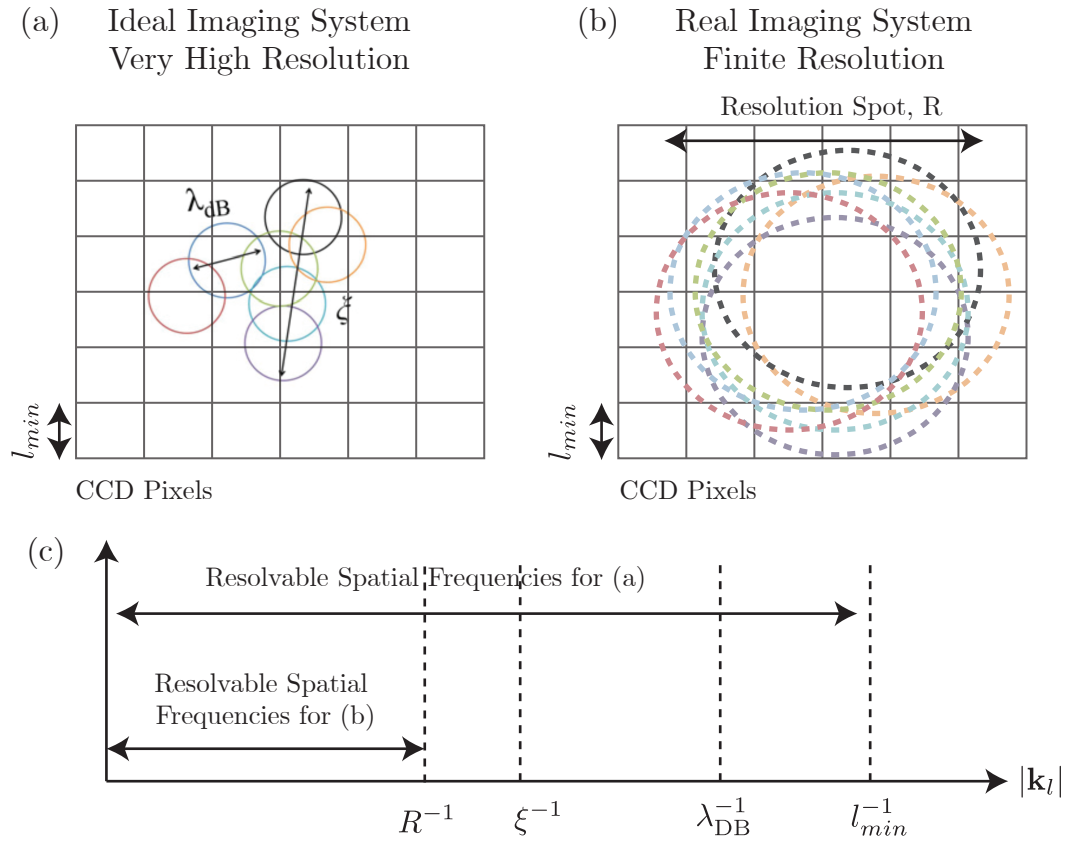


Figure A.1: Comparison of length and spatial frequency scales for imaging BECs. (a) and (b) correspond to imaging systems with spatial resolutions l_{min} and R . The grid represents camera pixels. Thermal De-Broglie wavelength λ_{dB} and healing length ξ are indicated. The dashed circles in (b) correspond to (a)'s solid circles of the same color. (c) Length scales in (a) and (b) in the Fourier domain.

frequencies resolved by the two imaging systems. Ideally, we wish to have an imaging resolution much smaller than ξ so that resolving spatial correlations for frequencies near and smaller than ξ^{-1} is straightforward. However, since our typical chemical potentials are of the order of 1 kHz, $\xi < 1 \mu\text{m}$, which is of the same order as our imaging system's diffraction-limited resolution. As a result, imaging systematics such as diffraction and aberrations obscure the correlation information. Ref. [117, 118] derives a method to determine these systematic effects in an uncorrelated atomic sample experimentally. We employ the same technique to characterize the modulation transfer function (MTF) of our imaging system.

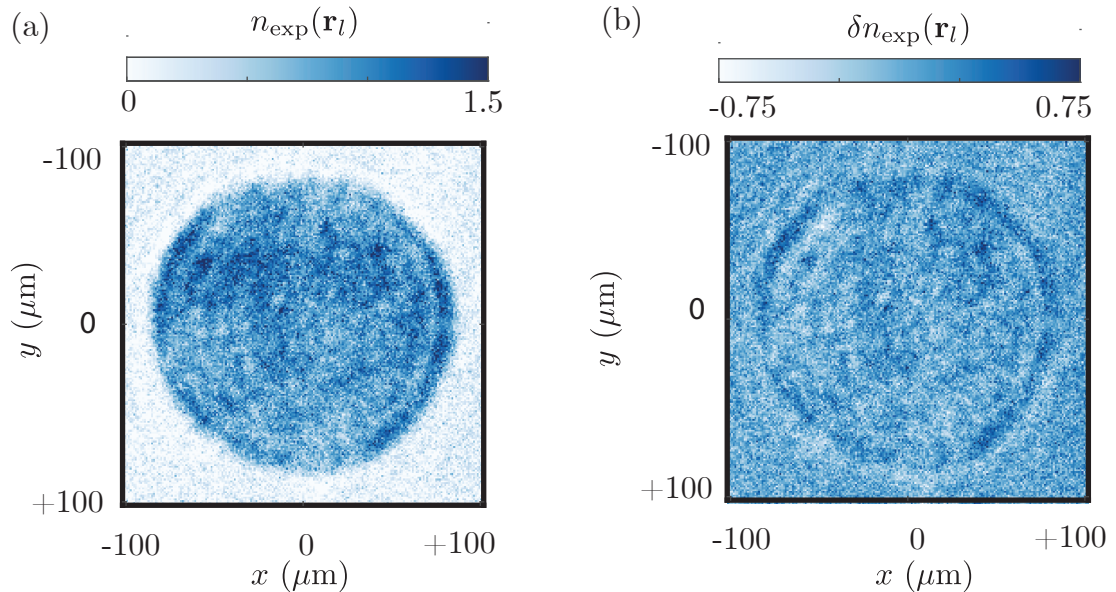


Figure A.2: (a) Atomic density of weakly interacting disk-shaped BEC $n_{\text{exp}}(\mathbf{r}_l)$. (b) Density variation of (a) $\delta n_{\text{exp}}(\mathbf{r}_l)$ about the average 50 shots. The densities in both (a) and (b) are in the same arbitrary units.

We start by acquiring images of 50 similar atomic samples of weakly interacting BECs. The 2D column densities corresponding to each of the 50 samples are similar but not identical. Fig. A.2 (a) is the density corresponding to one of these samples

$n_{\text{exp}}(\mathbf{r}_l)$, and Fig. A.2 (b) is its density fluctuation about the mean density evaluated across the 50 samples $\delta n_{\text{exp}}(\mathbf{r}_l) = n_{\text{exp}}(\mathbf{r}_l) - \langle n_{\text{exp}}(\mathbf{r}_l) \rangle$, where $\langle \dots \rangle$ denotes averaging across the 50 samples. These fluctuations in the atomic density δn_{exp} are a result of shot-noise. Therefore for an ideal imaging system, we expect the density fluctuation power spectrum $\left| \widetilde{\delta n_{\text{exp}}}(\mathbf{k}_l) \right|^2$ to be spectrally flat, where $\widetilde{\cdot}$ represents spatial Fourier transform. However, due to the finite resolution of the imaging system, diffraction and imaging aberrations result in stronger density-density correlations for spatial frequencies less than R^{-1} , conveniently giving a measure of the MTF. According to [117], the Fourier transform of the MTF, $\mathcal{M}(\mathbf{k}_l)$ is related to the average of the density fluctuation power spectrum $\left\langle \left| \widetilde{\delta n}(\mathbf{k}_l) \right|^2 \right\rangle$ by the equation

$$\mathcal{M}^2(\mathbf{k}_l) = \left\langle \left| \widetilde{\delta n}(\mathbf{k}_l) \right|^2 \right\rangle. \quad (\text{A.2})$$

Fig. A.3 (a) is the experimentally obtained RHS of Eq. (A.2) estimated by averaging $\left| \widetilde{\delta n_{\text{exp}}}(\mathbf{k}_l) \right|^2$ across the 50 images. The strong DC component arises due to the finite extent of the atomic cloud and needs to be removed for accurate determination of the MTF. For this, we refer to the relationship between the Fourier transformed MTF $\mathcal{M}(\mathbf{k}_l)$ and the resonant absorption imaging pupil function p , derived in [117]. The relationship is given by

$$\mathcal{M}^2 = \left\langle \left| \widetilde{\delta n}(\mathbf{k}_l) \right|^2 \right\rangle = \left| \mathcal{R}[\widetilde{p}] \right|^2, \quad (\text{A.3})$$

where the pupil function can be represented in the form of amplitude A and wavefront Θ

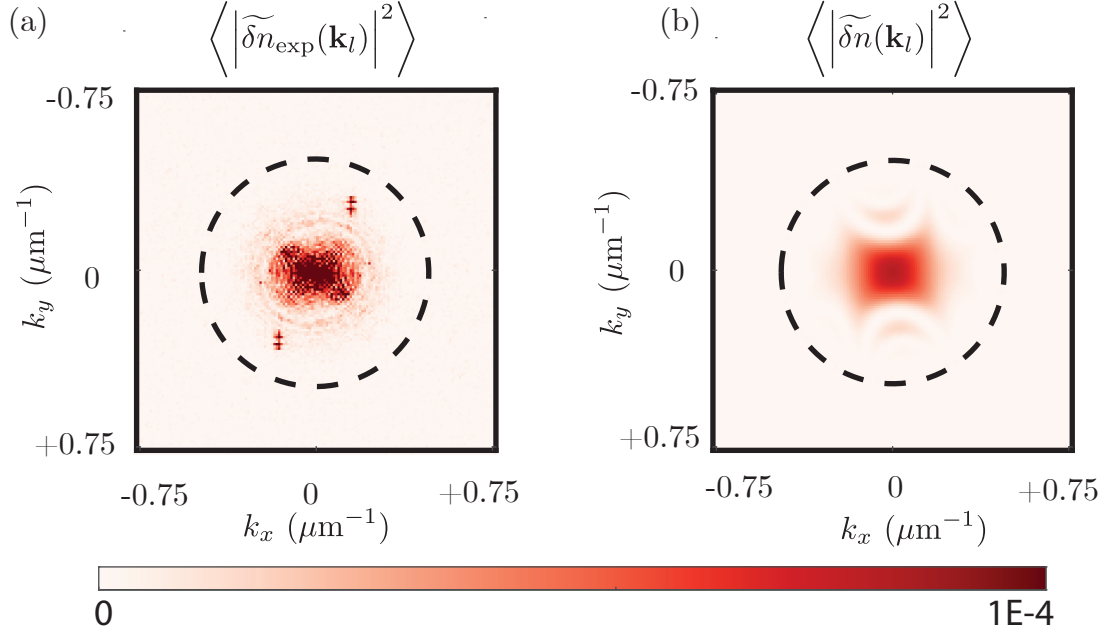


Figure A.3: (a) Experimentally evaluated density fluctuation power spectrum as a function of the spatial frequency \mathbf{k}_l . (b) Result of fitting (a) to Eq. A.4. The dashed circles enclose resolvable spatial frequencies for an imaging system with NA = 0.28. The color bar holds for both (a) and (b).

aberrations as

$$p(\mathbf{r}) = A(\mathbf{r}) e^{i2\pi\Theta(\mathbf{r})}. \quad (\text{A.4})$$

We fit the experimentally obtained $\langle |\widetilde{\delta n}_{\text{exp}}(\mathbf{k}_l)|^2 \rangle$ (see Fig. A.3 (a)) to the pupil function (A.4) with the wavefront aberration represented by an even polynomial of order six. Fig. A.3 (b) shows the fitted $\langle |\widetilde{\delta n}(\mathbf{k}_l)|^2 \rangle$, which according to Eq. (A.2) is equal to $\mathcal{M}^2(\mathbf{k}_l)$. This fitted MTF doesn't have the spurious DC component. Fig. A.4 (a) shows the wavefront aberration Θ obtained from the fit. As a sanity check, we go a step further and estimate the types of aberrations present in our imaging system, which involves projecting the wavefront aberration Θ onto a Zernike polynomial basis [119], to obtain the first 10

Zernike coefficients. Fig. A.4 (b) is the wavefront aberration reconstructed from these Zernike coefficients.

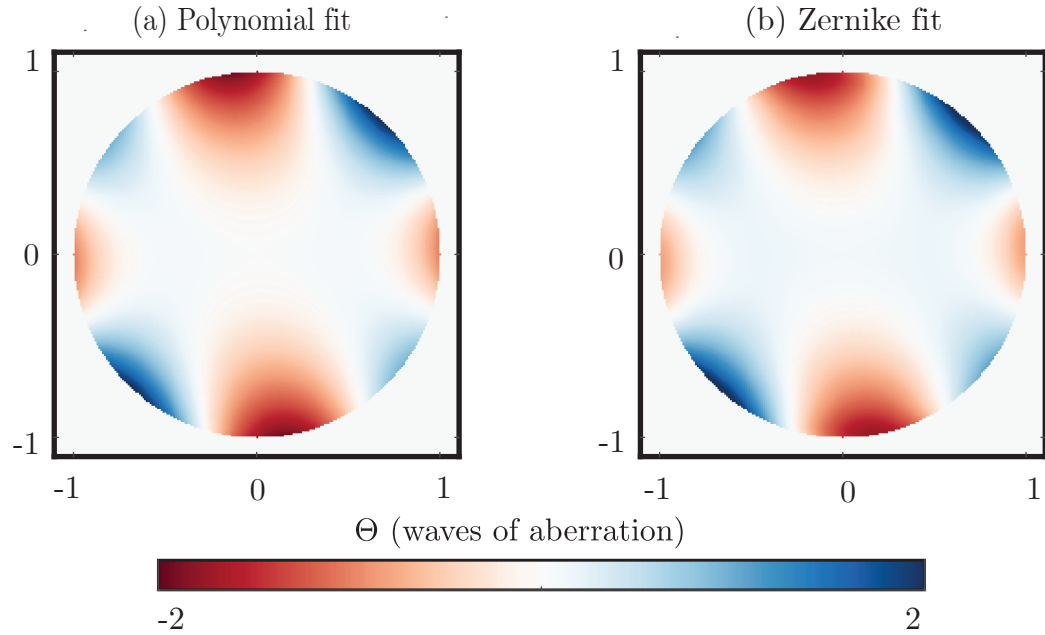


Figure A.4: (a) Wavefront aberration determined by fitting Fig. A.4 (a) to Eq. A.4. (b) Wavefront aberration reconstructed by projecting (a) onto a Zernike polynomial basis.

Our next goal is to intentionally introduce an aberration in our system and then look for the desired effect, serving as a sanity check for the above scheme. Since we have complete control over the system defocus, we now concentrate on the Zernike defocus coefficient Z_0^2 . Fig. A.5 (a) is a schematic of the imaging system where z_i is the distance between the exit pupil and the camera. We intentionally defocus the system by varying z_i and record the Zernike defocus coefficient Z_0^2 . Fig. A.5 (b) plots Z_0^2 as a function of Δz_i . $\Delta z_i = 0$ represents the optimal focal position. As z_i is varied on either side of this optimal value, Z_0^2 increases in magnitude, thereby confirming optimal focus at $\Delta z_i = 0$.

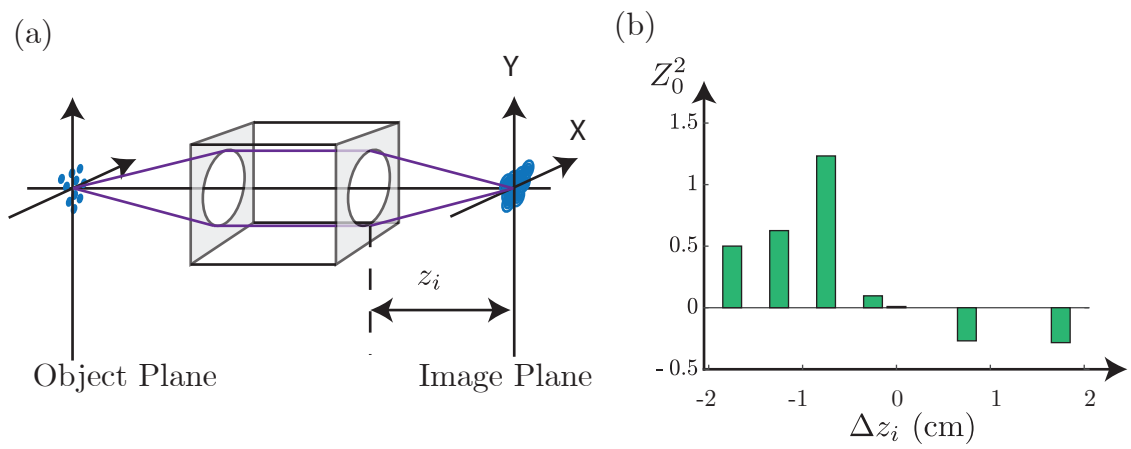


Figure A.5: Experiment to deterministically change the system defocus. (a) The imaging system with image distance z_i as indicated. (b) Variation of Zernike defocus coefficient Z_0^2 as a function of Δz_i .

Bibliography

- [1] H. Y. Ban, M. Jacka, J. L. Hanssen, J. Reader, and J. J. McClelland. Laser cooling transitions in atomic erbium. *Opt. Express*, 13(8):3185–3195, Apr 2005.
- [2] D. A. Steck. Sodium 23 D Line Data, 2010.
- [3] Toptica Photonics. *Tunable Diode Lasers*, 2018.
- [4] Jeffrey Garver Lee. *Dissipation in a superfluid atom circuit*. PhD thesis, University of Maryland, 2011.
- [5] C. B. I. V. P. Alcock and M. K. Horrigan. Vapor pressure of the metallic elements. *Canadian Metallurgical Quarterly*, 23:309, 1984.
- [6] M. H. Anderson, J. R. Ensher, M. R. Matthews, C. E. Wieman, and E. A. Cornell. Observation of bose-einstein condensation in a dilute atomic vapor. *Science*, 269(5221):198–201, 1995.
- [7] K. B. Davis, M. O. Mewes, M. R. Andrews, N. J. van Druten, D. S. Durfee, D. M. Kurn, and W. Ketterle. Bose-einstein condensation in a gas of sodium atoms. *Phys. Rev. Lett.*, 75:3969–3973, Nov 1995.
- [8] Markus Greiner, Olaf Mandel, Theodor W. Hänsch, and Immanuel Bloch. Collapse and revival of the matter wave field of a bose–einstein condensate. *Nature*, 419(6902):51–54, 2002.
- [9] D. Jaksch, C. Bruder, J. I. Cirac, C. W. Gardiner, and P. Zoller. Cold bosonic atoms in optical lattices. *Physical Review Letters*, 81(15):3108–3111, 1998.
- [10] Markus Greiner, Cindy A. Regal, and Deborah S. Jin. Emergence of a molecular bose–einstein condensate from a fermi gas. *Nature*, 426(6966):537–540, 2003.
- [11] S. Jochim, M. Bartenstein, A. Altmeyer, G. Hendl, C. Chin, J. Hecker Denschlag, and R. Grimm. Pure gas of optically trapped molecules created from fermionic atoms. *Phys. Rev. Lett.*, 91:240402, Dec 2003.

- [12] J. Cubizolles, T. Bourdel, S. J. J. M. F. Kokkelmans, G. V. Shlyapnikov, and C. Salomon. Production of long-lived ultracold Li_2 molecules from a fermi gas. *Phys. Rev. Lett.*, 91:240401, Dec 2003.
- [13] Kevin E. Strecker, Guthrie B. Partridge, and Randall G. Hulet. Conversion of an atomic fermi gas to a long-lived molecular bose gas. *Phys. Rev. Lett.*, 91:080406, Aug 2003.
- [14] L. Amico, M. Boshier, G. Birkl, A. Minguzzi, C. Miniatura, L.-C. Kwek, D. Aghamalyan, V. Ahufinger, D. Anderson, N. Andrei, A. S. Arnold, M. Baker, T. A. Bell, T. Bland, J. P. Brantut, D. Cassettari, W. J. Chetcuti, F. Chevy, R. Citro, S. De Palo, R. Dumke, M. Edwards, R. Folman, J. Fortagh, S. A. Gardiner, B. M. Garraway, G. Gauthier, A. Günther, T. Haug, C. Hufnagel, M. Keil, P. Ireland, M. Lebrat, W. Li, L. Longchambon, J. Mompart, O. Morsch, P. Naldesi, T. W. Neely, M. Olshanii, E. Orignac, S. Pandey, A. Pérez-Obiol, H. Perrin, L. Piroli, J. Polo, A. L. Pritchard, N. P. Proukakis, C. Rylands, H. Rubinsztein-Dunlop, F. Scazza, S. Stringari, F. Tosto, A. Trombettoni, N. Victorin, W. von Klitzing, D. Wilkowski, K. Xhani, and A. Yakimenko. Roadmap on atomtronics: State of the art and perspective. *AVS Quantum Science*, 3(3):039201, 2021.
- [15] R. A. Pepino, J. Cooper, D. Z. Anderson, and M. J. Holland. Atomtronic circuits of diodes and transistors. *Phys. Rev. Lett.*, 103:140405, Sep 2009.
- [16] M. C. Beeler, R. A. Williams, K. Jiménez-García, L. J. LeBlanc, A. R. Perry, and I. B. Spielman. The spin hall effect in a quantum gas. *Nature*, 498(7453):201–204, 2013.
- [17] S. Eckel, F. Jendrzejewski, A. Kumar, C. J. Lobb, and G. K. Campbell. Interferometric measurement of the current-phase relationship of a superfluid weak link. *Phys. Rev. X*, 4:031052, Sep 2014.
- [18] Stephen Eckel, Jeffrey G. Lee, Fred Jendrzejewski, Noel Murray, Charles W. Clark, Christopher J. Lobb, William D. Phillips, Mark Edwards, and Gretchen K. Campbell. Hysteresis in a quantized superfluid ‘atomtronic’ circuit. *Nature*, 506(7487):200–203, 2014.
- [19] F. Jendrzejewski, S. Eckel, N. Murray, C. Lanier, M. Edwards, C. J. Lobb, and G. K. Campbell. Resistive flow in a weakly interacting bose-einstein condensate. *Phys. Rev. Lett.*, 113:045305, Jul 2014.
- [20] T. L. Gustavson, P. Bouyer, and M. A. Kasevich. Precision rotation measurements with an atom interferometer gyroscope. *Phys. Rev. Lett.*, 78:2046–2049, Mar 1997.
- [21] Carlos Barceló, S. Liberati, and Matt Visser. Probing semiclassical analog gravity in bose-einstein condensates with widely tunable interactions. *Phys. Rev. A*, 68:053613, Nov 2003.

- [22] Chen-Lung Hung, Victor Gurarie, and Cheng Chin. From cosmology to cold atoms: Observation of sakharov oscillations in a quenched atomic superfluid. *Science*, 341(6151):1213–1215, 2013.
- [23] Jeff Steinhauer. Observation of self-amplifying hawking radiation in an analogue black-hole laser. *Nature Physics*, 10(11):864–869, 2014.
- [24] Jeff Steinhauer. Observation of quantum hawking radiation and its entanglement in an analogue black hole. *Nature Physics*, 12(10):959–965, August 2016.
- [25] Jeff Steinhauer, Murad Abuzarli, Tangui Aladjidi, Tom Bienaimé, Clara Piekarski, Wei Liu, Elisabeth Giacobino, Alberto Bramati, and Quentin Glorieux. Analogue cosmological particle creation in an ultracold quantum fluid of light. *arxiv:2102.08279*, 2021.
- [26] A. Einstein. Quantentheorie des einatomigen idealen gases. *Sitzungsberichte der Preussischen Akademie der Wissenschaften*, 1, 1925.
- [27] S.N. Bose. Plancks gesetz und lichtquantenhypothese. *Zeitschrift für Physik*, 26, 1924.
- [28] William D. Phillips and Harold Metcalf. Laser deceleration of an atomic beam. *Phys. Rev. Lett.*, 48:596–599, Mar 1982.
- [29] Steven Chu, L. Hollberg, J. E. Bjorkholm, Alex Cable, and A. Ashkin. Three-dimensional viscous confinement and cooling of atoms by resonance radiation pressure. *Phys. Rev. Lett.*, 55:48–51, Jul 1985.
- [30] Paul D. Lett, Richard N. Watts, Christoph I. Westbrook, William D. Phillips, Phillip L. Gould, and Harold J. Metcalf. Observation of atoms laser cooled below the doppler limit. *Phys. Rev. Lett.*, 61:169–172, Jul 1988.
- [31] Wolfgang Petrich, Michael H. Anderson, Jason R. Ensher, and Eric A. Cornell. Stable, tightly confining magnetic trap for evaporative cooling of neutral atoms. *Phys. Rev. Lett.*, 74:3352–3355, Apr 1995.
- [32] Kendall B. Davis, Marc-Oliver Mewes, Michael A. Joffe, Michael R. Andrews, and Wolfgang Ketterle. Evaporative cooling of sodium atoms. *Phys. Rev. Lett.*, 74:5202–5205, Jun 1995.
- [33] C. J. Pethick and H. Smith. *Bose–Einstein Condensation in Dilute Gases*. Cambridge University Press, 2 edition, 2008.
- [34] Stringari S. Pitaevski, L. P. *Bose-Einstein condensation*. Oxford University Press, 2016.
- [35] Cheng Chin, Rudolf Grimm, Paul Julienne, and Eite Tiesinga. Feshbach resonances in ultracold gases. *Rev. Mod. Phys.*, 82:1225–1286, Apr 2010.

- [36] D.M. Stamper-Kurn, W. Ketterle, D.S. Durfee. Making, probing and understanding bose-einstein condensates, 1999.
- [37] C. Ryu, M. F. Andersen, P. Cladé, Vasant Natarajan, K. Helmerson, and W. D. Phillips. Observation of persistent flow of a bose-einstein condensate in a toroidal trap. *Phys. Rev. Lett.*, 99:260401, Dec 2007.
- [38] A. Ramanathan, K. C. Wright, S. R. Muniz, M. Zelan, W. T. Hill, C. J. Lobb, K. Helmerson, W. D. Phillips, and G. K. Campbell. Superflow in a toroidal bose-einstein condensate: An atom circuit with a tunable weak link. *Phys. Rev. Lett.*, 106:130401, Mar 2011.
- [39] A Kumar, N Anderson, W D Phillips, S Eckel, G K Campbell, and S Stringari. Minimally destructive, doppler measurement of a quantized flow in a ring-shaped bose-einstein condensate. *New Journal of Physics*, 18(2):025001, feb 2016.
- [40] A. Kumar, S. Eckel, F. Jendrzejewski, and G. K. Campbell. Temperature-induced decay of persistent currents in a superfluid ultracold gas. *Phys. Rev. A*, 95:021602, Feb 2017.
- [41] S. Eckel, A. Kumar, T. Jacobson, I. B. Spielman, and G. K. Campbell. A rapidly expanding bose-einstein condensate: An expanding universe in the lab. *Phys. Rev. X*, 8:021021, Apr 2018.
- [42] Christopher J Foot. *Atomic physics*. Oxford master series in atomic, optical, and laser physics. Oxford University Press, Oxford, 2007.
- [43] Straten P. Metcalf, H. J. *Laser Cooling and Trapping*. Springer, 2 edition, 2002.
- [44] Beale P.D. Pathria, R. K. *Statistical Mechanics*. Elsevier Science, 2011.
- [45] Franco Dalfovo, Stefano Giorgini, Lev P. Pitaevskii, and Sandro Stringari. Theory of bose-einstein condensation in trapped gases. *Rev. Mod. Phys.*, 71:463–512, Apr 1999.
- [46] P. O. Fedichev, G. V. Shlyapnikov, and J. T. M. Walraven. Damping of low-energy excitations of a trapped bose-einstein condensate at finite temperatures. *Phys. Rev. Lett.*, 80:2269–2272, Mar 1998.
- [47] G. Edward Marti, Ryan Olf, and Dan M. Stamper-Kurn. Collective excitation interferometry with a toroidal bose-einstein condensate. *Phys. Rev. A*, 91:013602, Jan 2015.
- [48] N. Katz, J. Steinhauer, R. Ozeri, and N. Davidson. Beliaev damping of quasiparticles in a bose-einstein condensate. *Phys. Rev. Lett.*, 89:220401, Nov 2002.
- [49] Carlos Barceló, Stefano Liberati, and Matt Visser. Analogue gravity. *Living Reviews in Relativity*, 14(1):3, 2011.

- [50] Weinfurter S. Jacquet M. J. and König F. The next generation of analogue gravity experiments. *Phil. Trans. R. Soc. A*, 2021.
- [51] W. G. Unruh. Experimental black-hole evaporation? *Phys. Rev. Lett.*, 46:1351–1353, May 1981.
- [52] S. W. HAWKING. Black hole explosions? *Nature*, 248(5443):30–31, 1974.
- [53] S. W. Hawking. Particle creation by black holes. *Communications in Mathematical Physics*, 43(3):199–220, 1975.
- [54] L. J. Garay, J. R. Anglin, J. I. Cirac, and P. Zoller. Sonic analog of gravitational black holes in bose-einstein condensates. *Phys. Rev. Lett.*, 85:4643–4647, Nov 2000.
- [55] L. J. Garay, J. R. Anglin, J. I. Cirac, and P. Zoller. Sonic black holes in dilute bose-einstein condensates. *Phys. Rev. A*, 63:023611, Jan 2001.
- [56] M.-a. Sakagami and A. Ohashi. Hawking radiation in the laboratory. *Progress of Theoretical Physics*, 107(6):1267–1272, Jun 2002.
- [57] Hironobu Furuhashi, Yasusada Nambu, and Hiromi Saida. Simulation of an acoustic black hole in a laval nozzle. *Classical and Quantum Gravity*, 23(17):5417–5438, Aug 2006.
- [58] Satoshi Okuzumi and Masa-aki Sakagami. Quasinormal ringing of acoustic black holes in laval nozzles: Numerical simulations. *Physical Review D*, 76(8), Oct 2007.
- [59] Oren Lahav, Amir Itah, Alex Blumkin, Carmit Gordon, Shahar Rinott, Alona Zayats, and Jeff Steinhauer. Realization of a sonic black hole analog in a bose-einstein condensate. *Phys. Rev. Lett.*, 105:240401, Dec 2010.
- [60] Juan Ramón Muñoz de Nova, Katrine Golubkov, Victor I. Kolobov, and Jeff Steinhauer. Observation of thermal hawking radiation and its temperature in an analogue black hole. *Nature*, 569(7758):688–691, 2019.
- [61] J.-C. Jaskula, G. B. Partridge, M. Bonneau, R. Lopes, J. Ruaudel, D. Boiron, and C. I. Westbrook. Acoustic analog to the dynamical casimir effect in a bose-einstein condensate. *Phys. Rev. Lett.*, 109:220401, Nov 2012.
- [62] Stephen Eckel and Ted Jacobson. Phonon Redshift and Hubble Friction in an Expanding BEC. *SciPost Phys.*, 10:64, 2021.
- [63] Eric D. Black. An introduction to pound–drever–hall laser frequency stabilization. *American Journal of Physics*, 69(1):79–87, 2001.
- [64] Monica Gutierrez Galan. *Bose Einstein Condensates for Analogue Cosmology Experiments*. PhD thesis, University of Maryland, 2021.

- [65] F Salcés-Carcoba. *Microscopy of Elongated Superfluids*. PhD thesis, University of Maryland, 2020.
- [66] J.F. Jarvis, C.N. Judice, and W.H. Ninke. A survey of techniques for the display of continuous tone pictures on bilevel displays. *Computer Graphics and Image Processing*, 5(1):13–40, 1976.
- [67] Klaus Hueck, Niclas Luick, Lennart Sobirey, Jonas Siegl, Thomas Lompe, Henning Moritz, Logan W. Clark, and Cheng Chin. Calibrating high intensity absorption imaging of ultracold atoms. *Opt. Express*, 25(8):8670–8679, Apr 2017.
- [68] Anand Ramanathan, Sérgio R. Muniz, Kevin C. Wright, Russell P. Anderson, William D. Phillips, Kristian Helmerson, and Gretchen K. Campbell. Partial-transfer absorption imaging: A versatile technique for optimal imaging of ultracold gases. *Review of Scientific Instruments*, 83(8):083119, 2012.
- [69] T. G. Tiecke, S. D. Gensemer, A. Ludewig, and J. T. M. Walraven. High-flux two-dimensional magneto-optical-trap source for cold lithium atoms. *Phys. Rev. A*, 80:013409, Jul 2009.
- [70] J. Schoser, A. Batär, R. Löw, V. Schweikhard, A. Grabowski, Yu. B. Ovchinnikov, and T. Pfau. Intense source of cold rb atoms from a pure two-dimensional magneto-optical trap. *Phys. Rev. A*, 66:023410, Aug 2002.
- [71] G. Lamporesi, S. Donadello, S. Serafini, and G. Ferrari. Compact high-flux source of cold sodium atoms. *Review of Scientific Instruments*, 84(6):063102, 2013.
- [72] Wolfgang Ketterle, Kendall B. Davis, Michael A. Joffe, Alex Martin, and David E. Pritchard. High densities of cold atoms in a dark spontaneous-force optical trap. *Phys. Rev. Lett.*, 70:2253–2256, Apr 1993.
- [73] J. Dalibard and C. Cohen-Tannoudji. Laser cooling below the doppler limit by polarization gradients: simple theoretical models. *J. Opt. Soc. Am. B*, 6(11):2023–2045, Nov 1989.
- [74] Wolfgang Ketterle and N.J. Van Druten. Evaporative cooling of trapped atoms. volume 37 of *Advances In Atomic, Molecular, and Optical Physics*, pages 181–236. Academic Press, 1996.
- [75] K. M. O’Hara, M. E. Gehm, S. R. Granade, and J. E. Thomas. Scaling laws for evaporative cooling in time-dependent optical traps. *Phys. Rev. A*, 64:051403, Oct 2001.
- [76] Y.-J. Lin, A. R. Perry, R. L. Compton, I. B. Spielman, and J. V. Porto. Rapid production of ^{87}Rb bose-einstein condensates in a combined magnetic and optical potential. *Phys. Rev. A*, 79:063631, Jun 2009.

- [77] Alan L. Migdall, John V. Prodan, William D. Phillips, Thomas H. Bergeman, and Harold J. Metcalf. First observation of magnetically trapped neutral atoms. *Phys. Rev. Lett.*, 54:2596–2599, Jun 1985.
- [78] T. H. Bergeman, Patrick McNicholl, Jan Kycia, Harold Metcalf, and N. L. Balazs. Quantized motion of atoms in a quadrupole magnetostatic trap. *J. Opt. Soc. Am. B*, 6(11):2249–2256, Nov 1989.
- [79] William D. Phillips, John V. Prodan, and Harold J. Metcalf. Laser cooling and electromagnetic trapping of neutral atoms. *J. Opt. Soc. Am. B*, 2(11):1751–1767, Nov 1985.
- [80] S. Banik, M. Gutierrez Galan, H. Sosa-Martinez, M. Anderson, S. Eckel, I. B. Spielman, and G. K. Campbell. Hubble attenuation and amplification in expanding and contracting cold-atom universes, 2021.
- [81] D. Baumann. Inflation. In *Physics of the Large and the Small*, pages 523–686. World Scientific, 2011.
- [82] J. M. Gomez Llorente and J. Plata. Expanding ring-shaped bose-einstein condensates as analogs of cosmological models: Analytical characterization of the inflationary dynamics. *Phys. Rev. A*, 100:043613, Oct 2019.
- [83] Germain Rousseaux, Christian Mathis, Philippe Maïssa, Thomas G Philbin, and Ulf Leonhardt. Observation of negative-frequency waves in a water tank: a classical analogue to the hawking effect? *New J. Phys*, page 053015, May 2008.
- [84] Thomas G. Philbin, Chris Kuklewicz, Scott Robertson, Stephen Hill, Friedrich König, and Ulf Leonhardt. Fiber-optical analog of the event horizon. *Science*, 319:1367–1370, Mar 2008.
- [85] H. S. Nguyen, D. Gerace, I. Carusotto, D. Sanvitto, E. Galopin, A. Lemaître, I. Sagnes, J. Bloch, and A. Amo. Acoustic black hole in a stationary hydrodynamic flow of microcavity polaritons. *Phys. Rev. Lett.*, 114:036402, Jan 2015.
- [86] F. Belgiorno, S. L. Cacciatori, M. Clerici, V. Gorini, G. Ortenzi, L. Rizzi, E. Rubino, V. G. Sala, and D. Faccio. Hawking radiation from ultrashort laser pulse filaments. *Phys. Rev. Lett.*, 105:203901, Nov 2010.
- [87] E. Rubino, J. McLenaghan, S. C. Kehr, F. Belgiorno, D. Townsend, S. Rohr, C. E. Kuklewicz, U. Leonhardt, F. König, and D. Faccio. Negative-frequency resonant radiation. *Phys. Rev. Lett.*, 108:253901, Jun 2012.
- [88] Theo Torres, Sam Patrick, Antonin Coutant, Maurício Richartz, Edmund W. Tedford, and Silke Weinfurter. Rotational superradiant scattering in a vortex flow. *Nature Physics*, 13:833–836, 2017.

- [89] C. Cao, E. Elliott, J. Joseph, H. Wu, J. Petricka, T. Schäfer, and J. E. Thomas. Universal quantum viscosity in a unitary fermi gas. *Science*, 331(6013):58–61, 2011.
- [90] Y. Ohashi, H. Tajima, and P. van Wyk. Bcs–bec crossover in cold atomic and in nuclear systems. *Progress in Particle and Nuclear Physics*, 111:103739, 2020.
- [91] Victor I. Kolobov, Katrine Golubkov, Juan Ramón Muñoz de Nova, and Jeff Steinhauer. Observation of stationary spontaneous hawking radiation and the time evolution of an analogue black hole. *Nature Physics*, 17(3):362–367, 2021.
- [92] Uwe R. Fischer and Ralf Schützhold. Quantum simulation of cosmic inflation in two-component bose-einstein condensates. *Phys. Rev. A*, 70:063615, Dec 2004.
- [93] Ming-Chiang Chung and Aranya B Bhattacharjee. Damping in 2d and 3d dilute bose gases. *New Journal of Physics*, 11(12):123012, dec 2009.
- [94] Antonin Coutant and Silke Weinfurter. An acoustic probe for quantum vorticity in bose-einstein condensates. *arXiv:1504.00691*, 04 2015.
- [95] B. DeMarco and D. S. Jin. Onset of fermi degeneracy in a trapped atomic gas. *Science*, 285(5434):1703–1706, 1999.
- [96] F. Schreck, L. Khaykovich, K. L. Corwin, G. Ferrari, T. Bourdel, J. Cubizolles, and C. Salomon. Quasipure bose-einstein condensate immersed in a fermi sea. *Phys. Rev. Lett.*, 87:080403, Aug 2001.
- [97] Andrew G. Truscott, Kevin E. Strecker, William I. McAlexander, Guthrie B. Partridge, and Randall G. Hulet. Observation of fermi pressure in a gas of trapped atoms. *Science*, 291(5513):2570–2572, 2001.
- [98] T Lahaye, C Menotti, L Santos, M Lewenstein, and T Pfau. The physics of dipolar bosonic quantum gases. *Reports on Progress in Physics*, 72(12):126401, nov 2009.
- [99] Ph. Courteille, R. S. Freeland, D. J. Heinzen, F. A. van Abeelen, and B. J. Verhaar. Observation of a feshbach resonance in cold atom scattering. *Phys. Rev. Lett.*, 81:69–72, Jul 1998.
- [100] Albert Frisch, Michael Mark, Kiyotaka Aikawa, Francesca Ferlaino, John L. Bohn, Constantinos Makrides, Alexander Petrov, and Svetlana Kotochigova. Quantum chaos in ultracold collisions of gas-phase erbium atoms. *Nature*, 507(7493):475–479, 2014.
- [101] S. Inouye, M. R. Andrews, J. Stenger, H. J. Miesner, D. M. Stamper-Kurn, and W. Ketterle. Observation of feshbach resonances in a bose–einstein condensate. *Nature*, 392(6672):151–154, 1998.
- [102] J. Stenger, S. Inouye, M. R. Andrews, H.-J. Miesner, D. M. Stamper-Kurn, and W. Ketterle. Strongly enhanced inelastic collisions in a bose-einstein condensate near feshbach resonances. *Phys. Rev. Lett.*, 82:2422–2425, Mar 1999.

- [103] Axel Griesmaier, Jörg Werner, Sven Hensler, Jürgen Stuhler, and Tilman Pfau. Bose-einstein condensation of chromium. *Phys. Rev. Lett.*, 94:160401, Apr 2005.
- [104] Mingwu Lu, Nathaniel Q. Burdick, Seo Ho Youn, and Benjamin L. Lev. Strongly dipolar bose-einstein condensate of dysprosium. *Phys. Rev. Lett.*, 107:190401, Oct 2011.
- [105] K. Aikawa, A. Frisch, M. Mark, S. Baier, A. Rietzler, R. Grimm, and F. Ferlaino. Bose-einstein condensation of erbium. *Phys. Rev. Lett.*, 108:210401, May 2012.
- [106] Xiaojiao Dai, Yanyi Jiang, Chao Hang, Zhiyi Bi, and Longsheng Ma. Thermal analysis of optical reference cavities for low sensitivity to environmental temperature fluctuations. *Opt. Express*, 23(4):5134–5146, Feb 2015.
- [107] R. W. P. Drever, J. L. Hall, F. V. Kowalski, J. Hough, G. M. Ford, A. J. Munley, and H. Ward. Laser phase and frequency stabilization using an optical resonator. *Applied Physics B*, 31(2):97–105, 1983.
- [108] Warren G Nagourney. *Quantum electronics for atomic physics*. Oxford : Oxford University Press, [2010] ©2010, [2010].
- [109] Bahaa E A Saleh and Malvin Carl Teich. *Fundamentals of photonics; 2nd ed.* Wiley series in pure and applied optics. Wiley, New York, NY, 2007.
- [110] Michael Hercher. The spherical mirror fabry-perot interferometer. *Appl. Opt.*, 7(5):951–966, May 1968.
- [111] Benjamin Rechovsky. A narrow line laser system for cooling strontium. *Joint Quantum Institute, University of Maryland NIST*, 2013.
- [112] E. Lally. A narrow-linewidth laser at 1550 nm using the pound-drever-hall stabilization technique. Master’s thesis, Virginia Tech, 2006.
- [113] Petr O. Fedichev and Uwe R. Fischer. Gibbons-hawking effect in the sonic de sitter space-time of an expanding bose-einstein-condensed gas. *Phys. Rev. Lett.*, 91:240407, Dec 2003.
- [114] Petr O. Fedichev and Uwe R. Fischer. “cosmological” quasiparticle production in harmonically trapped superfluid gases. *Phys. Rev. A*, 69:033602, Mar 2004.
- [115] Piyush Jain, Silke Weinfurtnner, Matt Visser, and C. W. Gardiner. Analog model of a friedmann-robertson-walker universe in bose-einstein condensates: Application of the classical field method. *Phys. Rev. A*, 76:033616, Sep 2007.
- [116] Angus Prain, Serena Fagnocchi, and Stefano Liberati. Analogue cosmological particle creation: Quantum correlations in expanding bose-einstein condensates. *Phys. Rev. D*, 82:105018, Nov 2010.

- [117] Chen-Lung Hung, Xibo Zhang, Li-Chung Ha, Shih-Kuang Tung, Nathan Gemelke, and Cheng Chin. Extracting density–density correlations from in situ images of atomic quantum gases. *New Journal of Physics*, 13(7):075019, jul 2011.
- [118] Emine Altuntaş and I. B. Spielman. Self-bayesian aberration removal via constraints for ultracold atom microscopy. *Phys. Rev. Research*, 3:043087, Oct 2021.
- [119] Augustus J. E. M. Janssen. Extended nijboer–zernike approach for the computation of optical point-spread functions. *J. Opt. Soc. Am. A*, 19(5):849–857, May 2002.